Reduced kinetic model of polyatomic gases using lattice Boltzmann methods

This dissertation is submitted for the degree of

Doctor of Philosophy

By

Praveen Kumar Kolluru

JNCASR

Engineering Mechanics Unit

Jawaharlal Nehru Centre For Advanced Scientific Research

(A Deemed University)

Bengaluru - 560064

JULY 2024

Declaration

I hereby declare that the matter embodied in the thesis entitled **“Reduced kinetic model of polyatomic gases using lattice Boltzmann methods”** is the result of investigations carried out by me at the Engineering Mechanics Unit, Jawaharlal Nehru Centre for Advanced Scientific Research, Bengaluru, India under the supervision of **Prof. Santosh Ansumali** and that it has not been submitted elsewhere for the award of any degree or diploma.

In keeping with the general practice of reporting scientific observations, due acknowledgement has been made whenever the work described is based on the findings of other investigators.

Praveen Kumar Kolluru
January 2025

Certificate

I hereby certify that the matter embodied in this thesis entitled **“Reduced kinetic model of polyatomic gases using lattice Boltzmann methods”** has been carried out by **Mr. Praveen Kumar Kolluru** at the Engineering Mechanics Unit, Jawaharlal Nehru Centre for Advanced Scientific Research, Bangalore, India under my supervision and that it has not been submitted elsewhere for the award of any degree or diploma.

Santosh

Santosh Ansumali

July 2024

Acknowledgements

I would like to express my sincere gratitude to my advisor, Prof. Santosh Ansumali, for his unwavering support and immense patience throughout my PhD. I am also grateful to Prof. Ganesh Subramanian, Prof. K.R. Sreenivas, Prof. Mehboob Alam, and Prof. Meher Prakash for their excellent courses. I am deeply indebted to Prof. V. Kumaran for his invaluable feedback.

I would like to thank my friends from the DNS lab - Atif, Samarth, Akshay, Rhoheth, Shaurya, Rafi, and Vybhav for their invaluable assistance and discussions. I would also like to extend my gratitude to Siddharth, Chakradhar, and Manjusha for their help in various aspects of my work.

I am thankful to Dr. Joydeep De, Mr. A. Jayachandra, Dr. Princy, employees of the library, complab, hostel, and other staff for their cooperation.

I want to express my sincere appreciation to my family and friends for their unwavering support and encouragement throughout my journey.

Abstract

The Boltzmann collision kernel and the widely used Bhatnagar–Gross–Krook (BGK) model are limited to monatomic gases as they do not account for the internal molecular structure. However, many real gases such as nitrogen, oxygen and methane are polyatomic. Kinetic models of polyatomic gas typically account for the internal degrees of freedom at the level of the two-particle distribution function. Close to the hydrodynamic limit, the internal (rotational) degrees of freedom tend to be well represented just by rotational kinetic energy density. We account for the rotational energy by augmenting the ellipsoidal statistical Bhatnagar–Gross–Krook (ES–BGK) model, an extension of the BGK model, at the level of the single-particle distribution function with an advection–diffusion–relaxation equation for the rotational energy. This reduced model respects the H theorem and recovers the compressible hydrodynamics for polyatomic gases as its macroscopic limit. As required for a polyatomic gas model, this extension of the ES–BGK model not only has the correct specific heat ratio but also allows for three independent tunable transport coefficients: thermal conductivity, shear viscosity and bulk viscosity.

An energy-conserving lattice Boltzmann model based on a crystallographic lattice for the simulation of weakly compressible flows is also proposed. The theoretical requirements and the methodology to construct such a model are discussed. We demonstrate that the model recovers the isentropic sound speed in addition to the effects of viscous heating and heat flux dynamics.

Table of contents

List of figures

List of tables

Chapter 1

Introduction

Computational Fluid Dynamics (CFD) plays a crucial role in understanding fluid flow behavior across a wide range of applications, from process engineering to aerodynamics. Characterized by non-dimensional numbers such as the Reynolds number, fluid flows can range significantly, from as low as 10^{-3} in microfluidic devices to upwards of 10^8 in external aerodynamic flows over airplane wings. Governed by the complex, non-linear Navier-Stokes-Fourier equations, these flows necessitate numerical solutions across potentially billions of grid points, with the complexity further amplified by intricate geometries and boundary conditions. Simulation methods vary: Direct Numerical Simulation (DNS) encompasses all scales of flow, Large Eddy Simulation (LES) targets large-scale turbulent structures, and Reynolds-Averaged Navier-Stokes (RANS) offers time-averaged solutions through statistical averaging. Hybrid approaches, combining techniques like LES and RANS, adapt to simulate turbulence scales differently across the computational domain, while particle-based methods like Direct Simulation Monte Carlo (DSMC) focus on resolving smaller scales in critical regions, demonstrating the field's trend towards methodological diversification to address specific challenges.

The accurate simulations of fluid flow, such as that over an aeroplane wing resolving all length and time scales, are not yet possible due to the current limitations of computer hardware, though GPUs show promising advancements. The evolution towards exascale computing and the growing interest in digital twins for complex physical object simulations in manufacturing underscores the need for more efficient algorithms and numerical methods that excel in parallel scalability. Presently, methods vary in their suitability and efficiency; for instance, Lattice Boltzmann methods excel in parallelization due to their simple algorithms, unlike the traditional methods, which struggle with complex geometries. Moreover, the integration of multiphysics solvers, essential for simulating coupled physical phenomena, is challenged by the disparate timescales these phenomena operate on, highlighting the need for algorithms capable of bridging this spectral gap to enhance simulation efficiency.

The lattice Boltzmann (LB) method with its simplified kinetic description of hydrodynamics in terms of a sequence of collision and free flight restricted on a D-dimensional lattice provides a computationally efficient and easily parallelizable alternative simulation methodology [4, 40, 127]. An LB model in its standard formulation describes a weakly compressible flow at a reference temperature T_0. The pressure p and the mass density ρ are related via the ideal equation of state $p = \rho\theta_0$, where $\theta_0 = k_B T_0/m$ is the scaled temperature with k_B as the Boltzmann constant and m is the mass of the molecule. These models are quite suitable for isothermal flows where the relevant time scale is a few orders of magnitude higher than the acoustic time scales and the object of interest is the velocity or vorticity field. A consequence of kinetic equation with an isothermal dynamics, as revealed by Chapman-Enskog expansion, is that in the hydrodynamic limit, the stress tensor is not traceless and is of form [127, 11]

$$\sigma_{\alpha\beta} = \eta \left(\partial_\alpha u_\beta + \partial_\beta u_\alpha\right), \tag{1.1}$$

which implies that the bulk viscosity $\zeta = 2/3\eta$, where η is the shear viscosity. Even though this expression for bulk viscosity is not realistic for any fluid, this is not of too much concern as long as one is interested in the velocity dynamics in the limit of vanishing Mach number Ma. This is due to the fact that the divergence of the velocity field for low Mach number is $\partial_\kappa u_\kappa \sim O(\mathrm{Ma}^2)$ [48]. Thus, the method is routinely used for incompressible hydrodynamic simulations both in low Reynolds number creeping flow regime as well as for high Reynolds number turbulent flow regime [4, 40, 78–80, 101, 127].

An extension of the lattice Boltzmann method (LBM) for acoustics is relatively recent [30, 46, 48, 88, 93, 133, 134]. These works have established the capability of LBM to correctly reproduce fundamental acoustic phenomena and highlighted the low dissipative behaviour of the LBM. The starting point for acoustic modeling in isothermal LB is the fact that the pressure fluctuation δp (linearized around no flow condition) for the method follows the wave equation [82]

$$\frac{\partial^2 \delta p}{\partial t^2} = \bar{c}_s^2 \nabla^2 \delta p, \tag{1.2}$$

with the isothermal sound speed being $\overline{c}_s \equiv \sqrt{\partial p/\partial \rho|_T} = \sqrt{\theta_0}$. It needs to be noted that the sound wave is generated by compression and expansion of air and is not an isothermal but an adiabatic process. Thus, it is not surprising that neglecting the rapidly-fluctuating temperature field in a sound wave leads to an incorrect value of the sound speed. The real isentropic sound speed is $c_s = \sqrt{\partial p/\partial \rho|_s} = \sqrt{\gamma\theta}$, where γ is the specific heat ratio. However, in practice for simulating acoustic waves, this incorrect sound speed is not of too much concern, as dynamics can be corrected via rescaling of temperature. In particular, Eq.(1.2) describes the correct acoustic dynamics at temperature $\theta = \theta_0/\gamma$.

However, a more elaborate description of the sound wave in LB framework must start from the true evolution equation for pressure fluctuation obtained by Navier-Stokes-Fourier (NSF) equation linearized around no flow condition as [33]

$$\left[-\frac{\partial^2}{\partial t^2} + \frac{\Gamma}{\rho_0}\frac{\partial}{\partial t}\nabla^2\right]\delta\rho + \nabla^2\delta p = 0, \tag{1.3}$$

where $\delta\rho$ is the density fluctuation from the equilibrium density ρ_0 and $\Gamma = 4\eta/3 + \zeta$. The thermodynamic equation of state relates the density and pressure fluctuations with the entropy fluctuation via the relation [31]

$$\delta\rho = \left.\frac{\partial \rho}{\partial p}\right|_s \delta p + \left.\frac{\partial \rho}{\partial s}\right|_p \delta s, \tag{1.4}$$

where, the entropy density fluctuation δs satisfies the relation [82]

$$\frac{\partial \delta s}{\partial t} = -\frac{1}{\rho_0 T_0}\nabla_\alpha \delta q_\alpha, \tag{1.5}$$

with the heat flux due to the temperature fluctuation δq_α obeying the Fourier's law i.e., $\delta q_\alpha = -\kappa\nabla_\alpha \delta T$ where κ is the thermal conductivity [85].

Thus, the final evolution equation for the pressure fluctuation obtained using Eqs.(1.3),(1.4) is

$$\left[-\frac{\partial^2}{\partial t^2} + \frac{1}{\rho_0}\Gamma\frac{\partial}{\partial t}\nabla^2\right]\left(\left.\frac{\partial \rho}{\partial p}\right|_s \delta p + \left.\frac{\partial \rho}{\partial s}\right|_p \delta s\right) + \nabla^2\delta p = 0, \tag{1.6}$$

where the entropy fluctuation is governed by Eq.(1.5). For short time dynamics, i.e., at time scales much less than the momentum diffusion time scales, the dynamics can be considered to be isentropic and entropy fluctuations as well as the viscous contribution can be ignored. This reduces Eq.(1.6) to the wave equation as solved by an isothermal LB model given in Eq.(1.2).

However, a faithful simulation of acoustics by LB models requires that for a linearized flow, the pressure fluctuations obey Eq.(1.6), which in turn demands accurate heat flux dynamics via Eq.(1.5).

Despite their success, the Boltzmann collision kernel and its aforementioned simplifications are limited to monoatomic gases as they do not account for the internal molecular structure. However, many real gases such as nitrogen, oxygen, or methane are polyatomic. At the macroscopic level, the internal molecular structure predominantly manifests in terms of modified specific heat ratio γ and bulk viscosity $\eta_{\rm b}$, which is crucial for a number of aerodynamic and turbomachinery engineering applications [135, 142]. The specific heat ratio predicted by the Boltzmann equation is that of a monoatomic gas ($\gamma = 5/3$), whereas that of a diatomic gas is $7/5$.

Two-particle kinetic theory as an extension of the Boltzmann equation as expected correctly predicts the specific heat ratio for polyatomic gases along with heat conductivity and the bulk viscosity [138, 142, 35]. However, it is often not feasible to do any analysis on the Boltzmann-type equation for polyatomic gases. Therefore, several simplifications to model polyatomic gases have also been proposed. They essentially incorporate the rotational kinetic energy by decomposing the two-particle distribution function into two independent single-particle distribution functions [6, 21, 70, 83, 96, 102, 132, 137, 140, 142]. Furthermore, a thermodynamic framework and extensions thereof were developed for modelling highly nonequilibrium phenomena in dense and rarefied polyatomic gases where the Navier–Stokes–Fourier theory is no longer valid [14, 99, 113]. A few BGK like models have also been proposed for polyatomic gases which accept the Prandtl number as a tunable parameter [6, 29].

Hydrodynamic simulations for a realistic system require the development of reduced-order models to account for rotational degrees of freedom ideally without increasing the phase-space dimensionality. Indeed, the standard approach is to demonstrate that the two-particle distribution function describing the translational and rotational degrees of freedom can be approximated by considering two single-particle distribution functions (one for the translational and another for the rotational degrees of freedom) whose dynamics are coupled to each other [6].

The dynamics of a dilute monoatomic gas in terms of the single-particle distribution function is described by the Boltzmann equation [32, 35]. Unlike the continuum Navier–Stokes–Fourier hydrodynamics equation, the Boltzmann equation is a valid description even at highly non-equilibrium states [32, 90, 98], encountered in the presence of strong shock waves at high Mach number (ratio of flow speed to sound speed) and in a highly rarefied flow characterized by a large Knudsen number (ratio of the mean free path to characteristic length scale) [8, 103, 125]. However, any analysis of the integro-differential Boltzmann equation is a formidable task, even for the simplest problems. Thus, one often models the Boltzmann dynamics via a simplified collision term that converts the evolution equation to a partial differential equation [3, 6, 7, 23, 56, 63, 86, 87, 116, 121]. An important example is the BGK model [23], which states that the relaxation of the distribution function towards the Maxwell–Boltzmann (MB) form happens in a time scale corresponding to the mean free time τ with the assumption that every moment of the distribution function relaxes at the same rate. The BGK model is quite successful in replicating qualitative features of the Boltzmann dynamics (collisional invariants, the zero of the collision, H-theorem, conservation laws, etc). However, the BGK model predicts the Prandtl number of the fluid to be unity, while the value predicted by the Boltzmann equation for monoatomic gas is $2/3$. Thus, several other variations of the collision model, such as ES–BGK model [6, 63], the quasi-equilibrium models [56, 87], the Shakhov model [116], and the Fokker-Plank model [121, 123] are used as kinetic models with tunable Prandtl number. The ES–BGK model [6, 63] is an elegant but simple improvement over the BGK model. This model assumes that the distribution function relaxes to an anisotropic Gaussian distribution within mean free time τ. The anisotropic Gaussian in itself evolves towards the MB distribution with a second-time scale. The presence of a second-time scale as a free parameter ensures that the time scales related to momentum and thermal diffusivity are independent and thus permits one to vary the Prandtl number in the range of $2/3$ to ∞.

1.1 Highlights of this thesis

Motivated by the above challenges, this thesis addresses the following questions

- How to formulate a lattice Boltzmann model to recover the isentropic sound speed and capture the dynamics of pressure fluctuations accurately?
- Is it possible to model the influence of internal degrees of freedom using a scalar variable and thereby develop a simplified kinetic model that accurately reflects the specific heat ratio and Prandtl number through a single distribution function?

- Are there any numerical methods that can accelerate simulations when the time scales involved are spread across multiple orders of magnitude?

The thesis is organised as follows: In Chapter 2, the fundamentals of kinetic theory are revised, defining crucial time scales and non-dimensional numbers. The transport properties of a dilute monoatomic gas are estimated, and the Boltzmann equation is discussed in terms of the evolution of the single-particle distribution function. Its moments are defined, along with the Maxwell-Boltzmann distribution function. The focus then shifts to the two most widely used collisional models, the BGK model and ES-BGK model.

In Chapter 3[*], a higher-order lattice Boltzmann model is proposed that recovers the isentropic speed of sound and has the ability to recover pressure dynamics accurately. The discussion begins with the lattice Boltzmann method, identifying the restrictions on a discrete velocity model to recover isothermal compressible hydrodynamics. The constraints on a model that recovers the required moments essential for compressible thermohydrodynamics simulations are identified. An energy-conserving equilibrium distribution function for this weakly compressible LB model is derived, demonstrating its capability for simulating acoustic phenomena. A few test cases are presented to showcase its ability to simulate thermal flows.

In Chapter 4[†], a reduced kinetic model is proposed by extending the ES-BGK model for polyatomic gases, and the transport properties for this model are derived. The lattice Boltzmann formulation for the polyatomic model is then proposed and validated numerically. An alternative model for diatomic gases has also been presented with a few validations.

In Chapter 5, a brief review of projective integration methods is provided, showing that there exists a better estimate for the derivative required for the projective step, and the stability of the new methods is discussed. A few canonical test cases using the new method are presented.

In Chapter 6, an outlook of the thesis is presented.

---

[*] Text from this chapter has been published in Physical Review E, Volume 101, on page 013309 under the title "Lattice Boltzmann Model for Weakly Compressible Flows". This paper was highlighted as an Editors' Suggestion. ©2020 by the American Physical Society.

[†] Material from this chapter has been published in the Journal of Fluid Mechanics, Volume 963, Pages A7 titled "Reduced Kinetic Model of Polyatomic Gases". This chapter has been reprinted with permission. ©The Authors. It was published in 2023 by Cambridge University Press. Additionally, this chapter also includes text from "Extended BGK Model for Diatomic Gases," published in the Journal of Computational Sciences, Volume 45, on page 101179. ©2020 Elsevier B.V.

Chapter 2

Kinetic Theory

2.1 Introduction

Fluid transport equations are commonly expressed through the conservation laws for mass, momentum, and energy, complemented by constitutive laws governing the stress tensor and heat flux. This continuum representation is known as the Navier-Stokes-Fourier (NS) equation [19, 82]. However, on the microscopic scale, the control volume is envisioned as comprising particles governed by Newton's law of motion [19]. However, in molecular dynamics simulations of such a system, specifying the precise initial conditions for velocity $\mathbf{v}_i$ and position $\mathbf{x}_i$ for the individual particles is not feasible. Thus, instead of focusing on a single initial configuration of particles, one often considers an ensemble of initial conditions consistent with the system's macroscopic properties, such as mass density, velocity, temperature, pressure, and energy. For such an ensemble of particles, a probabilistic description is obtained by considering the particles' initial phase space distribution in terms of their position and momentum. This transition to the probabilistic description for a collection of N point particles is done via the Liouville equation which describes the evolution of the N particle density function $f^{(N)}(\mathbf{x}_1, \mathbf{v}_1, \cdots \mathbf{x}_N, \mathbf{v}_N, t)$ in the phase space. Here, $f^{(N)}(\mathbf{x}_1, \mathbf{v}_1, \cdots \mathbf{x}_N, \mathbf{v}_N, t)\, d\mathbf{x}_1 d\mathbf{v}_1 \cdots d\mathbf{x}_N d\mathbf{v}_N$ denotes the probability of finding 1st particle position in range $(\mathbf{x}_1, \mathbf{x}_1 + d\mathbf{x}_1)$ and the velocity in the range $(\mathbf{v}_1, \mathbf{v}_1 + d\mathbf{v}_1)$, second particle position in the range $(\mathbf{x}_2, \mathbf{x}_2 + d\mathbf{x}_2)$ and the velocity in the range $(\mathbf{v}_2, \mathbf{v}_2 + d\mathbf{v}_2)$ and so on at time t.

In this description, the evolution of macroscopic properties is derived through averaging over particle motion. As our interest lies in the average description, the dynamics represented by the N-particle distribution function are too detailed. Thus, it may be desirable to formulate the evolution equation for the one-particle distribution function $f^{(1)}(\mathbf{x}, \mathbf{v}, t)$, where $f^{(1)}(\mathbf{x}, \mathbf{v}, t)\, d\mathbf{x} d\mathbf{v}$ indicates the probability of locating a particle within the position range $(\mathbf{x}, \mathbf{x}+d\mathbf{x})$ and within the velocity range $(\mathbf{v}, \mathbf{v}+d\mathbf{v})$ at time t.

However, this evolution equation for a gas is not closed, as it requires knowledge of the two-particle distribution function. Similarly, the two-particle distribution function evolution equation requires knowledge of the three-particle distribution function, and so on. This infinite chain of equations is known as the Bogoliubov-Born-Green-Kirkwood-Yvon (BBGKY) hierarchy. However, in the case of a dilute gas, this hierarchy can be simplified, and a closed-form equation for the single-particle distribution function, called the Boltzmann equation, can be obtained. The Boltzmann equation is based on the dynamic variable $f^{(1)}(\mathbf{x}, \mathbf{v}, t)$, and it describes the transition from mesoscale Boltzmann description to the continuum description in terms of the NSF equation. The continuum description is valid in the limit of the vanishing mean free path. A multiscale description of the different levels of details is shown in Fig.4.4.

This thesis focuses on the dilute gas kinetic theory, which involves the use of the single-particle distribution $f^{(1)}(\mathbf{x}, \mathbf{v}, t)$, denoted as $f(\mathbf{x}, \mathbf{v}, t)$ for convenience from here on. While this description is adequate for monoatomic gases, it requires augmentation for polyatomic gases.

In this chapter, I define a few basic quantities used in kinetic theory and get estimates for transport properties such as viscosity and thermal conductivity for a dilute gas. To describe the transition from the kinetic theory of gases in terms of the single-particle distribution to the macroscopic NSF equation, it is important to define the relevant time and length scales which play crucial roles in the dynamics. In Section 2.2, a few key definitions of kinetic theory are presented. Estimates for transport properties are obtained in Section 2.3. Following this, Section 2.4 introduces the single-particle distribution function and its moments in the context of macroscopic hydrodynamics. Boltzmann equation for dilute gases is discussed in Section 2.5, which is followed by a description of the Maxwell-Boltzmann distribution function in Section 2.6. Finally, two of the most widely used collision models are presented in Section 2.7.

2.2 Time and Length Scale

A few relevant length and time scales for fluid flow phenomena are discussed in this section. Some important non-dimensional numbers that characterise the flow are defined. For example, an important length scale in the kinetic theory of gases is the mean free path (l_{mfp}), which

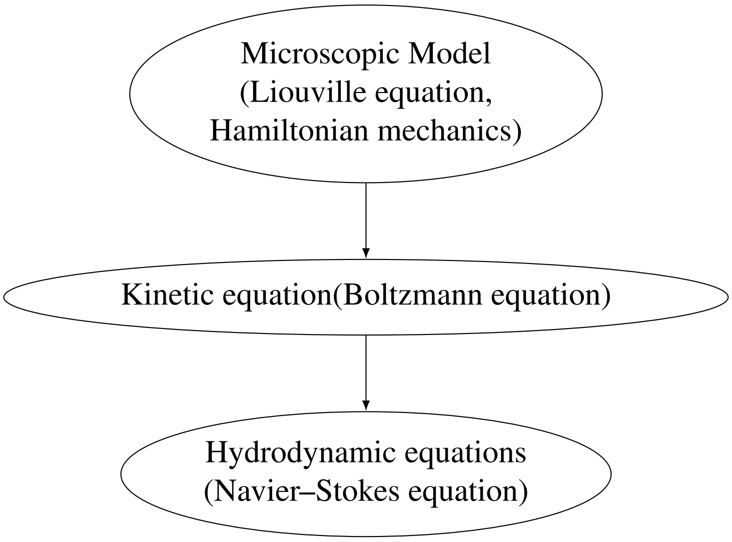

Fig. 2.1 Levels of modeling fluids

represents the average distance a gas molecule travels between successive collisions with other molecules. The mean free path in terms of the molecular diameter d and the number density n is

$$l_{\mathrm{mfp}} = \frac{1}{\sqrt{2}\pi d^2 n}. \tag{2.1}$$

It is often convenient to measure the mean free path in terms of the characteristic macroscopic length scale L. This is typically done by defining the dimensionless number Knudsen number as

$$\mathrm{Kn} = \frac{l_{\mathrm{mfp}}}{L}. \tag{2.2}$$

The continuum description of the NSF equation is valid in the limit of $\mathrm{Kn} \ll 1$.

For the single-component fluid motion, the following five time scales can be defined:

- **Mean free time** τ: The average time between these collisions is defined as mean free time. This can be obtained by noticing that the relevant velocity scale is the average thermal velocity $v_T = \sqrt{3k_{\mathrm{B}}T/m}$. Thus, one may define the mean free time as

  $$\tau = \frac{l_{\mathrm{mfp}}}{v_T}. \tag{2.3}$$

  The smallest time scale in kinetic theory, the collisonal time (inverse of collisonal frequency) for particles of diameter d can be estimated to be [126]

  $$\tau = \frac{1}{n\pi d^2 \bar{g}}, \tag{2.4}$$

where n is the particle number density and $\bar{g} = \sqrt{2}v_T$ is the relative speed between particle. Note that the factor $\sqrt{2}$ appears because the collision rate depends on the relative velocity between two particles and not on the velocity of a single molecule.

- **Acoustic time scale** t_a: The time taken for sound propagation of fluid over length L with isentropic sound speed $c_s = \sqrt{\gamma k_\mathrm{B} T/m}$ is

$$t_\mathrm{a} = \frac{L}{c_s} \equiv \frac{L}{\sqrt{\frac{\gamma k_\mathrm{B} T}{m}}} \tag{2.5}$$

  where γ is the specific heat ratio.

- **Momentum diffusion time scale** t_D: The time taken for the momentum to diffuse over length L in a fluid with kinematic viscosity ν is

$$t_\mathrm{D} = \frac{L^2}{\nu} \tag{2.6}$$

  Later, it will be shown that ν for a dilute gas is related to mean free time via the relation

$$\tau = \frac{\mu}{p} \tag{2.7}$$

  where μ is the kinematic viscosity p is a pressure.

- **Thermal diffusion time scale** t_{D_T}:The time taken for the momentum to diffuse over length L in a fluid with kinematic viscosity ν is

$$t_{D_T} = \frac{L^2}{\kappa/(\rho\, c_P)}, \tag{2.8}$$

  where ρ, κ and c_P are the density, thermal conductivity and specific heat at a constant pressure of the gas, respectively.

- **Convective time scale** t_U: The time taken for momentum propogation at a distance L via convection with characteristic fluid velocity as U is

$$t_\mathrm{U} = \frac{L}{U} \tag{2.9}$$

Based on these time scales, one can define several dimensionless numbers which characterize fluid motion. These are:

- **Reynolds Number**: The ratio of the viscous time scale and convective time scale is defined as the Reynolds number Re

  $$\mathrm{Re} = \frac{t_D}{t_U} = \frac{L^2/\nu}{L/U} \equiv \frac{\rho U L}{\mu}. \tag{2.10}$$

  Flows with high Reynolds numbers are characterized by the dominance of inertial forces and are often turbulent in nature. Such flows are relevant for applications in external aerodynamics, atmospheric flows, and many other areas. On the other hand, flows with low Reynolds numbers are characterized by the dominance of viscous forces and are usually laminar in nature. These flows are important for applications in microfluidics and biophysics.

- **Mach Number**: The ratio of the acoustic time scale and convective time scale is denoted as Mach number Ma

  $$\mathrm{Ma} = \frac{L/c_s}{L/U} \equiv \frac{U}{c_s}. \tag{2.11}$$

  Thus, it is evident that the Mach number is the ratio of the fluid velocity and the sound velocity. In general, for fluid flows, compressibility effects are important only if the Mach number is finite. In practice, many computational works consider regime of $\mathrm{Ma} < 0.1$ as incompressible. Compressibility effects becoming noticeable as Ma approaches 0.3. Thus, safely, one may say that for $\mathrm{Ma} < 0.05$, the compressibility effects are very weak and can be ignored.

- **Knudsen Number**: In terms of time scales, the Knudsen number relates the mean free time τ, a molecular time scale with the macroscopic acoustic time scale L/c_s.

  $$\mathrm{Kn} = \frac{l_{\mathrm{mfp}}}{L} = \frac{\tau c_s}{L}. \tag{2.12}$$

  It is evident that this is not independent of Reynolds and Mach number and can be rewritten via the Von Karman relation

  $$\mathrm{Kn} = \alpha \frac{\mathrm{Ma}}{\mathrm{Re}}, \tag{2.13}$$

  where α is a numerical constant.

Table 2.1 Prandtl number of selected gases at atmospheric pressure and temperature of $300K$. [58]

Fluid	**Pr**
Argon	0.668
Methane	0.739
Carbon dioxide	0.778
Hydrogen	0.71
Helium	0.668
Nitrogen	0.714
Oxygen	0.714

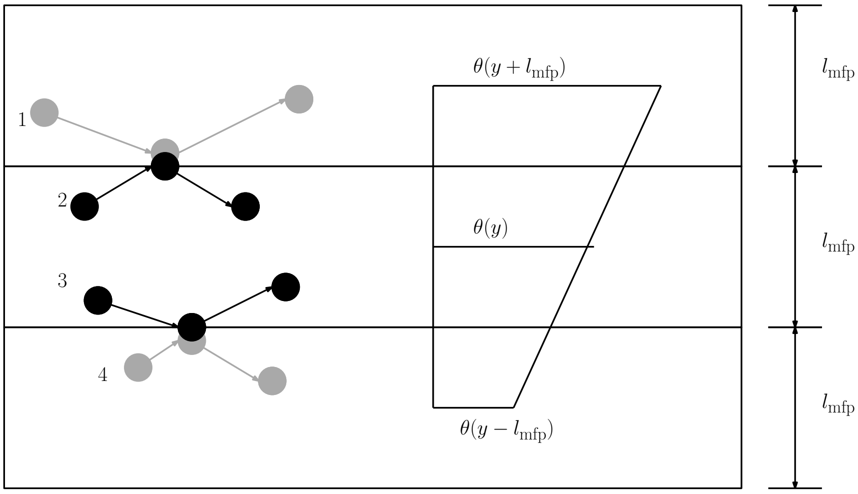

Fig. 2.2 Two infinite parallel plates at temperatures θ^+ and θ^-

- **Prandtl Number**: The ratio of the thermal diffusion time and the momentum diffusion time is called Pr

$$\mathrm{Pr} = \frac{t_{D_T}}{t_D} = \frac{\frac{L^2}{\kappa/(\rho\, c_P)}}{\frac{L^2}{\nu}} \implies \mathrm{Pr} = \frac{\mu\, c_P}{\kappa} \tag{2.14}$$

  Thus, it is evident that Prandtl number is a material property. Prantdl numbers of a few gases are listed in Table 2.1.

2.3 Estimates of transport coefficients

In this section, estimates of the transport coefficients - viscosity and thermal conductivity are obtained. Consider a gas in between two infinite parallel plates at temperatures θ^+ and θ^-. At steady state, the net energy transport though the surface $\theta(y)$ in figure 2.2, comes from particles coming from a neighbourhood of l_{mfp} in either directions with kinetic energy $3k_BT(y \pm l_{\mathrm{mfp}})/2$.

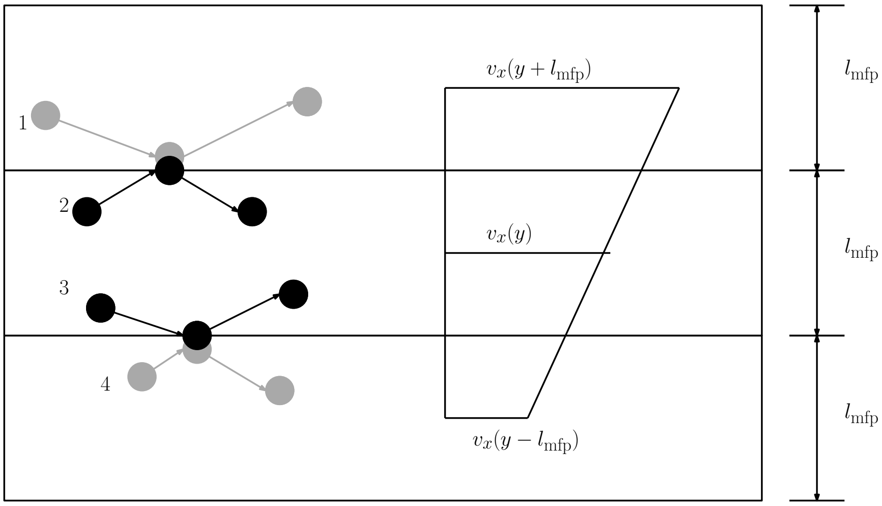

Fig. 2.3 Two infinite parallel plates: the bottom plate is stationary and the top plate is moving with a velocity v.

For a simple setup consisting of six directions of motion ($\pm x, \pm y, \pm z$), the flux of particles in one direction is $J = nv_T/6$. The heat flux through the surface can be estimated to be

$$q(y) = \frac{1}{6} n v_T \left[\frac{3}{2} k_B \theta (y - l_{\rm mfp}) - \frac{3}{2} k_B \theta (y + l_{\rm mfp}) \right]. \tag{2.15}$$

For small temperature gradients, applying a Taylor series expansion for temperature, the above equation can be simplified to be

$$q(y) = -\left(\frac{n v_T k_B l_{\rm mfp}}{2} \right) \frac{d\theta}{dy}. \tag{2.16}$$

Using the relations for $v_T = \sqrt{3k_BT/m}$ and mean free path, this recovers the Fourier's law of thermal conductivity $q = -\kappa \nabla T$ with

$$\kappa = \frac{k_B}{2\pi d^2} \sqrt{\frac{3}{2} \frac{k_B T}{m}}. \tag{2.17}$$

A similar analysis of the velocity gradient can be used to compute the viscosity. The momentum that crosses the surface $\mathrm{v}(y)$, in Figure 2.3, coming from regions $\mathrm{v}_x(y + l_{\rm mfp})$ and $\mathrm{v}_x(y - l_{\rm mfp})$ contribute to the stress tensor

$$\sigma_{xy} = -\frac{n v_T}{6} \left[m \mathrm{v}_x (y - l_{\rm mfp}) - \mathrm{v}_x (y + l_{\rm mfp}) \right]. \tag{2.18}$$

Using a Taylor expansion in velocity, Newton's law of viscous transport $\sigma_{xy} = -\mu \frac{d\mathrm{v}_x}{dy}$ can be recovered with

$$\mu = \frac{m}{3\pi d^2}\sqrt{\frac{3}{2}\frac{k_B T}{m}} \tag{2.19}$$

It should be noted that the above expression suggests that for a dilute-gas, kinematic viscosity is not a function of density.

Hence, mean-free path can be defined in terms of viscosity as

$$\lambda = \frac{\mu}{\rho}\sqrt{\frac{3m}{k_B T}} \tag{2.20}$$

Using the relations from equations 2.4 and 2.19, we have

$$\frac{\mu}{\tau} = n k_B T, \tag{2.21}$$

this can be simplified further to obtain the relation

$$\mu = \rho\tau\frac{k_B T}{m} \equiv p\tau \tag{2.22}$$

where $p = nmv_T^2/3$ is the pressure.

2.4 Distribution function and its moments

The dynamics of dilute monoatomic gases is well-described by the Boltzmann equation in terms of the evolution of the single-particle distribution function f, where $f(\boldsymbol{x},\boldsymbol{c},t)\,d\boldsymbol{x}d\boldsymbol{c}$ is the probability of finding a particle within $(\boldsymbol{x},\boldsymbol{x}+d\boldsymbol{x})$, possessing a velocity in the range $(\boldsymbol{c},\boldsymbol{c}+d\mathbf{c})$ at a time t. The hydrodynamic variables are density $\rho(\boldsymbol{x},t)$, velocity $\boldsymbol{u}(\boldsymbol{x},t)$ and total energy $E(\boldsymbol{x},t) = (\rho u^2 + 3\rho k_B T/m)/2$. Here onwards, a scaled temperature θ defined in terms of Boltzmann constant k_B and mass of the particle m as $\theta = k_B T/m$ is used. The thermodynamic pressure p and the scaled temperature θ are related via the ideal gas equation of state as $p = \rho\theta$. These hydrodynamic variables are computed as the moments of the single-particle distribution function

$$\{\rho,\rho\boldsymbol{u},E\} = \left\langle \left\{1,\boldsymbol{c},\frac{c^2}{2}\right\},f \right\rangle, \tag{2.23}$$

where the averaging operator is defined as $\langle \phi_1(\boldsymbol{c}), \phi_2(\boldsymbol{c}) \rangle = \int_{-\infty}^{\infty} \phi_1(\boldsymbol{c})\phi_2(\boldsymbol{c}) d\boldsymbol{c}$. In the comoving reference frame with fluctuating velocity $\boldsymbol{\xi} = \boldsymbol{c}$ - $\boldsymbol{u}$, the stress tensor $\sigma_{\alpha\beta}$ is traceless part of the flux of the momentum tensor $\Theta_{ij} \equiv \sigma_{\alpha\beta} + \rho\theta\delta_{\alpha\beta}$ and the heat flux q_α is the flux of the energy. Thus,

$$\Theta_{ij} \equiv \left\langle \xi_i \xi_j, f \right\rangle, \;\; \sigma_{\alpha\beta} = \left\langle \overline{\xi_\alpha \xi_\beta}, f \right\rangle, \quad q_\alpha = \left\langle \xi_\alpha \frac{\xi^2}{2}, f \right\rangle, \tag{2.24}$$

where the symmetrized traceless part $\overline{A_{\alpha\beta}}$ for any second-order tensor $A_{\alpha\beta}$ is $\overline{A_{\alpha\beta}} = \left(A_{\alpha\beta} + A_{\beta\alpha} - 2A_{\gamma\gamma}\delta_{\alpha\beta}/3\right)$ The stress tensor and heat flux tensor are related to the pressure tensor $P_{\alpha\beta} = \left\langle c_\alpha c_\beta, f \right\rangle$ and energy flux $\left\langle c^2 c_\alpha/2, f \right\rangle$ respectively as

$$\sigma_{\alpha\beta} = P_{\alpha\beta} - \rho u_\alpha u_\beta - \rho\theta\delta_{\alpha\beta}, \qquad q_\alpha = \left\langle \frac{c^2 c_\alpha}{2}, f \right\rangle - u_\alpha \left(E + \rho\theta\right) - u_\beta \sigma_{\alpha\beta}. \tag{2.25}$$

The third-order moment $Q_{\alpha\beta\gamma}$ with the traceless part $\overline{Q_{\alpha\beta\gamma}}$ are defined as

$$Q_{\alpha\beta\gamma} = \left\langle \xi_\alpha \xi_\beta \xi_\gamma, f \right\rangle, \quad \overline{Q_{\alpha\beta\gamma}} = Q_{\alpha\beta\gamma} - \frac{2}{5}\left(q_\alpha \delta_{\beta\gamma} + q_\beta \delta_{\alpha\gamma} + q_\gamma \delta_{\alpha\beta}\right). \tag{2.26}$$

For subsequent use, the fourth-order moment and its contracted parts are defined as $R_{\alpha\beta\gamma\delta} = \left\langle \xi_\alpha \xi_\beta \xi_\gamma \xi_\delta, f \right\rangle$, $R_{\alpha\beta} = \left\langle \xi^2 \xi_\alpha \xi_\beta, f \right\rangle$ with trace $R = \left\langle \xi^4, f \right\rangle$.

In the next section, Boltzmann equation for dilute gases is discussed.

2.5 Boltzmann equation for dilute gases

In the dilute gas limit, the time evolution of the distribution function is a sequence of free-flight and binary collisions well described by the Boltzmann equation

$$\partial_t f + c_\alpha \partial_\alpha f = \Omega(f, f), \tag{2.27}$$

where the collision kernel $\Omega(f, f)$ models the binary collisions between particles under the assumptions of molecular chaos [32, 35, 95]. The nonlinear integro-differential Boltzmann collision kernel is often replaced by simpler models that should recover the following essential features [32]:

(a) **Conservation Laws:** As the mass, momentum, and energy density of the particles are conserved during the elastic collision, any valid collision model must satisfy

$$\langle \Omega(f,f), \{1, \boldsymbol{c}, c^2\} \rangle = \{0, \boldsymbol{0}, 0\}. \tag{2.28}$$

Thus, the macroscopic conservation laws obtained by taking appropriate moments (with respect to $\{1, \boldsymbol{c}, c^2\}$) of the Boltzmann equation

$$\begin{aligned} &\partial_t \rho + \partial_\alpha (\rho u_\alpha) = 0, \\ &\partial_t (\rho u_\alpha) + \partial_\beta \left(\rho u_\alpha u_\beta + \rho \theta \delta_{\alpha\beta} + \sigma_{\alpha\beta}\right) = 0, \\ &\partial_t E + \partial_\alpha \left[(E + p)\, u_\alpha + q_\alpha + \sigma_{\alpha\beta} u_\beta\right] = 0, \end{aligned} \tag{2.29}$$

are the same as those of the compressible hydrodynamics.

(b) **Zero of collision:** The collision term is zero if and only if the distribution function attains Maxwell–Boltzmann form, i.e.,

$$\Omega(f,f) = 0 \iff f = f^{\mathrm{MB}}, \tag{2.30}$$

where the Maxwell–Boltzmann distribution f^{MB} is

$$f^{\mathrm{MB}}(\rho(f), \boldsymbol{u}(f), \theta(f)) = \rho \left(\frac{1}{2\pi\theta}\right)^{3/2} \exp\left(-\frac{(c-u)^2}{2\theta}\right), \tag{2.31}$$

which ensures that the dynamics is consistent with the equilibrium thermodynamics.

(c) **The H Theorem:** The Boltzmann equation generalizes the second law of thermodynamics to nonequilibrium situations. Boltzmann defined a nonequilibrium generalization of the entropy known as the H function [32]

$$H[f] = \int (f \ln f - f) dc. \tag{2.32}$$

At equilibrium, the thermodynamic entropy is calculated as [32]

$$S^{\mathrm{eq}} = -k_{\mathrm{B}} H[f^{\mathrm{MB}}] = -\rho k_B \left(\ln \frac{\rho}{(2\pi\theta)^{3/2}} - \frac{5}{2}\right). \tag{2.33}$$

The evolution of this H function is

$$\partial_t H + \partial_\alpha J^H_\alpha = \underbrace{\langle \Omega(f,f), \ln f \rangle}_{\Sigma} \leq 0, \tag{2.34}$$

where J^H_α is the entropy flux and Σ is the negative of the entropy generation. Boltzmann demonstrated that the entropy generation is positive, hence, the H function is nonincreasing in time [32]. Thus, any consistent approximation for the Boltzmann collision kernel should also satisfy the same condition.

2.6 Maxwell-Boltzmann distribution function

In the previous section, it was shown that the zero of the collision term is obtained by the Maxwell-Boltzmann distribution function where the entropy production is zero.

Hence, the Maxwell-Boltzmann distribution can be interpreted as the minimizer of H-function

$$H = \int f \log f dc, \tag{2.35}$$

under the constraints of mass , momentum and energy conservation as

$$\Xi = \int f(\ln f - 1) + f\left(\alpha + \beta_k c_k + \gamma c^2\right). \tag{2.36}$$

where α, β_k and γ are the Lagrange multipliers associated with mass, momentum and energy conservation constraints respectively.

The stationary point of Ξ gives us the equilibrium distribution function f^{eq},

$$\frac{d\,\Xi}{df} = 0 \equiv f^{MB} = \exp\left[-\left(\alpha + \beta_k c_k + \gamma c^2\right)\right]. \tag{2.37}$$

The equilibrium distribution can be evaluated to be

$$f^{MB}(\rho, u, \theta) = \frac{\rho}{(2\pi\theta)^{3/2}} \exp\left(\frac{(c-u)^2}{2\theta}\right) \tag{2.38}$$

using the exact form of Lagrange multipliers

$$\alpha = -\ln\rho + \frac{3}{2}\log(2\pi\theta) + u^2, \ \beta_k = -\frac{u_k}{\theta}, \text{and } \gamma = \frac{1}{2\theta}. \tag{2.39}$$

The moments of f^{MB} are the hydrodynamic variables are the density, momentum and energy

$$\left\langle \left\{1, \boldsymbol{c}, \frac{c^2}{2}\right\}, f^{MB} \right\rangle = \{\rho, \rho\boldsymbol{u}, E\}. \tag{2.40}$$

Of the many valid collision models — the Boltzmann collision model [32], BGK model [23], ES–BGK model [6, 63], the quasi-equilibrium models [56, 87], the Shakhov model [116], and the Fokker-Plank model [121, 123], the two most widely used models, the BGK collision model and the ES–BGK model are described in the next section.

2.7 Collision Models

In this section, the evolution equations and the transport coefficients for the BGK and ES–BGK models are derived.

2.7.1 BGK Model

The Bhatnagar–Gross–Krook (BGK) model, perhaps the simplest and most widely-used model of the Boltzmann collision kernel models the collision as a relaxation of the distribution function towards the equilibrium f^{MB} [23] as

$$\Omega_{\mathrm{BGK}} = \frac{1}{\tau}\left(f^{\mathrm{MB}}(\rho, \boldsymbol{u}, \theta) - f\right). \tag{2.41}$$

This assumes that the process occurs at a single time scale τ corresponding to the mean free time. It is trivial to see that this model has the same collisional invariants as the Boltzmann kernel, hence, recovers the same conservation laws [23]. The entropy production Σ^{BGK} due to the BGK model is written as

$$\Sigma^{\mathrm{BGK}} = \langle \Omega_{\mathrm{BGK}}, \ln f \rangle = \frac{1}{\tau}\int \left(f^{\mathrm{MB}}(\rho, \boldsymbol{u}, \theta) - f\right) \ln\left(\frac{f}{f^{\mathrm{MB}}(\rho, \boldsymbol{u}, \theta)}\right) d\boldsymbol{c} \leq 0. \tag{2.42}$$

Thus, like the Boltzmann equation, the BGK model also satisfies the H theorem. By taking appropriate moments of the Boltzmann BGK equation, we can also see that the evolution of the stress and the heat flux are [89]

$$
\begin{aligned}
\partial_t \sigma_{\alpha\beta} + \partial_\gamma \left(\sigma_{\alpha\beta} u_\gamma\right) + \partial_\gamma \overline{Q_{\alpha\beta\gamma}} + 2\overline{\sigma_{\gamma\beta}\partial_\gamma u_\alpha} + 2p\overline{\partial_\beta u_\alpha} + \frac{4}{5}\overline{\partial_\beta q_\alpha} &= -\frac{1}{\tau}\sigma_{\alpha\beta}, \\
\partial_t q_\alpha + \frac{1}{2}\partial_\beta \left(\overline{R_{\alpha\beta}} + \frac{1}{3} R\,\delta_{\alpha\beta}\right) + \overline{Q_{\alpha\beta\gamma}}\partial_\gamma u_\beta + \partial_\beta \left(q_\alpha u_\beta\right) + \frac{7}{5} q_\beta \partial_\beta u_\alpha & \\
+\frac{2}{5} q_\alpha \partial_\beta u_\beta + \frac{2}{5} q_\beta \partial_\alpha u_\beta - \frac{5}{2}\frac{p}{\rho}\partial_\alpha p - \frac{5}{2}\frac{p}{\rho}\partial_\beta \sigma_{\alpha\beta} - \frac{\sigma_{\alpha\beta}}{\rho}\partial_\beta p - \frac{\sigma_{\alpha\beta}}{\rho}\partial_\eta \sigma_{\beta\eta} &= -\frac{q_\alpha}{\tau}.
\end{aligned}
\tag{2.43}
$$

The form of relaxation dynamics shows that the time-scales for the momentum diffusivity and thermal diffusivity are equal for the BGK model. These equations show that, like any equation of Boltzmann type, the dynamics of M^{th} order moment involves $(M+1)^{th}$ moment and thus form an infinite order moment chain. The hydrodynamic limit is typically analysed via Chapman–Enskog expansion which allows evaluating the dynamic viscosity μ and thermal conductivity κ for the model with the specific heat C_p for a monoatomic ideal gas as $5/2$ is [2, 35]

$$
\mu = p\tau, \quad \kappa = \frac{5}{2} p\tau \quad \Longrightarrow \mathrm{Pr} = \frac{\mu C_p}{k} = 1. \tag{2.44}
$$

Despite this defect of $\mathrm{Pr} = 1$, the BGK model is extremely successful both as a numerical and an analytical tool for analysis.

2.7.2 ES–BGK Model

The ES–BGK model [62] also describes the collision as simple relaxation process but unlike the BGK model, it overcomes the restriction on the Prandtl number. The extra ingredient for ES–BGK model is quasi-equilibrium form of distribution derived by minimizing the H–function (Eq.(2.32)) under the constraints of an additional condition of fixed stresses, which implies absolute minimization of

$$
\Xi[f] = \int d\mathbf{c} \left[(f \ln f - f) + \alpha f + \beta_j c_j f + \gamma_{ij} c_i c_j f\right]. \tag{2.45}
$$

The solution to this minimization problem is an anisotropic Gaussian

$$
f^{\mathrm{Quasi}}\left(\rho, \boldsymbol{u}, \Theta_{ij}\right) = \frac{\rho}{\sqrt{\det[2\pi\Theta_{\mathrm{ij}}]}} \exp\left(-\frac{1}{2}\xi_i \Theta_{ij}^{-1} \xi_j\right). \tag{2.46}
$$

Like the MB distribution, this has the same conserved moments as that of the single-particle distribution function but this also treats $\Theta_{ij}(f)$ as a conserved variable [74] i.e.,

$$\{\rho(f^{\text{Quasi}}), u_\alpha(f^{\text{Quasi}}), \theta(f^{\text{Quasi}}), \Theta_{ij}(f^{\text{Quasi}})\} = \{\rho(f), u_\alpha(f), \theta(f), \Theta_{ij}(f)\}. \tag{2.47}$$

On this quasi-equilibrium manifold with stress as variable when the H is minimum we have

$$H[f^{\text{Quasi}}(\rho, \boldsymbol{u}, \Theta_{ij})] = \rho \ln\left(\frac{\rho}{\sqrt{\det[2\pi\Theta_{\text{ij}}]}}\right) - \frac{5}{2}\rho. \tag{2.48}$$

The ES–BGK model uses the anisotropic Gaussian distribution $f^{\text{ES}} \equiv f^{\text{Quasi}}(\rho, \boldsymbol{u}, \lambda_{ij})$

$$f^{\text{ES}}(\rho, \boldsymbol{u}, \lambda_{ij}) = \frac{\rho}{\sqrt{\det[2\pi\lambda_{\text{ij}}]}} \exp\left(-\frac{1}{2}\xi_i \lambda_{ij}^{-1} \xi_j\right), \tag{2.49}$$

where instead of pressure tensor a positive definite matrix λ_{ij}

$$\lambda_{ij} = (1-b)\theta\delta_{ij} + b\Theta_{ij} \equiv \theta\delta_{ij} + b\sigma_{ij}, \tag{2.50}$$

is used with $-1/2 \le b \le 1$ as a free parameter, the range of b is dictated by the positive definiteness of λ_{ij}^{-1}. For $0 \le b \le 1$, λ_{ij} is trivially positive as it is a convex combination of two positive definite matrices. The non-trivial range $-1/2 \le b < 0$ is better understood from the eigenvalue analysis of λ_{ij} [6]. Let the eigenvalues of λ_{ij} be Λ_i and that of positive definite matrix Θ_{ij} be ϕ_i and thus $\phi_1 + \phi_2 + \phi_3 = \Lambda_1 + \Lambda_2 + \Lambda_3 = 3\theta$. In terms of these eigenvalues, the matrix $\boldsymbol{\lambda}$ after suitable rotation can be rewritten as

$$\boldsymbol{\lambda} = \begin{pmatrix} (1-b)\theta + b\phi_1 & 0 & 0 \\ 0 & (1-b)\theta + b\phi_2 & 0 \\ 0 & 0 & (1-b)\theta + b\phi_3 \end{pmatrix}, \tag{2.51}$$

which is a convex combination of diagonal matrices Ψ_1, Ψ_2 and Ψ_3 as

$$\boldsymbol{\lambda} = \frac{1+2b}{3} \underbrace{\begin{pmatrix} \phi_1 & 0 & 0 \\ 0 & \phi_2 & 0 \\ 0 & 0 & \phi_3 \end{pmatrix}}_{\Psi_1} + \frac{1-b}{3} \underbrace{\begin{pmatrix} \phi_2 & 0 & 0 \\ 0 & \phi_3 & 0 \\ 0 & 0 & \phi_1 \end{pmatrix}}_{\Psi_2} + \frac{1-b}{3} \underbrace{\begin{pmatrix} \phi_3 & 0 & 0 \\ 0 & \phi_1 & 0 \\ 0 & 0 & \phi_2 \end{pmatrix}}_{\Psi_3}. \tag{2.52}$$

As in the diagonal representation, the non-zero components are the eigenvalues and one obtains the relationship between ϕ_i and Λ_i as

$$\Lambda_i = \frac{1+2b}{3}\phi_i + \frac{1-b}{3}\sum_{i\neq j}\phi_j. \tag{2.53}$$

Thus, the eigenvalues of λ_{ij} are non-negative if the range of b is restricted to $-1/2 \leq b \leq 1$ as we also know that $\phi_i \geq 0$. In the ES–BGK model, the collisional relaxation is towards this anisotropic Gaussian distribution f^{ES} which itself attains the form of the Maxwellian at the equilibrium. The collision kernel in explicit form is

$$\Omega_{\mathrm{ESBGK}} = \frac{1}{\tau}\left(f^{\mathrm{ES}}\left(\rho,\boldsymbol{u},\lambda_{ij}\right) - f\right), \tag{2.54}$$

where it is evident that $b=0$ corresponds to the limit of the BGK equation and $b=1$ would imply that stress is conserved. For $b\neq 1$, the model has the same set of conservation laws as the BGK equation. As the stress and heat flux tensors follow the relation

$$\sigma_{\alpha\beta}(f^{\mathrm{ES}}) = b\sigma_{\alpha\beta}(f), \quad \left\langle \xi_\alpha\xi^2, f^{\mathrm{ES}}\right\rangle = 0, \tag{2.55}$$

thus, the evolution equations for stress tensor and heat flux are

$$\begin{aligned}
\partial_t\sigma_{\alpha\beta} + \partial_\gamma\left(u_\gamma\sigma_{\alpha\beta}\right) + \partial_\gamma\overline{Q_{\alpha\beta\gamma}} + 2\overline{\sigma_{\gamma\beta}\partial_\gamma u_\alpha} + 2p\overline{\partial_\beta u_\alpha} + \frac{4}{5}\overline{\partial_\beta q_\alpha} &= -\left(\frac{1-b}{\tau}\right)\sigma_{\alpha\beta},\\
\partial_t q_\alpha + \frac{1}{2}\partial_\beta\left(\overline{R_{\alpha\beta}} + \frac{1}{3}R\,\delta_{\alpha\beta}\right) + \overline{Q_{\alpha\beta\gamma}}\partial_\gamma u_\beta + \partial_\beta\left(q_\alpha u_\beta\right) + \frac{7}{5}q_\beta\partial_\beta u_\alpha&\\
+\frac{2}{5}q_\alpha\partial_\beta u_\beta + \frac{2}{5}q_\beta\partial_\alpha u_\beta - \frac{5}{2}\frac{p}{\rho}\partial_\alpha p - \frac{5}{2}\frac{p}{\rho}\partial_\beta\sigma_{\alpha\beta} - \frac{\sigma_{\alpha\beta}}{\rho}\partial_\beta p - \frac{\sigma_{\alpha\beta}}{\rho}\partial_\eta\sigma_{\beta\eta} &= -\frac{q_\alpha}{\tau},
\end{aligned} \tag{2.56}$$

which shows that the momentum and thermal diffusivities are different in an ES–BGK model and the Prandtl number $\mathrm{Pr} = \mu c_p/\kappa$ is a free parameter. In particular, the Chapman-Enskog analysis of this model yields

$$\mu = \frac{p\tau}{1-b}, \quad \kappa = \frac{5}{2}p\tau \quad \Longrightarrow \mathrm{Pr} = \frac{1}{1-b}. \tag{2.57}$$

Thus, the free parameter b in the anisotropic Gaussian allows one to vary the Prandtl number from $2/3$ to infinity. At $b=-1/2$, the Prandtl number predicted by the ES–BGK model is $2/3$, which matches with the value obtained from the Boltzmann equation, and when $b=0$, the model is equivalent to the BGK model. The thermal conductivity is fixed only by τ while the viscosity can be tuned via b to obtain the required Prandtl number.

The H theorem for this model was first proved by Andries et al. [6] by showing that the entropy production Σ^{ESBGK} is non-positive. The expression for the entropy production is

$$\Sigma^{\text{ESBGK}} = \langle \Omega_{\text{ESBGK}}, \ln f \rangle = \frac{1}{\tau} \left\langle \left(f^{\text{ES}} \left(\rho, \boldsymbol{u}, \lambda_{ij}\right) - f \right), \frac{\partial H}{\partial f} \right\rangle. \tag{2.58}$$

The proof is built on the property of an arbitrary convex function $G(x)$ that

$$\frac{\partial G}{\partial x}(y-x) \leq G(y) - G(x) \tag{2.59}$$

using which we can write

$$\Sigma^{\text{ESBGK}} \leq \frac{1}{\tau} \left(H[f^{\text{ES}}\left(\rho, \boldsymbol{u}, \lambda_{ij}\right)] - H\left[f^{\text{Quasi}}\left(\rho, \boldsymbol{u}, \Theta_{ij}\right)\right]\right) + \frac{1}{\tau}\Delta H^{\text{Quasi}}, \tag{2.60}$$

with the last term as $\Delta H^{\text{Quasi}} = H[f^{\text{ES}}\left(\rho, \boldsymbol{u}, \Theta_{ij}\right)] - H[f]$ in the above equation is non-positive as $f^{\text{Quasi}}\left(\rho, \boldsymbol{u}, \Theta_{ij}\right)$ is by construction the minima of H. To prove that $H[f^{\text{ES}}\left(\rho, \boldsymbol{u}, \lambda_{ij}\right)] - H\left[f^{\text{Quasi}}\left(\rho, \boldsymbol{u}, \Theta_{ij}\right)\right] \leq 0$, using Eq.(2.48) we have

$$H[f^{\text{ES}}\left(\rho, \boldsymbol{u}, \lambda_{ij}\right)] - H\left[f^{\text{Quasi}}\left(\rho, \boldsymbol{u}, \Theta_{ij}\right)\right] = \frac{1}{2}\rho \ln\left(\frac{\det[\Theta_{ij}]}{\det[\lambda_{ij}]}\right). \tag{2.61}$$

Starting from the Brunn-Minkowsky inequality

$$\det[aA + (1-a)B] \geq (\det[A])^{a} (\det[B])^{1-a}, \tag{2.62}$$

relating the determinants of two positive matrices A and B and their convex combinations, we can show that $\det[\lambda_{ij}] \geq \det[\Theta_{ij}]$ [64]. This inequality along with Eq.(2.52) allows us to write

$$\det[\lambda_{ij}] \geq (\det[\Psi_1])^{\frac{1+2b}{3}} (\det[\Psi_2])^{\frac{1-b}{3}} (\det[\Psi_3])^{\frac{1-b}{3}}. \tag{2.63}$$

However, from the definitions of Ψ_1, Ψ_2, and Ψ_3 one can see that

$$\det[\Psi_1] = \det[\Psi_2] = \det[\Psi_3] = \phi_1\phi_2\phi_3 = \det[\Theta_{ij}]. \tag{2.64}$$

Hence, the total entropy production is non-positive, i.e., $\Sigma^{\text{ESBGK}} \leq 0$.

Chapter 3

Lattice Boltzmann model for weakly compressible flows

In this chapter*, we propose an energy conserving multispeed LBM with 41 discrete velocities in three dimensions that is relevant for acoustics and weakly compressible flows. We list the conditions on the equilibrium for the discrete velocity models to recover the Navier-Stokes-Fourier equations as the hydrodynamic limit. We also discuss the importance of the cubic accuracy in recovering the Navier-Stokes hydrodynamics. We develop the LB model based on recently proposed crystallographic lattice Boltzmann framework using a bcc lattice [101]. It was shown that the bcc lattice gives better spatial accuracy in addition to more accuracy in the velocity space, in comparison to a simple cubic (sc) lattice. We outline the procedure for the development of the discrete equilibrium using entropic formulation by a series expansion at the reference state with zero velocity and zero temperature variation. First, the equilibrium at a rest state is derived for non-zero variation in temperature, and a non-zero velocity equilibrium is derived as a series expansion around the earlier reference state. This expansion is more stable than a direct two variable (Mach number and deviation from reference temperature) expansion. Finally, we show the capability of the new model to perform aeroacoustic, thermal, thermoacoustic and turbulent simulations by presenting a number of benchmark simulations.

This chapter is structured as follows: In Sec. 3.1 we describe the lattice Boltzmann method briefly and define the restrictions on the discrete velocity model to recover isothermal compressible hydrodynamics. This is followed by a derivation of a compressible thermo-hydrodynamic

---

*Work presented in this chapter has been published in Physical Review E, Volume 101, Page 013309, in an article titled “Lattice Boltzmann model for weakly compressible flows” ©2020 American Physical Society.
This publication has been highlighted as Editors’ Suggestion

model and constraints for such a model in Sec. 3.2. A brief description on recently proposed class of crystallographic lattice Boltzmann models and followed by the construction of a new LB model, RD3Q41 model, with 41 velocities on a bcc lattice is given in Sec. 3.3. An energy conserving equilibrium distribution function is derived for the proposed RD3Q41 model in Sec. 3.4. We show the capability of this model for simulating acoustic phenomena in Sec. 3.5, followed by a few test cases to demonstrate its ability to simulate thermal flows in Sec. 3.6. A nontrivial problem involving both thermal and acoustic phenomena is presented in Sec. 3.7. Further, in Sec. 3.8 we show that the proposed model is also advantageous for multiphase flows on account of it being more accurate in the velocity space. Finally, we simulate a few turbulent flows at high Reynolds numbers like the Kida-Peltz flow, flow in a rectangular channel and flow past a sphere in Sec. 3.9.

3.1 Lattice Boltzmann Method

The lattice Boltzmann method (LBM) with its simplified kinetic picture on a D-dimensional lattice provides a computationally efficient description of hydrodynamics [40, 127]. In this section, we briefly review the method and the basic motivation behind its use for simulating hydrodynamics. In LBM, the velocity space is discretized to a finite set $\mathscr{C} = \{\mathbf{c}_i, i = 1..N_d\}$ and one associates a discrete population $f_i \in \mathbf{f}$ with each $\mathbf{c}_i$. The discrete populations $f(\mathbf{c}_i, \mathbf{x}, t) \equiv f_i(\mathbf{x}, t)$ are considered a function of location $\mathbf{x}$ and time t. The set $\mathscr{C}$ is chosen to satisfy an appropriate set of symmetries needed to recover hydrodynamics from the evolution equation of f_i in the long time limit [144]. The hydrodynamic variables such as the mass density ρ, velocity $\mathbf{u}$, and the energy E are defined as

$$\rho = \langle f, 1 \rangle, \quad \mathbf{j} \equiv \rho \mathbf{u} = \langle f, \mathbf{c} \rangle, \quad E = \left\langle f, \frac{\mathbf{c}^2}{2} \right\rangle, \tag{3.1}$$

where the inner product between two functions of discrete velocities ϕ and ψ is defined as

$$\langle \phi, \psi \rangle = \sum_{i=1}^{N_d} \phi_i \psi_i. \tag{3.2}$$

In a three dimensional space ($D = 3$), the energy is that of the ideal gas i.e. $E = (\rho u^2 + 3\rho\theta)/2$. Using this relation, one can obtain temperature θ from total energy E (Eq. 3.1) as $\theta = (2E - \rho u^2)/(3\rho)$. A few higher order moments which are relevant to the hydrodynamic description are momentum flux as $P_{\alpha\beta} = \left\langle f, \mathbf{c}_\alpha \mathbf{c}_\beta \right\rangle$, flux of momentum flux as $Q_{\alpha\beta\gamma} = \left\langle f, \mathbf{c}_\alpha \mathbf{c}_\beta \mathbf{c}_\gamma \right\rangle$. The fluctuating velocity $\boldsymbol{\xi}$ is defined as $\mathbf{c} - \mathbf{u}$ and the heat flux as $q_\alpha = \left\langle f, \xi_\alpha \xi^2/2 \right\rangle$ and the flux of heat flux as $R_{\alpha\beta} = \left\langle f, \xi^2 \xi_\alpha \xi_\beta \right\rangle$.

Typically, one works with the discrete in space and time version of the kinetic evolution equation in the Boltzmann Bhatnagar-Gross-Krook (BGK) form [23] as

$$f_i(\mathbf{x} + \mathbf{c}_i \Delta t, t + \Delta t) = f_i(\mathbf{x}, t) + 2\beta \left[f_i^{\text{eq}}(\rho(\mathbf{f}), \mathbf{u}(\mathbf{f})) - f_i(\mathbf{x}, t) \right], \tag{3.3}$$

where f_i^{eq} represent discrete form of the Maxwell-Boltzmann equilibrium, Δt is the chosen time step and $\beta = \Delta t/(2\tau + \Delta t)$ with τ as the mean free time. The dimensionless parameter β, bounded in the interval $0 < \beta < 1$ with $\beta = 1$ as the dissipation-less state, physically represents the discrete dimensionless relaxation towards the equilibrium. Here, the choice of the discrete version of equilibrium distribution f_i^{eq} is crucial for recovering the correct hydrodynamic limit and different formulations of lattice Boltzmann models differ mainly in the choice of this discrete equilibrium [12, 136]. A common choice is to project the Maxwell-Boltzmann distribution on the Hermite basis to get a computationally attractive polynomial expression of the equilibrium as [20, 38, 108, 119]

$$f_i^{\text{eq}}(\rho, \mathbf{u}) = w_i \rho \left[1 + \frac{u_\alpha c_{i\alpha}}{\theta_0} + \frac{u_\alpha u_\beta}{2\,\theta_0^2} \left(c_{i\alpha} c_{i\beta} - \theta_0 \delta_{\alpha\beta} \right) \right], \tag{3.4}$$

where θ_0 is some reference temperature associated with the underlying lattice and w_i are the weights chosen in such a way that the mass and momentum constraints are ensured, i.e.,

$$\sum_{i=1}^{N_d} f_i^{\text{eq}} = \rho, \qquad \sum_{i=1}^{N_d} f_i^{\text{eq}} c_{i\alpha} = j_\alpha. \tag{3.5}$$

Furthermore, to get correct hydrodynamic limit for isothermal low Mach number dynamics, it is essential to ensure that the second moment of the discrete equilibrium is the same as that obtained from the Maxwell-Boltzmann distribution, i.e.,

$$P_{\alpha\beta}^{\text{eq}} = \sum_{i=1}^{N_d} f_i^{\text{eq}} c_{i\alpha} c_{i\beta} = \rho u_\alpha u_\beta + \rho \theta_0 \delta_{\alpha\beta}. \tag{3.6}$$

The rationale for adding Eq. (3.6) can be understood by writing first the kinetic equation in its partial differential form (PDE) form (for $\Delta t \to 0$) [45, 50, 144] as

$$\partial_t f_i + c_{i\alpha}\partial_\alpha f_i = -\frac{1}{\tau}\left[f_i - f_i^{\mathrm{eq}}\right], \tag{3.7}$$

from which one can write the mass and momentum conservation laws as

$$\begin{aligned} \partial_t \rho + \partial_\alpha j_\alpha &= 0, \\ \partial_t j_\alpha + \partial_\beta P_{\alpha\beta} &= 0. \end{aligned} \tag{3.8}$$

The evolution equation for the pressure tensor $P_{\alpha\beta}$ using Eq.(3.6) and Eq.(3.7) as

$$\partial_t P_{\alpha\beta} + \partial_\gamma Q_{\alpha\beta\gamma} = \frac{1}{\tau}\left(\rho u_\alpha u_\beta + \rho\theta_0\delta_{\alpha\beta} - P_{\alpha\beta}\right), \tag{3.9}$$

from which it is evident that in the limit of $\tau \to 0$, $P_{\alpha\beta} \to \rho u_\alpha u_\beta + \rho\theta_0\delta_{\alpha\beta}$ and thus the zeroth order hydrodynamic equation describes the inviscid hydrodynamics as given by the Euler equation. The Navier-Stokes hydrodynamics is recovered provided [108, 143, 44]

$$\sum_i^{N_d} f_i^{\mathrm{eq}} c_{i\alpha}c_{i\beta}c_{i\gamma} = \rho u_\alpha u_\beta u_\gamma + \rho\theta_0\left(u_\alpha\delta_{\beta\gamma} + u_\beta\delta_{\alpha\gamma} + u_\gamma\delta_{\alpha\beta}\right). \tag{3.10}$$

In most of the widely used lower order lattice Boltzmann models the above condition is satisfied only only up to linear order in velocity due to the absence of the cubic term in the equilibrium represented by Eq.(3.4) [109]. The Eq.(3.4) along with Eqs.(3.5),(3.6) imply that the discrete velocity set and associated weights should satisfy

$$\begin{gathered} \sum_{i=1}^{N_d} w_i = 1, \quad \sum_{i=1}^{N_d} w_i c_{i\alpha}c_{i\beta} = \theta_0\delta_{\alpha\beta}, \\ \sum_{i=1}^{N_d} w_i c_{i\alpha}c_{i\beta}c_{i\gamma}c_{i\zeta} = \theta_0^2\Delta_{\alpha\beta\gamma\zeta}, \end{gathered} \tag{3.11}$$

where $\Delta_{\alpha\beta\gamma\zeta} = \delta_{\alpha\beta}\delta_{\gamma\zeta} + \delta_{\alpha\gamma}\delta_{\beta\zeta} + \delta_{\alpha\zeta}\delta_{\beta\gamma}$ is the fourth-order isotropic tensor and all odd order moments, such as

$$\begin{gathered}\sum_{i=1}^{N_d} w_i c_{i\alpha} = 0, \quad \sum_{i=1}^{N_d} w_i c_{i\alpha} c_{i\beta} c_{i\gamma} = 0, \\ \sum_{i=1}^{N_d} w_i c_{i\alpha} c_{i\beta} c_{i\gamma} c_{i\kappa} c_{i\zeta} = 0,\end{gathered} \tag{3.12}$$

are zero. These conditions are central to models for isothermal incompressible hydrodynamics, and the procedure to construct them is well understood [127]. It should be noted here that in case of compressible hydrodynamics, moment chain suggests that one needs to add $\mathcal{O}(u^3)$ contribution in the equilibrium distribution so that Eq.(3.10) is satisfied. This condition on the third moment can be fulfilled only if the discrete equilibrium distribution is of the form [45],

$$\begin{aligned} f_i^{\text{eq}} = w_i \Bigg(1 + \frac{u_\alpha c_{i\alpha}}{\theta_0} + \frac{u_\alpha u_\beta}{2\,\theta_0^2} \left(c_{i\alpha} c_{i\beta} - \theta_0 \delta_{\alpha\beta} \right) \\ + \frac{u_\alpha u_\beta u_\gamma c_{i\gamma}}{6\,\theta_0^3} \left(c_{i\alpha} c_{i\beta} - 3\theta_0 \delta_{\alpha\beta} \right) \Bigg). \end{aligned} \tag{3.13}$$

This adds further restriction on the weights as

$$\sum_{i=1}^{N_d} w_i c_{i\alpha} c_{i\beta} c_{i\gamma} c_{i\kappa} c_{i\zeta} c_{i\eta} = \theta_0^3 \Delta_{\alpha\beta\gamma\kappa\zeta\eta}, \tag{3.14}$$

where $\Delta_{\alpha\beta\gamma\kappa\zeta\eta}$ is the sixth-order isotropic tensor [144]. However, only very high-order on-lattice models are known to satisfy such constraint in 3-dimensions [45, 120]. In practice, it is easier to satisfy the contracted version of Eq. (3.10)

$$\sum_{i=1}^{N_d} f_i^{\text{eq}} c_i^2 c_{i\alpha} = \rho u_\alpha u^2 + (D+2)\,\rho\,\theta_0\, u_\alpha, \tag{3.15}$$

which requires only

$$\sum_{i=1}^{N_d} w_i c_i^2\, c_{i\alpha} c_{i\beta} c_{i\gamma} c_{i\kappa} = 7\theta_0^3 \Delta_{\alpha\beta\gamma\kappa}. \tag{3.16}$$

The above condition only ensures that the evolution equation for the energy is correct to the leading order. In this work, we will consider Eq. (3.15) and Eq.(3.16) as a requirement on higher-order LBM.

3.2 Compressible Thermo-hydrodynamics

In the previous section, the requirements for constructing a model for isothermal compressible hydrodynamics and the importance of the cubic accuracy in recovering the Navier-Stokes hydrodynamics has been described. It is known that on higher-order lattices such cubic accuracy can be imposed [42, 144]. However, typically, this has been done in an isothermal setting. A drawback of such models, though, is that the isentropic speed of sound is not recovered and they also lack the coupling between thermal and acoustic modes [122]. These aspects have not got enough attention in the development of new LB models.

The coupling between thermal and acoustic modes requires an accurate description of heat flux [89, 110]. In particular, in the limit of low Knudsen number, one most recover Fourier dynamics. Hence, Navier-Stokes-Fourier dynamics should be recovered as the first order hydrodynamic description in the compressible models with energy conservation.

For the Chapman-Enskog analysis, the distribution function and time derivative are expanded in powers of smallness parameter τ as

$$f = f^{(0)} + \tau f^{(1)} + \cdots \tag{3.17}$$

$$\partial_t \phi = \partial_t^{(0)} \phi + \tau \partial_t^{(1)} \phi + \cdots . \tag{3.18}$$

The heat flux is given by Fourier law via Chapman-Enskog analysis provided that the evolution for the energy flux

$$\partial_t q_\alpha + \partial_\beta R_{\alpha\beta} = \frac{1}{\tau}\left(q_\alpha^{\mathrm{eq}} - q_\alpha\right), \tag{3.19}$$

is correct at the leading order

$$\partial_t^{(0)} q_\alpha^{\mathrm{eq}} + \partial_\beta R_{\alpha\beta}^{\mathrm{eq}} = \frac{1}{\tau}\left(-q_\alpha^{\mathrm{neq}}\right). \tag{3.20}$$

Since only the trace of the equilibrium of the fourth-order moment in the Maxwell-Boltzmann form appears in the balance equation of heat flux we only need to ensure

$$R_{\alpha\beta}^{\mathrm{eq}}(\mathbf{u}=0) = 5\rho\theta^2\delta_{\alpha\beta}, \tag{3.21}$$

to get the evolution of heat flux at least to be quadratically correct in terms of $\Delta\theta = \theta/\theta_0 - 1$, the dimensionless departure of θ from θ_0.

In order to ensure that $R_{\alpha\beta}$ satisfy Eq.(3.21), we write the equilibrium at $u = 0$, as

$$\tilde{f}_i = w_i\rho\left[1 + \frac{\Delta\theta}{2}\left(\frac{c_i^2}{\theta_0} - 3\right) + \frac{\Delta^2\theta}{8}\left(\frac{c_i^4}{\theta_0^2} - 10\frac{c_i^2}{\theta_0} + 15\right)\right]. \tag{3.22}$$

The expected value of $R^{\text{eq}}_{\alpha\beta}$ computed with this equilibrium matches the required value

$$R^{\text{eq}}_{\alpha\beta}(\mathbf{u} = 0) = 5\rho\theta_0^2\delta_{\alpha\beta}\left(1 + 2\Delta\theta + \Delta\theta^2\right) = 5\rho\theta^2\delta_{\alpha\beta}, \tag{3.23}$$

provided the model satisfies

$$\sum_{i=1}^{N_d} w_i c_i^8 = 945\theta_0^4. \tag{3.24}$$

This condition is often not considered by some extensions of LBM where the cubic moment is imposed [45, 94]. An exception is a model RD3Q67 model with 67 discrete velocities [18].

Thus, we look for LB models which satisfy Eq.(3.11), Eq.(3.16) and Eq.(3.24). These tensorial set of equations can be simplified further for the class of discrete velocity models with the discrete velocity set $\mathbf{c}$ which ensure isotropy and avoid preference to any direction in particular. These discrete velocity sets should have the properties of closure under inversion (if $c_i \in \mathbf{c}$ then $-c_i \in \mathbf{c}$) and closure under reflection (if $c_i(c_{ix}, c_{iy}, c_{iz}) \in \mathbf{c}$ then all possible reflections of $c_i \in \mathbf{c}$) to ensure that any vector $\psi(\mathbf{cc})$ in the discrete case we have

$$\begin{aligned}
&\langle \psi, c_x^{2n}\rangle = \langle \psi, c_y^{2n}\rangle = \langle \psi, c_z^{2n}\rangle,\\
&\langle \psi, c_x^{2n}c_y^{2m}\rangle = \langle \psi, c_y^{2n}c_z^{2m}\rangle = \langle \psi, c_z^{2n}c_x^{2m}\rangle,\\
&\langle \psi, c_x^{2n+1}\rangle = \langle \psi, c_y^{2n+1}\rangle = \langle \psi, c_z^{2n+1}\rangle = 0,
\end{aligned} \tag{3.25}$$

where n and m are the natural numbers [144].

The above constraints on the discrete velocity set along with Eq.(3.11), Eq.(3.16) and Eq.(3.24) give us the following set of seven equations as the constraints on the weights for the proposed model as

$$\begin{aligned}&\sum w_i = 1 \quad \sum w_i c_{ix}^2 = \theta_0 \quad \sum w_i c_{ix}^4 = 3\theta_0^2\\ &\sum w_i c_{ix}^2 c_{iy}^2 = \theta_0^2 \quad \sum w_i c_{ix}^4 c_i^2 = 21\theta_0^3\\ &\sum w_i c_{ix}^2 c_i^4 = 35\theta_0^3 \quad \sum w_i c_i^8 = 945\theta_0^4.\end{aligned} \tag{3.26}$$

As reference temperature θ_0 is not specified and is an unknown, we have six more additional degrees of freedom. Hence, to obtain an on-lattice model we need six energy shells each with a weight w_i to solve the system of equations exactly. Furthermore, these weights should be positive.

To summarize, the thermohydrodynamic equations for the proposed weakly compressible model are

$$\begin{aligned}&\partial_t \rho + \partial_\alpha (\rho u_\alpha) = 0,\\ &\partial_t (\rho u_\alpha) + \partial_\beta \left(P_{\alpha\beta}^{eq} + \sigma_{\alpha\beta}\right) = 0,\\ &\partial_t E + \partial_\alpha \left[(E+p)\, u_\alpha + q_\alpha^{eq} + \sigma_{\alpha\beta} u_\beta\right] = 0.\end{aligned} \tag{3.27}$$

The moments of the equilibrium distribution from series expansion have errors of the order $P_{\alpha\beta}^{eq} = P_{\alpha\beta}^{MB} + \mathcal{O}(u^2\eta^3)$ and $q_\alpha^{eq} = q_\alpha^{MB} + \mathcal{O}(u^3\eta^3)$ respectively with the moments of the Maxwell-Boltzmann distribution. It should be noted that the Prandl number is fixed at unity, with the definitions of the dynamic viscosity μ, thermal conductivity κ with the specific heat C_p for a monoatomic ideal gas as $5/2$ being

$$\mu = p\tau, \quad \kappa = \frac{5}{2} p\tau \quad \Longrightarrow \mathrm{Pr} = \frac{\mu C_p}{k} = 1. \tag{3.28}$$

3.3 Crystallographic lattice Boltzmann model

Historically, the lattice chosen for the LBM has been the simple cubic (sc) lattice which demands that the grid is refined near the solid body or in zones of extreme flow variations. A recently proposed class of LBM models known as crystallographic LBM show an important connection between crystallography, optimal packing problem in the efficient discretization of PDE [101].

Based on this connection, it was argued that the optimal spatial discretization is provided by a body-centered cubic (bcc) arrangement of grid points and not by a simple cubic arrangement

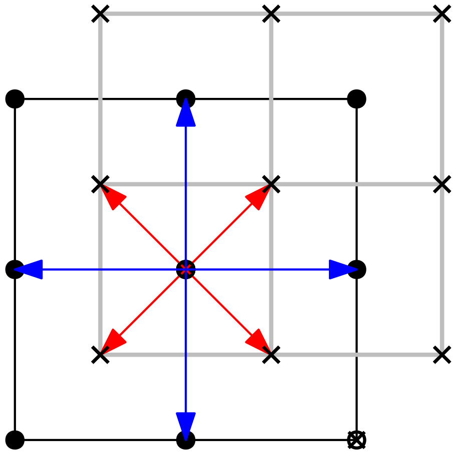

Fig. 3.1 Building block of a crystallographic lattice in two dimensions, simple cubic links (blue) and body-centered links (red) are depicted here.

of grid points as used by conventional structured grid-based methods [18, 100, 101]. This lattice comprises of two simple cubic lattices displaced by a distance of $0.5\Delta x$ in each direction. Figure 3.1 depicts the building blocks and the links of a bcc lattice in two dimensions for illustration purpose. Another well-known fact in the computer graphics literature is that the volume representation (or rendering) is better on the bcc lattice [5]. As the bcc grid has more points at the boundaries, it was also found to represent the boundaries well. To illustrate the difference between sc and bcc lattices, we show a depiction of a sphere and an ellipsoid on both sc and bcc lattices in Fig. 3.2.

Additionally, this class of bcc lattices removes an important artefact of sc lattices with velocity component unity (D3Q15, D3Q27) of imposing an artificial closure on the third-order moments where

$$\left\langle f, c_\alpha^3 \right\rangle = c^2 \left\langle f, c_\alpha \right\rangle, \tag{3.29}$$

here $\alpha = x, y, z$ and summation convention is not assumed. This effect plays an important role in regimes where the Knudsen boundary layer is important [8].

Like the traditional sc grids, the bcc grid also preserves the ease of streaming along the links while increasing the local accuracy.

A D3Q41 model with five different energy shells on a body-centred cubic grid, here onwards called the RD3Q41 grid, is proposed. Figure 3.3 shows the building blocks of the RD3Q41 model. The weights are derived by imposing the constraints from Eq.(3.26). It has two sc shells, one face-centered cubic (fcc) shell and two bcc energy shells. The energy shells and corresponding velocity sets with weights for this model are given in the Table 3.1.

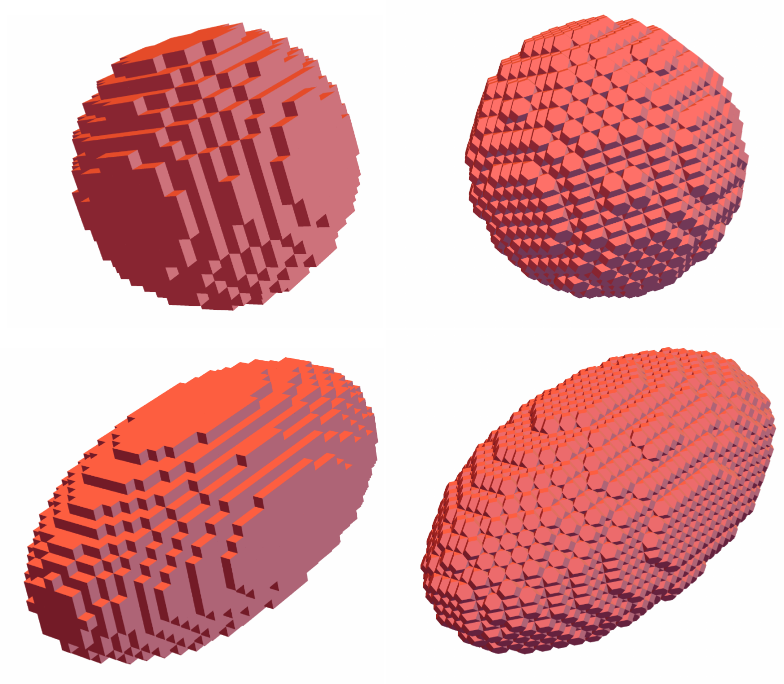

Fig. 3.2 A representation of sphere and an ellipsoid on sc(top) and bcc(bottom) lattices.

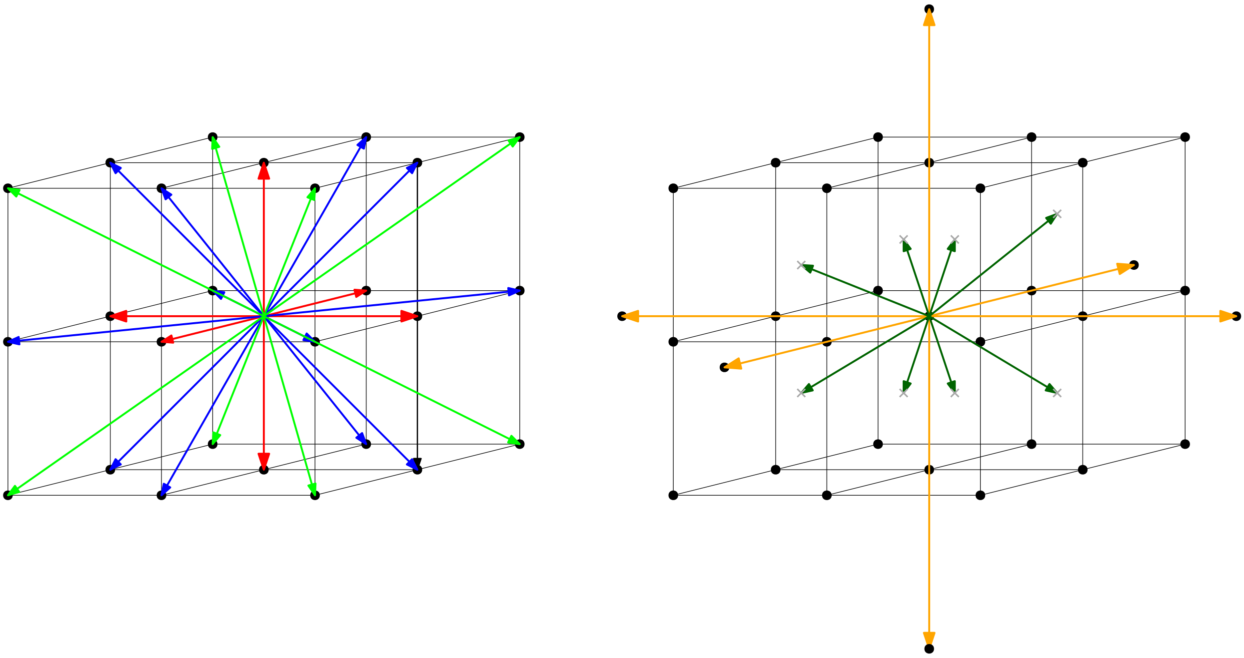

Fig. 3.3 Energy shells of the RD3Q41 model - sc-1(red), fcc-1(blue), bcc-1(light green) shown on a regular lattice and sc-2(orange), bcc-$\frac{1}{2}$(dark green).

Table 3.1 Energy shells and their corresponding velocities with weights for RD3Q41.

Shells	Discrete Velocities(c_i)	Weight(w_i)
sc-1	$(\pm1,0,0),(0,\pm1,0),(0,0,\pm1)$	0.04743040745116578
sc-2	$(\pm2,0,0),(0,\pm2,0),(0,0,\pm2)$	0.00165687664501576
fcc-1	$(\pm1,\pm1,0),(\pm1,0,\pm1),(0,\pm1,\pm1)$	0.00651175327832464
bcc -1	$(\pm1,\pm1,\pm1)$	0.00454087801154440
bcc -$\frac{1}{2}$	$(\pm0.5,\pm0.5,\pm0.5)$	0.04917980624482672

Using a crystallographic lattice structure requires $2N^3$ points to have a comparable resolution with $(2N)^3$ number of grid points using a standard lattice [101]. With this understanding, the memory requirement for the RD3Q41 is approximately $(2\times41)/(8\times27)\approx0.4$ times lower than the standard D3Q27 lattice. However, if we take the same number of points on both grids, the memory requirement for the standard D3Q27 lattice is $27/(2\times41)\approx0.33$ times lower than the proposed RD3Q41 lattice.

3.4 Discrete entropic equilibrium

The entropic formulation of the LBM restores the thermodynamic consistency embedded in the Boltzmann description. In this method, one starts with a discrete H function typically in the Boltzmann form

$$H=\sum_{i=1}^{N_d} f_i\left(\log\frac{f_i}{w_i}-1\right), \tag{3.30}$$

and construct equilibrium as its minimizer under the constraints of local conservation laws [11, 12, 26, 39, 68, 69, 128, 136]. Typically, the equilibrium is constructed in an isothermal setting which lacks energy conservation. In higher-order LBM energy conservation is included in deriving the thermal entropic equilibrium distribution.

In this section, we briefly derive the energy conserving equilibrium for the case of small temperature variation around reference temperature θ_0 using the entropic LBM. It should be reminded that in the case of entropic lattice Boltzmann model, for every discrete velocity model, one finds the Lagrange multiplier with a high degree of accuracy to preserve the positive form of equilibrium [43]. This is typically done numerically. To analyze the hydrodynamic limit of LBM, we derive the series form of the equilibrium. This allows us to calculate the closed-form expression for the moments. These expressions for the moments are relevant for analyzing the errors in the hydrodynamic limit.

Following Refs. [11, 18], we consider energy conserving equilibrium and include energy in the set of constraints to obtain the equilibrium distribution which minimizes entropy (Eq.(3.30)) as

$$f_i^{\mathrm{eq}} = w_i \rho \exp(-\alpha - \beta_\kappa c_{i\kappa} - \gamma c_i^2). \tag{3.31}$$

where $\alpha, \beta_\kappa, \gamma$ are the Lagrange multipliers associated with mass, momentum and energy respectively [11, 12]. The explicit expression can be obtained by inverting the following relations

$$\left\langle f_i^{\mathrm{eq}}, \{1, c_{i\alpha}, c^2\}\right\rangle = \{\rho, \rho u_\alpha, \rho u^2 + 3\rho\theta\}. \tag{3.32}$$

However, other than a few special cases such as the $D1Q3$ model and its higher dimension extensions $D2Q9$ and $D3Q27$, the explicit solutions are not known [11, 12]. The system of equations in Eq.(3.32) are not explicitly invertible, therefore we choose a reference state with mean velocity $u_\alpha = 0$ where $\beta_\kappa = 0$. Thus, the system of equations simplifies as

$$\begin{aligned} &\exp(-\alpha^0) \sum_{i=1}^{N_d} w_i \exp(-\gamma^0 c_i^2)\{1, c_i^2\} \\ &= \{1, 3\theta\} \equiv \{1, 3\theta_0(1+\eta)\}, \end{aligned} \tag{3.33}$$

where, α^0 and γ^0 are Lagrange multipliers corresponding to the state $\mathbf{u} = \mathbf{0}$. However, even for $\mathbf{u} = \mathbf{0}$, explicit solutions for other Lagrange multipliers are not known for most of the models[11]. Therefore, at $u_\alpha = 0$ itself we chose another reference state $\theta = \theta_0$ for which it is trivial to check that the solution is $\alpha^0(\theta = \theta_0) = 0$ and $\gamma^0(\theta = \theta_0) = 0$.

Following the procedure of Ref. [18], a perturbative series around this reference state can be built by expanding the Lagrange multipliers around $\alpha^{(0)}$ and $\gamma^{(0)}$ in powers of the smallness parameter $\eta = \theta/\theta_0 - 1$ (denoting smallness of the temperature deviation). The explicit solution is evaluated up to $\mathscr{O}(\eta^3)$ as

$$\begin{aligned} \tilde{f}_i = w_i \rho \Bigg[1 &+ \frac{\eta}{2}\left(\frac{c_i^2}{\theta_0} - 3\right) + \frac{\eta^2}{8}\left(\frac{c_i^4}{\theta_0^2} - 10\frac{c_i^2}{\theta_0} + 15\right) \\ &+ \frac{\eta^3}{48}\left(\frac{c_i^6}{\theta_0^3} - 21\frac{c_i^4}{\theta_0^2} + 105\frac{c_i^2}{\theta_0} - 105\right)\Bigg]. \end{aligned}$$

The equilibrium distribution at non-zero velocity is derived by expanding the Lagrange multipliers in ε (representing the smallness of the velocity scale) and the expression for discrete equilibrium accurate up to $\mathscr{O}(\varepsilon^3)$ is obtained to be

$$\begin{aligned} f_i^{\mathrm{eq}} =& \tilde{f}_i \left[1+\frac{u_\alpha c_{i\alpha}}{\theta}-\frac{u^2}{2\theta}(1-A_1)+\frac{1}{2}\left(\frac{u_\alpha c_{i\alpha}}{\theta}\right)^2+\frac{1}{6}\left(\frac{u_\alpha c_{i\alpha}}{\theta}\right)^3\right. \\ & \left. -\frac{u^2 c_i^2}{6\theta^2}A_1+\frac{u^2 u_\alpha c_{i\alpha}}{6\theta^2}A_2-\frac{u^2 c_i^2 u_\alpha c_{i\alpha}}{6\theta^3}A_1\right], \end{aligned} \tag{3.34}$$

where M_2 and M_2', the error terms with respect to zero velocity equilibrium moments, and A_1 and A_2 are

$$\begin{aligned} M_2 &= -0.807953\Delta^3\theta\left(\frac{\theta_0}{\theta}\right)^2, \\ M_2' &= -\left[0.520459\Delta^2\theta+1.41017\Delta^3\theta\right]\left(\frac{\theta_0}{\theta}\right)^2, \\ A_1 &= \frac{5/2M_2}{1+5/2M_2}, \\ A_2 &= 5A_1\left(1-M_2\right)-\left(3+M_2'-5M_2\right), \end{aligned} \tag{3.35}$$

with $\Delta\theta = \theta - \theta_0$. The equilibrium moments for this model are,

$$\begin{aligned} P_{\alpha\beta}^{\mathrm{eq}} &= \rho\theta\delta_{\alpha\beta}+\rho u_\alpha u_\beta\left(1-M_2'\right)+\frac{u^2}{2}\delta_{\alpha\beta}\left[1+4M_2'-5M_2-\frac{\left(1+\frac{25}{6}M_2-\frac{25}{6}M_2^2\right)}{1+\frac{5}{2}M_2}\right], \\ q_\alpha^{\mathrm{eq}} &= 5\theta u_\alpha\left(1-M_2\right)+\frac{1}{6}u^2u_\alpha\left[5A_2\left(1-M_2\right)-7A_1\left(1-M_3\right)+7\left(3+2M_3'-5M_3\right)\right], \end{aligned} \tag{3.36}$$

where

$$\begin{aligned} M_3 &= -\left[0.69253\Delta^2\theta-2.49925\Delta^2\theta\right]\left(\frac{\theta_0}{\theta}\right)^3, \\ M_3' &= -3.18168\left(\frac{\theta_0}{\theta}\right)^3\times\left(0.0934743\Delta\theta+0.636954\Delta^2\theta+\Delta^3\theta\right). \end{aligned} \tag{3.37}$$

The $P_{\alpha\beta}$ and q_α moments of the equilibrium distribution have errors of the order $\mathscr{O}(u^2\eta^3)$ and $\mathscr{O}(u^3\eta^3)$ respectively and match with the moments of the Maxwell-Boltzmann distribution up to high accuracy. Thus, model accurately recovers linearized hydrodynamics.

In the subsequent sections, we validate the accuracy and robustness of the proposed RD3Q41 model by simulating various canonical flows related to acoustics, compressible, turbulent, multiphase and thermal flows.

3.5 Acoustics

In the previous sections, the RD3Q41 model has been shown to recover the full Navier-Stokes-Fourier equations as its macroscopic limit. In this section, we select a few well-studied benchmarking problems related to the propagation of an acoustic pulse. The aim is to demonstrate that the model is suitable for simulating acoustic phenomena for subsonic flows.

As a first example, we present an isothermal simulation of propagation of a 2D acoustic pulse. The third direction has two lattice points, and periodic boundary conditions are imposed. An axisymmetric density pulse is initialized at the center of a uniform fluid of size $[-1,1]$ in both x and y directions as

$$\rho(x,y,t=0) = \rho_0[1.0+\rho'(x,y,t=0)], \tag{3.38}$$

where

$$\begin{aligned} \rho'(x,y,t=0) = \varepsilon e^{-\alpha r^2}, \quad \varepsilon = 0.001, \quad \alpha = \frac{\ln(2)}{b^2}, \\ b = 0.1, \qquad r = \sqrt{x^2+y^2}. \end{aligned} \tag{3.39}$$

A small value of ε is chosen to keep the amplitude of the acoustic perturbation small. For low amplitudes of density fluctuations and low viscosity, the exact solution of the density fluctuation is given by the analytical solution of the linearized Euler equations [131, 54]. The explicit expression for the density fluctuation is

$$\rho'(x,y,t) = \rho_0 \times \frac{\varepsilon}{2\alpha}\int_0^\infty \exp\left(\frac{-\xi^2}{4\alpha}\right)\cos(c_s\xi t)J_0(\xi r)\xi \, d\xi, \tag{3.40}$$

where J_0 is the Bessel function of the first kind of zero-order [1].

An excellent match is observed upon comparing density fluctuations along the centerline from isothermal simulation using our model and from the analytical solution at various time steps (t^*) as shown in Fig. 3.4. This confirms that the linearized acoustics are captured accurately in an isothermal setting.

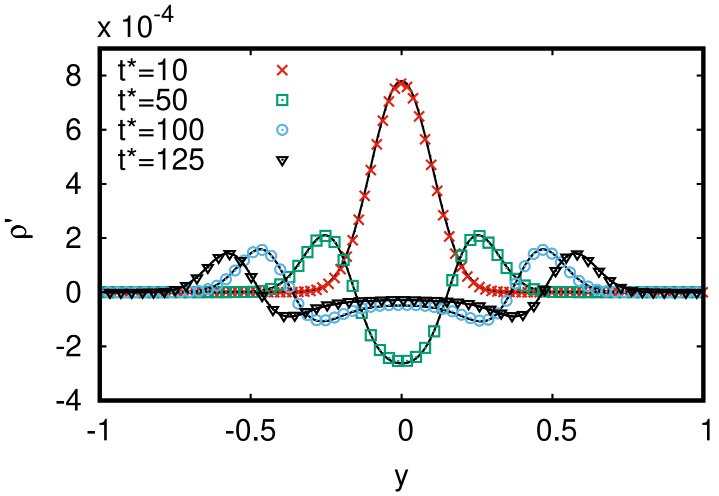

Fig. 3.4 Density fluctuations along the centerline in isothermal case (solid line) at different time steps compared with analytical solution (points).

To show that the ratio of sound speeds in a thermal to isothermal model is $\sqrt{\gamma}$, we perform thermal simulation of the same setup and compare the pressure fluctuations at times (t^*) with that obtained from an isothermal simulation at times $t = \sqrt{\gamma} \times t^*$. The specific heat ratio γ for the current model is $5/3$. The pressure fluctuation p' is defined as the deviation of pressure from rest condition as $p' = p - \rho_0\theta_0$. It can be seen from Fig. 3.5 that the profiles match very well confirming that the ratio of speed of sound is $\sqrt{\gamma}$ and energy conserving LB model indeed recovers the correct isentropic sound speed.

3.5.1 3D acoustic spherical pulse source

We demonstrate the utility of the present model in 3D via a simulation of a spherical pulse source. An acoustic pulse is initialized in the center of the domain of size $[-1,1]$ in x, y and z directions as

$$\rho(x,y,z,t=0) = \rho_0[1.0 + \rho'(x,y,z,t=0)], \tag{3.41}$$

where

$$\begin{aligned} \rho'(x,y,z,t=0) = \varepsilon e^{-\alpha r^2}, \quad \varepsilon = 0.001, \quad \alpha = \frac{\ln(2)}{b^2}, \\ b = 0.03, \qquad r = \sqrt{x^2+y^2+z^2}. \end{aligned} \tag{3.42}$$

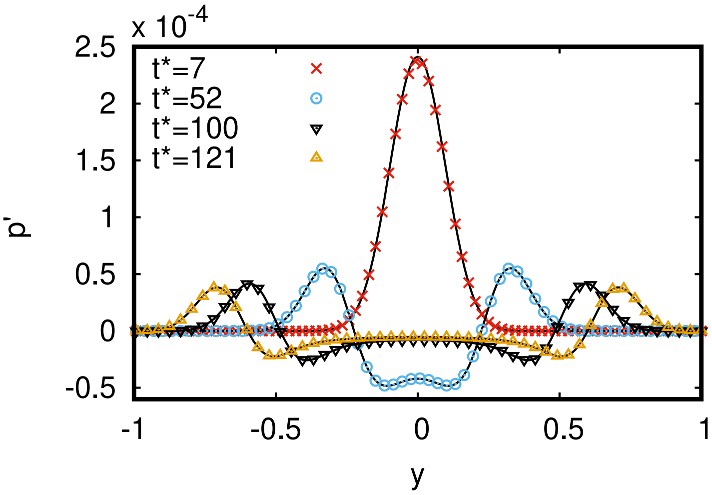

Fig. 3.5 Comparison of pressure fluctuations along the centerline at time t^* from a thermal simulation (solid line) and isothermal simulation (points) at time $\sqrt{\gamma} \times t^*$

The exact solution for the density fluctuation is given as [25]

$$\rho'(x,y,t) = \frac{\varepsilon}{2\alpha\sqrt{\pi\alpha}} \int_0^\infty \exp\left(\frac{-\xi^2}{4\alpha}\right) \frac{\sin(\xi r)}{\xi r} \xi^2 d\xi. \tag{3.43}$$

The density fluctuations from the LB simulation and the exact solution are plotted at a few time steps (t^*) along the y-axis at $(x,z) = (0.5, 0.5)$ in Fig. 3.6 and they show an excellent agreement.

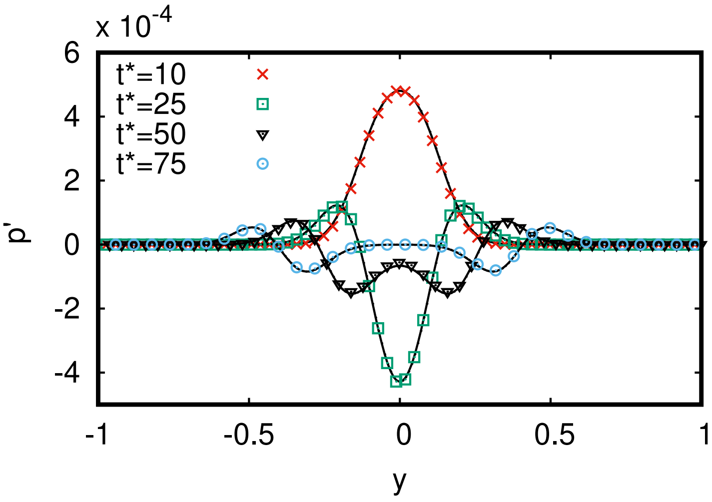

Fig. 3.6 Density fluctuations due to a 3D spherical pulse source along the y-axis at $(x,z) = (0.5, 0.5)$ from LB simulation (line) and exact solution (points).

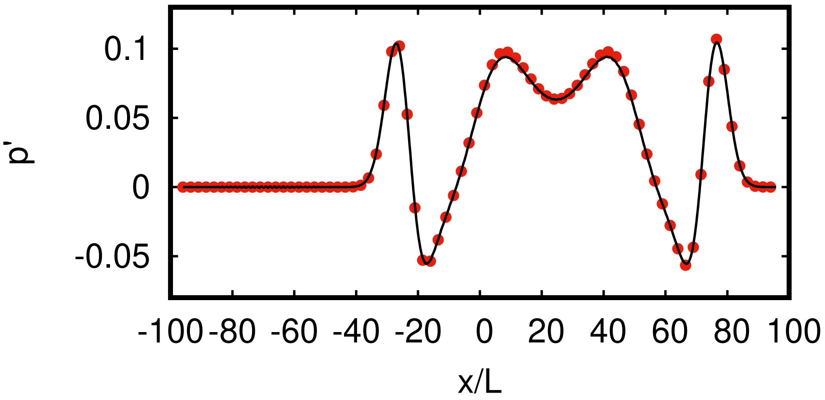

Fig. 3.7 Pressure fluctuations normalised with A at $y = 24L$ after 50 convection times (LB-line, Analytical-points).

3.5.2 Acoustic pulse reflecting off a planar wall

Next, we demonstrate the capability of the model to simulate the interaction of acoustic waves with simple boundaries. The interaction of an acoustic wave in a mean flow of Mach number $\text{Ma} = 0.5$ with an inviscid planar wall is simulated. A domain of length $[-100L, 100L]$ and $[0, 200L]$ is chosen along the x and y axes. An acoustic pulse is initiated at $t = 0$ as

$$p' = A \exp\left(-\ln(2)\left[\frac{x^2 + (y-25)^2}{25}\right]\right), \tag{3.44}$$

with $u = 0.5c_s$, $v = 0$ and $A = 10^{-4}$. This setup is identified as an effective test case to check the wall boundary conditions and an analytical solution for the pressure fluctuations is given in Ref. [60] as

$$p' = \frac{A}{2\alpha}\int_0^\infty \exp\left(\frac{-\xi^2}{4\alpha}\right)\cos(\xi t)\left[J_0(\xi\eta) + J_0(\xi\zeta)\right]\xi d\xi, \tag{3.45}$$

where $\alpha = \ln(2)/25$, $\eta = \sqrt{(x - \text{Ma}\times t)^2 + (y-25)^2}$, and $\zeta = \sqrt{(x + \text{Ma}\times t)^2 + (y-25)^2}$. We choose four lattice points per L for this simulation. The convection time t_c here is defined as L/c_s. Contours of pressure fluctuations normalized with A at the initial time and after 50 convection times from our simulation are shown in Fig. 3.8. Pressure fluctuations normalized with A obtained from the current simulation and the analytical solution after a time of $50t_c$ at $y = 24L$ shows an excellent match in Fig. 3.7.

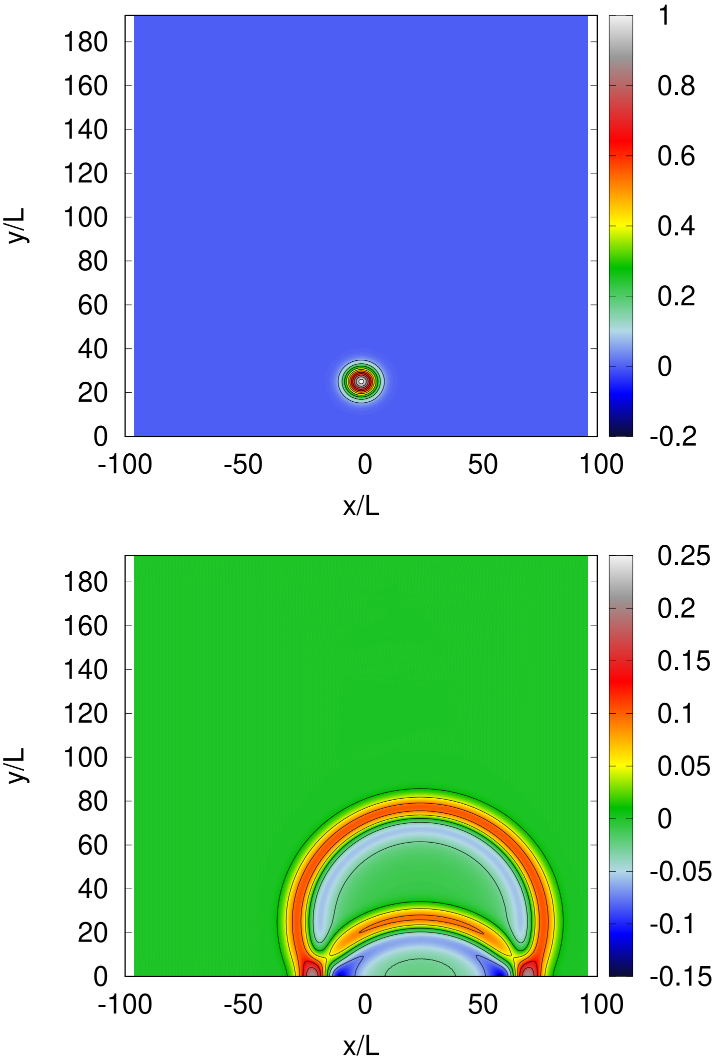

Fig. 3.8 Contours of pressure fluctuations normalised with A at $t = 0$ (up) and $t = 50$ convection times (bottom).

3.5.3 Acoustic scattering off a rigid cylinder

The acoustic scattering off a rigid cylinder is one of the benchmark problems identified as a simplified model to find the sound scattered by aircraft fuselage produced by the propeller [130]. In that work, the fuselage was approximated as a circular cylinder, and the source of sound was reduced to a point source. The presence of a curved boundary also makes this a natural extension to the previous test case for validating the wall boundary conditions.

A cylinder of diameter D_0 is placed at the center of a domain of length $[-15D_0, 15D_0]$ in both x and y directions. At a distance of $4D_0$ from the center of the cylinder along the x-axis a Gaussian acoustic pulse is initialized at $t = 0$ as

$$p' = A\exp\left(-\ln(2)\left[\frac{(x-4)^2+y^2}{0.2^2}\right]\right), \tag{3.46}$$

where $A = 10^{-4}$. The analytical solution for this test case is given as [129]

$$p' = Re\left\{\int_0^\infty (A_i(x,y,\omega)+A_r(x,y,\omega))\,\omega e^{-i\omega t} d\omega\right\}, \tag{3.47}$$

where A_i and A_r stand for the amplitudes of incident and reflected waves given as

$$A_i(x,y,\omega) = \frac{1}{2b}e^{-\omega^2/(4b)}J_0(\omega r_s), \tag{3.48}$$

with $r_s = \sqrt{(x-4D_0)^2+y^2}$, J_0 is Bessel function of zero order, and

$$A_r(x,y,\omega) = \sum_{k=0}^{\infty} C_k(\omega)H_k^{(1)}(r\omega)\cos(k\omega), \tag{3.49}$$

with

$$C_k(\omega) = \frac{1}{2\pi}\exp\{-\omega^2/(4b)\}\,\frac{\varepsilon_k}{\left[H_k^{(1)}\right]'}\int_0^\pi J_1(\omega r_{s0})\frac{r_0-4\cos(\theta)}{r_{s0}}\cos(k\theta)d\theta,$$

where $\varepsilon_0 = 1$, $\varepsilon_k = 2$ for $k \neq 0$, $r_0 = 1/2$ and $r_{s0} = \sqrt{0.25+x_s^2D_0^2-x_sD_0\cos(\theta)}$ while $H_k^{(1)}$ is the Hankel function of first order [1].

Pressure fluctuation profiles normalised with p_0A from times $t = 6$ to 10 convection times is plotted in Fig. 3.9 at three points $A(r = 5D_0, \theta = 90°)$, $B(r = 5D_0, \theta = 135°)$ and $C(r = 5D_0, \theta = 180°)$. The convection time scale is defined based on the cylinder's diameter and

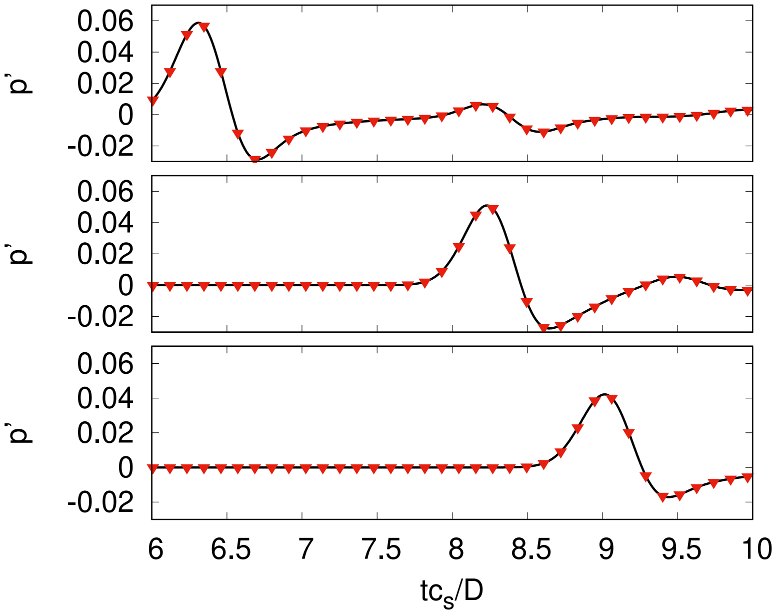

Fig. 3.9 Time evolution of pressure fluctuations normalised by p_0A at points $r = 5D_0$ and $\theta = 90^\circ, 135^\circ$ and 180° from top to bottom (LBM-solid line, Analytical-points).

sound speed as D_0/c_s. The points and time intervals are chosen such that only the acoustic wave reflected off the cylinder passes through these points. The pressure fluctuation profiles show a good agreement with the exact solution demonstrating the capability of the current model for solving computational aeroacoustics problems with non-trivial boundary shapes. Isocontours of pressure fluctuations normalized by p_0A are shown in Fig. 3.10 at times $t = 1.6, 4.0, 6.0$ and 10.0 convection times. The contours also show the direct wave D and the acoustic waves reflecting off the surface of the cylinder R.

In the following table we summarize the grid sizes, boundary conditions and time taken to run these simulations on a 11th Gen Intel® Core™ i7-11370H processor.

3.6 Energy conservation

Next, we wish to demonstrate that energy conservation is modelled correctly. In this section, we demonstrate the efficacy of the RD3Q41 model for simulating thermal flows by studying two test cases: a Couette flow with a temperature gradient (where the viscous heat dissipation becomes crucial) and heat conduction in a 2D cavity. These are setups where one expects the effects of

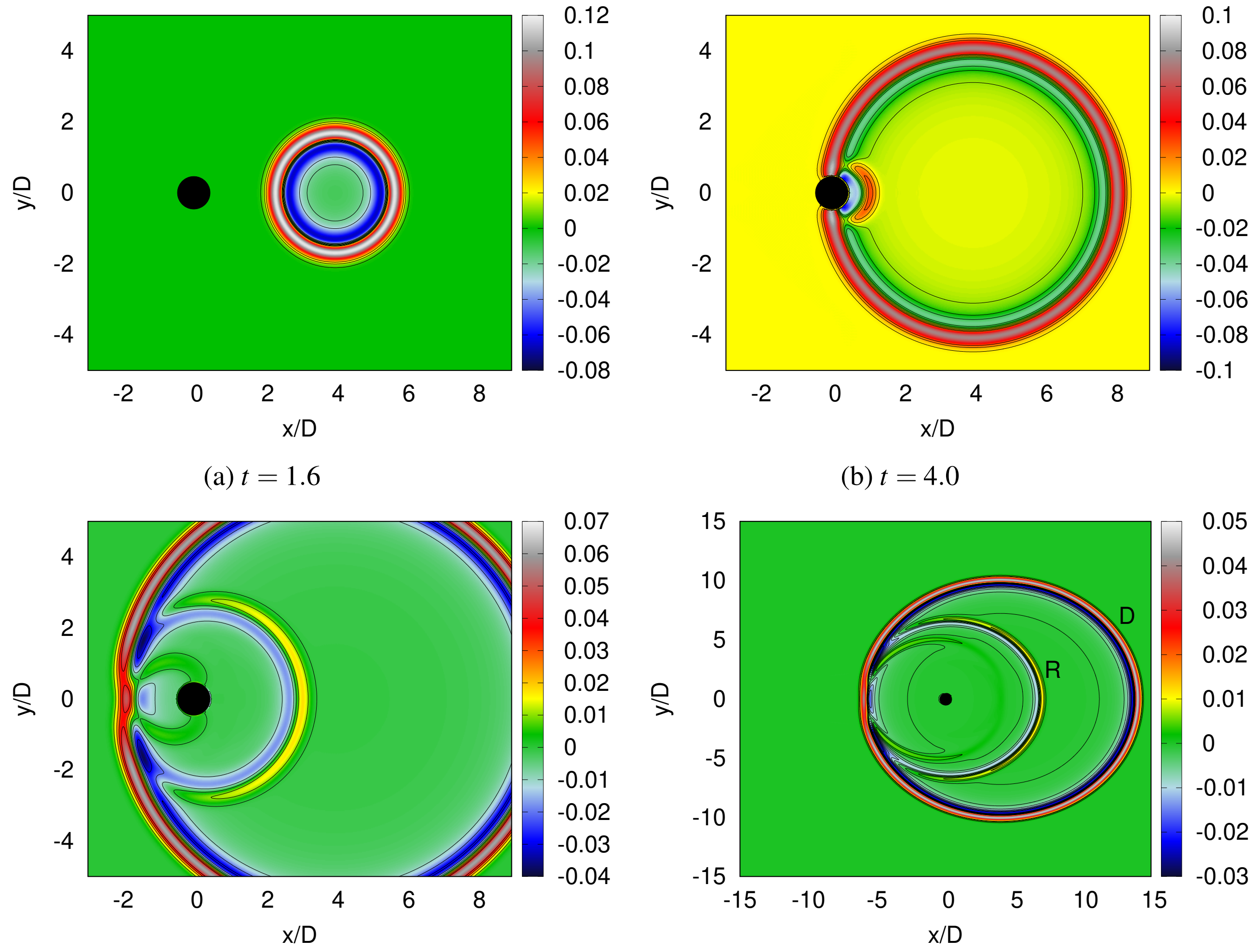

(a) $t = 1.6$ (b) $t = 4.0$

(c) $t = 6.0$ (d) $t = 10.0$

Fig. 3.10 Isocontours of pressure fluctuations normalised by p_0A at different times where D is the direct wave and R is the wave reflected off the surface of the cylinder.

Table 3.2 Grid and boundary condition details for various test cases. Simulation times reported are for single processor runs on a 11th Gen Intel® Core™ i7-11370H processor.

Test case	**Grid size**	**Boundary conditions**	**Simulation time in seconds (no. of iterations)**
2D acoustic pulse	$256 \times 256 \times 4$	(x,y,z) - Periodic BCs	$\approx$ 15 (162 iters)
3D acoustic pulse	$256 \times 256 \times 256$	(x,y,z) - Periodic BCs	$\approx$ 705 (75 iters)
Scattering off planar wall	$200L \times 200L \times 4$ L = 4	x - Outlet BCs y (top) - Outlet BC y (bottom) - Free slip wall z - Periodic BCs	$\approx$ 370(285 iters)
Scattering off rigid cylinder	$30D_0 \times 30D_0 \times 4$ $D_0 = 50$	(x,y,z) - Periodic BCs Cylinder - Bounceback BC	$\approx$ 3350(720 iters)

thermal conductivity to have a significant role. Hence, these test cases help in demonstrating the domain of validity of the proposed model.

3.6.1 Viscous heat dissipation

We consider the steady state of flow induced by a wall at $y = H$ moving with a constant horizontal velocity U_0 and maintained at a constant elevated temperature T_1. The lower wall at $y = 0$ is kept stationary at a constant temperature T_0 ($T_1 > T_0$).

This setup is well-suited to validate the effect of viscous heat dissipation. Each layer of fluid drags the layer below it due to friction, which results in the mechanical energy being converted to thermal heating, and therefore, the heat produced affects the temperature profile in bulk. The analytical solution for the temperature profile for this setup is [24]

$$\frac{T - T_0}{\Delta T} = \frac{y}{H} + \frac{\mathrm{Ec}}{2}\frac{y}{H}\left(1 - \frac{y}{H}\right), \tag{3.50}$$

where $\Delta T = T_1 - T_0$ is the temperature difference between the two walls and $\mathrm{Ec} = U_0^2/(c_p \Delta T)$ is the Eckert number that represents the ratio of viscous dissipation to heat conduction with $c_p = 5/2$ as the specific heat at constant pressure.

Simulations were performed for $\mathrm{Ec} = 0.5, 2.0, 5.0$ with $U_0 = 0.02$ and $\Delta\theta$ calculated according to respective Eckert numbers. The walls were maintained at temperatures $\theta_0 + 0.5\Delta\theta$ and $\theta_0 - 0.5\Delta\theta$. Kinetic boundary conditions as described in Ref. [9] have been applied at the walls, and periodic boundary conditions are used in the other two directions. Figure 3.11 compares the temperature profiles obtained analytically and via simulations and they are found to agree well.

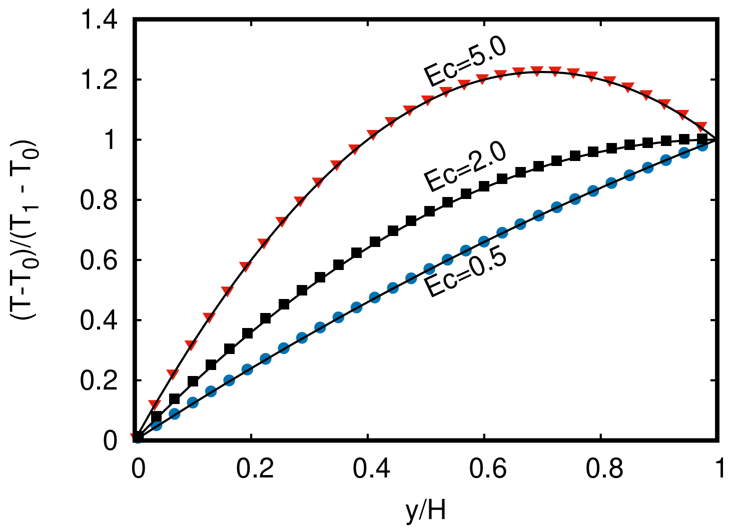

Fig. 3.11 Mean planar temperature profiles obtained from *RD*3*Q*41 at steady state (symbols) compared to the analytical solution (lines).

3.6.2 2D cavity heated at the top

In this setup, the fluid is confined in a rectangular cavity bounded with stationary walls on all four sides. The height of the cavity is W, and its length is L. The top wall is maintained at temperature (T_1), and the other three walls are maintained at temperature T_0 ($T_1 > T_0$). The temperature profile for this setup at the steady state is given by

$$\frac{T-T_0}{T_1-T_0} = \frac{2}{\pi}\sum_{n=1}^{\infty}\frac{(-1)^{n+1}+1}{n}\sin(n\pi x)\frac{\sinh(n\pi y)}{\sinh(n\pi H/L)}. \tag{3.51}$$

Kinetic boundary conditions as described in Ref. [9] have been applied at the top and bottom walls and periodic boundary conditions are applied in z-direction. The temperature profiles along the constant $x = 0.1, 0.2, 0.5$ and constant $y = 0.25, 0.5, 0.75$ are shown in Fig. 3.13 and can be seen to match well with the analytical solution. These two test cases prove that the thermal transport phenomenon is modeled correctly in the RD3Q41 model.

3.7 Thermoacoustics

In the previous sections, we showed that the current model accurately predicts acoustic and thermal phenomena individually. We now demonstrate the capability of the RD3Q41 model in simulating flows involving both thermal and acoustic phenomena.

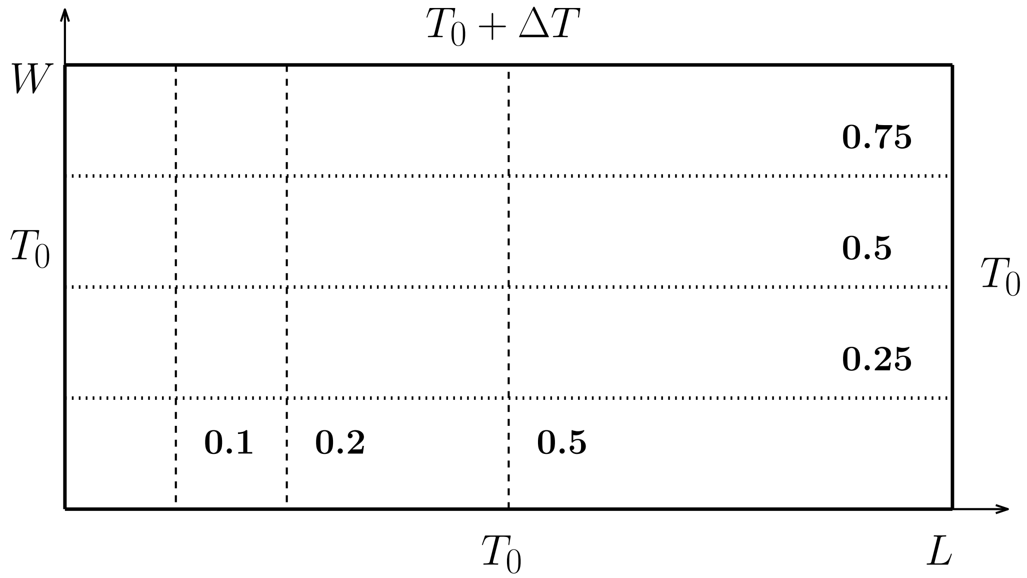

Fig. 3.12 Setup for the 2D cavity heated at the top.

A simple example is when a compressible fluid confined between two walls is heated rapidly on one end, it sets up a convective current [67, 84, 104]. The heated wall creates a pressure wave which reflects back and forth in the medium until it gets dissipated by viscosity. These pressure waves are called thermoacoustic waves because of the acoustic nature of the origin of these waves. It is understood that this thermally induced motion is known to enhance the heat transfer in the medium by addition of convective mode to the conductive mode of heat transfer [84]. The convective mode slowly dissipates due to the dissipation of the pressure wave, and conduction becomes the only mode of heat transfer [124]. The many time and length scales present in the system along with the compressible nature of the fluid makes numerical modeling of thermoacoustic convection a challenging problem.

The setup consists of a fluid column of length L enclosed between two walls. It is initially at a uniform temperature of T_0, as shown in Fig. 3.14. At times $t > 0$ the bottom wall is maintained at temperature T_0 while the top wall is rapidly heated to a temperature $T_0 + \Delta T$. Kinetic boundary conditions, as described in Ref. [9], have been applied at the walls. The compression and rarefaction of the thermoacoustic waves due to rapid heating create a fluctuating velocity in the domain which results in a significant increase in the rate of heat transfer relative to pure conduction.

To benchmark our code, Navier-Stokes-Fourier equations are solved as described in Ref. [84] to compare the evolution of the nondimensional temperature, density, and pressure obtained from the RD3Q41 model at a few intermediate times scaled by diffusion time. Diffusion time is

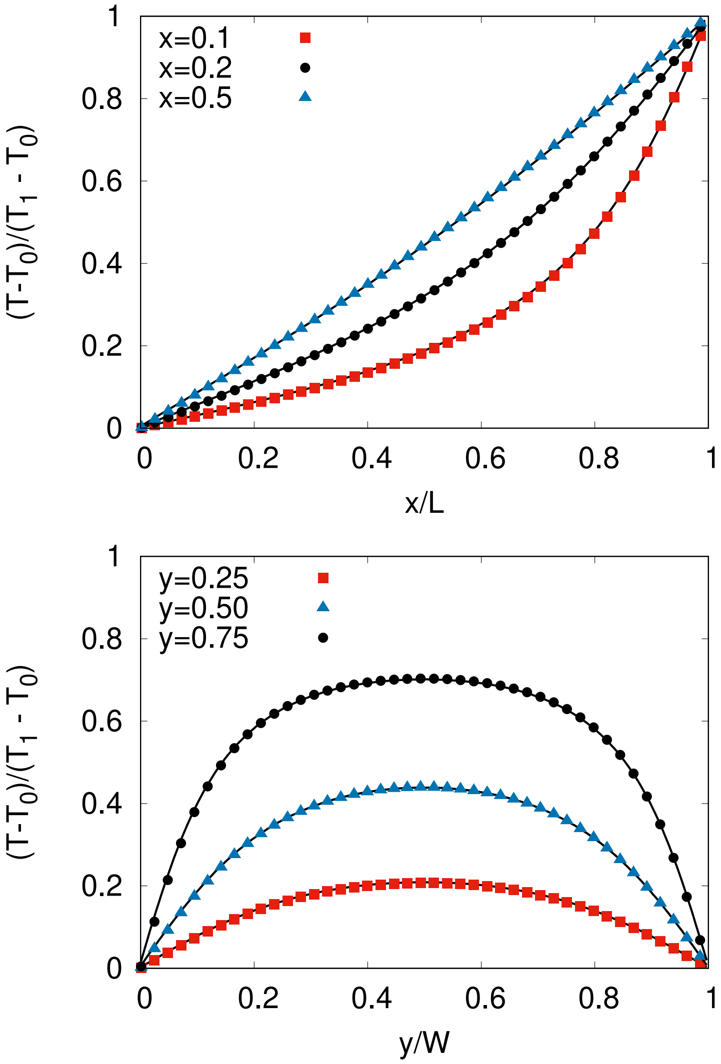

Fig. 3.13 Steady state temperature profiles at sections along X-axis (left) and Y-axis (right). The symbols are the solution form the RD3Q41 model while the lines represent the analytical solution.

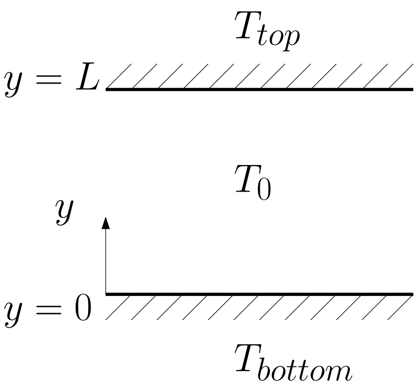

Fig. 3.14 A schematic of the setup for thermoacoustic convection

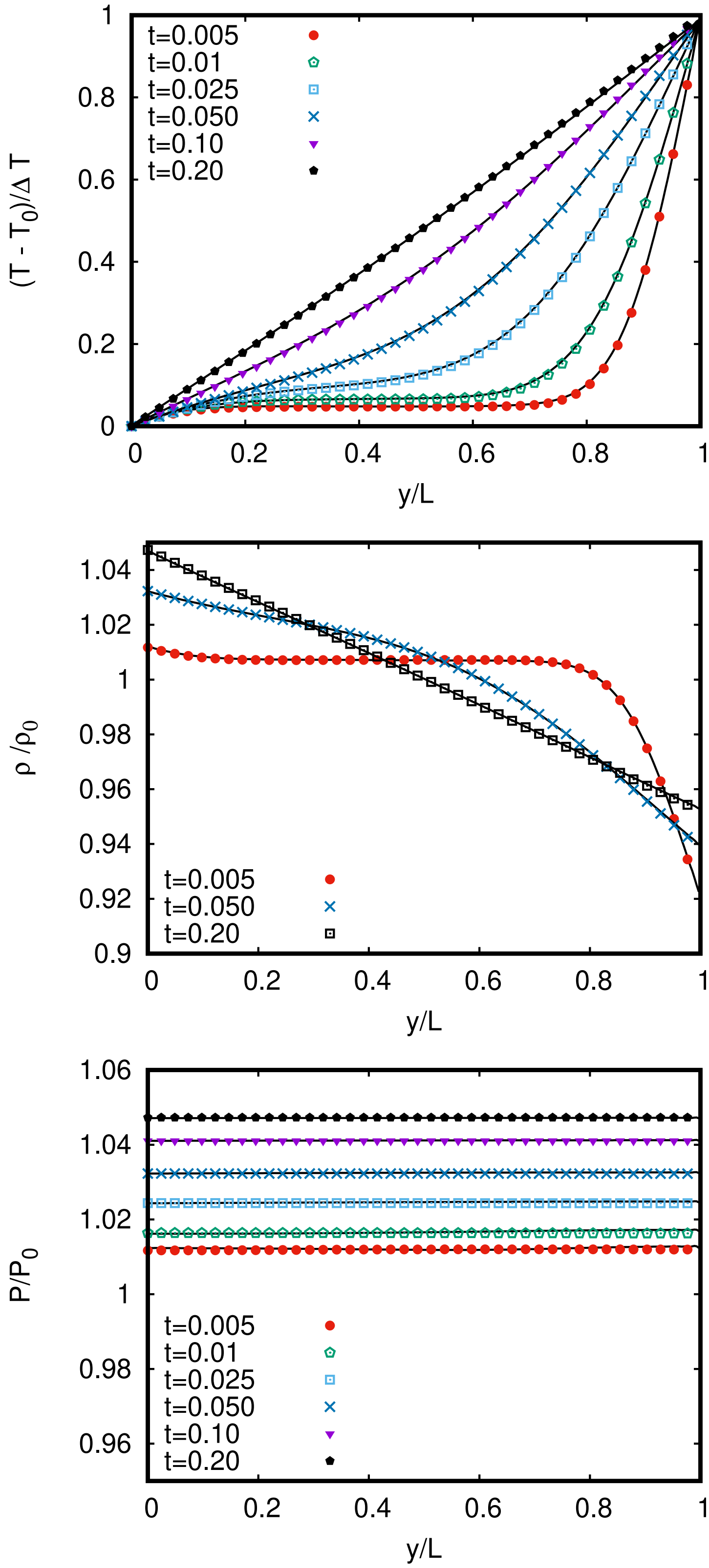

Fig. 3.15 Nondimensional temperature, density and pressure at a few intermediate times scaled by diffusion time.(LBM- points, solution of NSF equations - lines).

defined as L^2/ν, where ν is kinematic viscosity of the fluid. Results from both the methods are in good agreement, as shown in Fig. 3.15.

3.8 Sound propagation in a nonideal gas

In this section, we validate the proposed model for sound propagation in an isothermal nonideal gas. For a gas following an ideal equation of state $p = \rho\theta_0$ the sound speed is fixed at $\sqrt{\theta_0}$ where θ_0 is a reference temperature. However, in real gases, the speed of sound becomes dependent on the phase density too as pressure is a non-trivial function of phase density. To confirm this, we introduce a density perturbation at constant temperature in a nonideal fluid with Peng-Robinson type equation of state given by

$$p = \rho\theta_0 \frac{1+\eta+\eta^2-\eta^3}{(1-\eta)^3} - \frac{a\rho^2}{1+2\rho b-\rho^2 b^2}, \tag{3.52}$$

where $a = 1.8514276622\theta_c/\rho_c$, $b = 0.353748714/\rho_c$ are van der Waals like critical parameters and $\eta = \rho b/4$. Here, θ_c and ρ_c are critical temperature and critical density, respectively.

We compute the speed of sound at various values of $\theta^* = \theta_0/\theta_c$ and their corresponding equilibrium phase densities (ρ_{ph}) by initializing a 1D density fluctuation of the form

$$\rho(x, t=0) = \rho_{\mathrm{ph}}\left(1.0 + \varepsilon\cos(\pi x)\right), \tag{3.53}$$

in domain of size $[-\pi, \pi]$ in x-direction. The domain has two lattice points in the y and z directions and periodic boundary conditions are applied in all three directions. The wave is expected to reach the same configuration as the initial condition after one wave period (t_p). We track the l2-norm of the density fluctuation computed using the present state and initial state, which is minimum when the waves are in-phase after completing one cycle. The domain size (L) and the time period at which l2-norm is minimum are used to compute the speed of sound ($c_s = L/t_p$). We observe a good agreement with the theoretical prediction of the sound speed in both the phases for a broad range of θ^* as shown in Fig. 3.16.

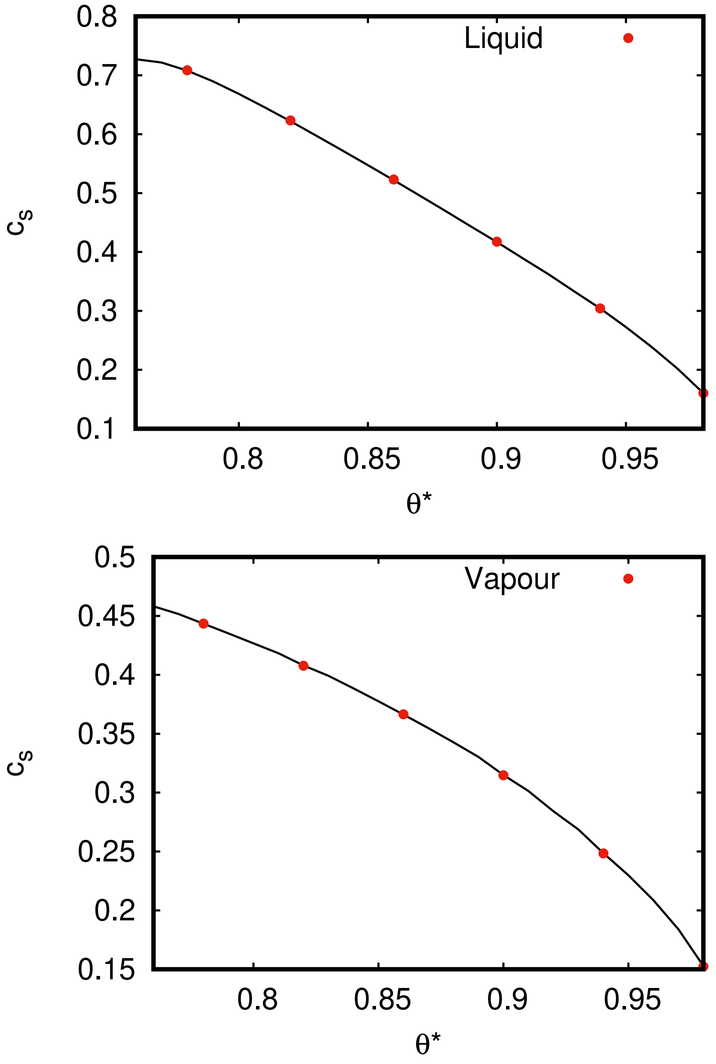

Fig. 3.16 Speed of sound in a nonideal gas for liquid and vapour phases – theoretical prediction (solid line) and simulation (points).

3.9 Turbulent Flows

Higher-order isothermal lattice Boltzmann methods are known to be stable and have been proposed as an alternative to direct numerical simulations (DNS) for fluid turbulence [42]. It is shown that energy conserving LB models are numerically stable than their non-energy conserving counterparts [122]. The proposed RD3Q41 model, which is an energy conserving higher-order LB model, takes advantage of these two features and is a viable alternative for DNS simulations of turbulent flows. In this section, we present simulations of turbulent flows for three cases - a fully periodic test case of decaying turbulence, flow in a rectangular channel and flow over a sphere.

3.9.1 Kida-Peltz flow

Kida-Peltz flow is a periodic flow with highly-symmetric initial conditions and is a good test case for the computational study of high Reynolds number (Re) flows [71]. The initial conditions for the flow are

$$\begin{aligned} u_x(x,y,z) &= U_0\ \sin x\ (\cos(3y)\ \cos z - \cos y\ \cos(3z)), \\ u_y(x,y,z) &= U_0\ \sin y\ (\cos(3z)\ \cos x - \cos z\ \cos(3x)), \\ u_z(x,y,z) &= U_0\ \sin z\ (\cos(3x)\ \cos y - \cos x\ \cos(3y)), \end{aligned} \tag{3.54}$$

with $x, y, z \in [0, 2\pi]$. The simulations were performed at a Reynolds number 5000 defined based on the domain length and velocity U_0. In this flow, enstrophy(Ω) increases very sharply in the initial time steps and reaches a maximum value and then decays with time. Mean enstrophy is calculated from the symmetric velocity gradient tensor[51]

$$S_{\alpha\beta} = \frac{2}{\rho\theta(2\tau + \Delta t)} \sum_i \left(f_i - f_i^{eq}\right) c_{i\alpha} c_{i\beta}, \tag{3.55}$$

where $\tau = \nu/c_s^2$.

We demonstrate the efficiency of the proposed RD3Q41 model by comparing the evolution of mean enstrophy of a Kida-Peltz flow setup with that of pseudo-spectral(PS) method in Fig. 3.17.

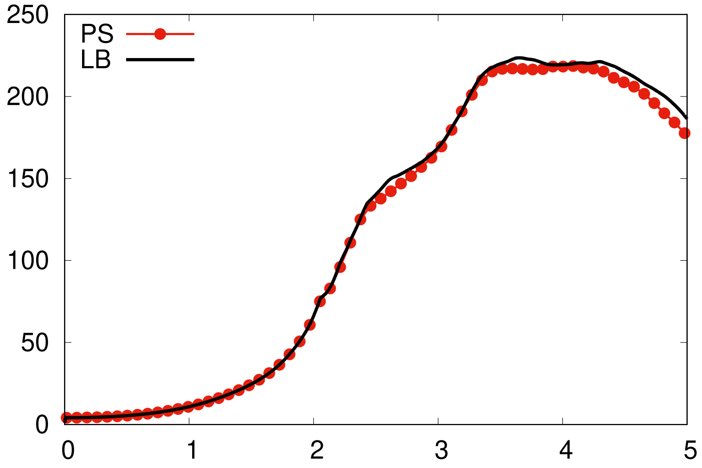

Fig. 3.17 Comparison of evolution of mean enstrophy with time (line–LBM, points–PS).

3.9.2 Turbulent channel flow

In this section, the proposed RD3Q41 model is benchmarked for the classic wall-bounded turbulent flow in a rectangular channel. We perform simulations at a friction Reynolds number $(Re_\tau) \approx 180$. The friction Reynolds number is defined based on the wall shear velocity (u_τ) and the channel half-width (δ). The simulations were performed a domain of size $12\delta \times 2\delta \times 6\delta$, and the channel half-width was chosen to be 96 grid points. This corresponds to a nondimensional grid spacing $y^+ = yu_\tau/\nu \approx 2$. This resolution is sufficient to resolve the Kolmogorov length scale [22]. The flow is driven by a body-force, and periodic boundary conditions are applied in streamwise and spanwise directions. Turbulence in the domain is triggered by adding a divergence-free noise to the initial conditions [28].

At sufficiently high Reynolds numbers in channel flows, the variation of the mean velocity in wall coordinates (u^+) is known to follow the law of the wall [105]. The mean velocity (u^+) scales linearly with wall coordinate y^+ in viscous layer and in the log-law region scales as $u^+ = (1/\kappa)ln(y^+) + B$ where $\kappa = 0.42$ and $B = 5.5$ are constants. Fig. 3.18 shows that the mean flow of velocity in wall coordinates from our simulations follows the law of the wall and is in excellent agreement with that reported in Ref. [97]. RMS velocity profiles also show an excellent agreement, as shown in Fig. 3.19.

The other mean flow properties like skin friction coefficient (C_f), the ratio of bulk mean velocity (U_m) and centreline velocity (U_c) to wall shear velocity (u_τ) show good agreement with

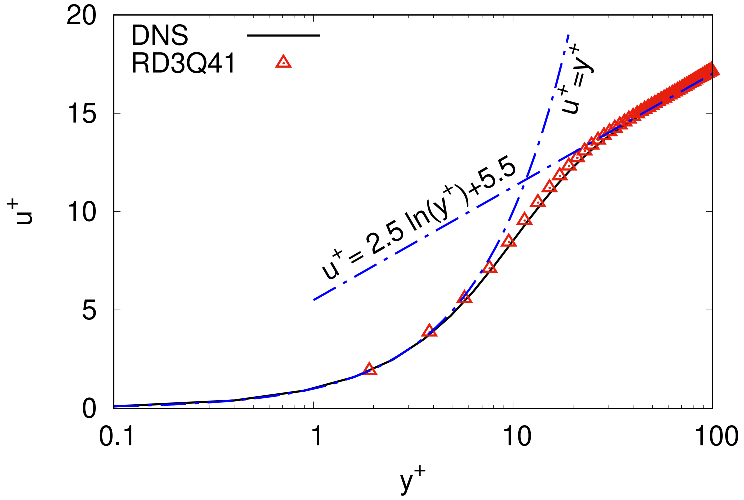

Fig. 3.18 Mean velocity profiles from our simulation (points) and DNS results (line) from [97].

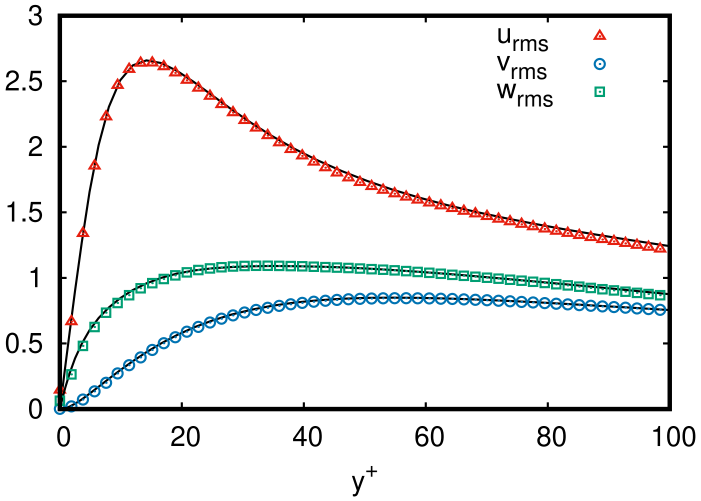

Fig. 3.19 RMS velocity profiles from our simulation (points) and DNS results (line) from [97].

Table 3.3 Mean flow properties from present RD3Q41 simulation and from Ref. [73] at $Re_\tau = 180$.

	C_{f_0}	C_f	U_m/u_τ	U_c/u_τ	U_c/U_m
RD3Q41	5.95×10^{-3}	8.23×10^{-3}	15.58	18.33	1.17
Ref.[73]	6.04×10^{-3}	8.18×10^{-3}	15.63	18.20	1.16

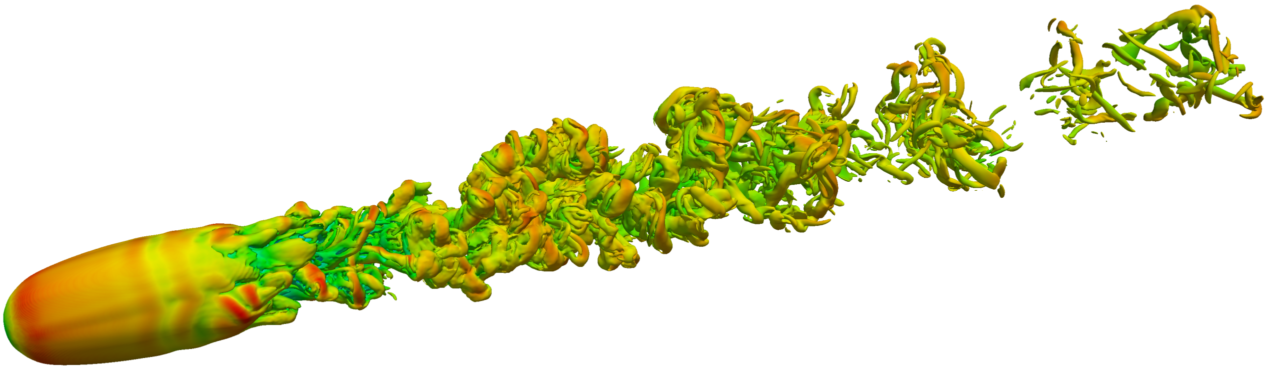

Fig. 3.20 Isovorticity contours of flow over sphere at Reynolds number= 3700.

Kim et al. [73] and are reported in Table 3.3. This shows that the proposed model is well suited to simulate wall-bounded turbulent flows.

3.9.3 Flow past a sphere

Finally we look at the external flows. Flow over a bluff bodies is a well studied problem that is of considerable academic and practical interest. In this section, we simulate flow past a sphere at Reynolds number of 3700. The Reynolds number is defined based on the freestream velocity U_0 and the diameter of the sphere D_0. A computational domain of $[-4.725D_0, 15.525D_0] \times [-6.125D_0, 6.125D_0] \times [-6.125D_0, 6.125D_0]$ is used with 80 grid points per diameter of the sphere and the centre of sphere located at the origin. The inlet and outlet boundary conditions are based on Ref. [41]. A diffused bounce-back boundary condition described in Ref. [76] is implemented on the surface of the sphere. The diffused bounceback condition as a solid-fluid boundary condition is implemented as follows:

Table 3.4 Drag coefficient (C_d), average base pressure coefficient (C_p), recirculation length (L_R), separation angle (ϕ_s).

	C_d	Base C_p	L_R	ϕ_s
DNS [112]	0.394	-0.207	2.28	89.4
LES [145]	0.355	-0.194	2.622	90
Experiments[72]	-	-0.224	-	-
RD3Q41	0.427	-0.211	2.241	90

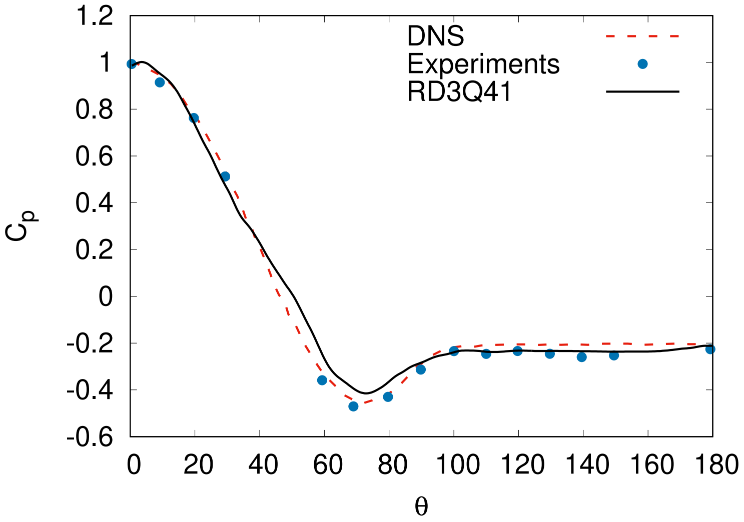

Fig. 3.21 C_p distribution on the surface of the sphere compared with with the experimental [72] and DNS [112] studies.

1. a predictor step similar to Ladd's bounceback [79] is performed on all the boundary points first
2. similar to the kinetic boundary conditions, the wall density at boundary points is evaluated based on these predicted populations
3. for the boundary points, the populations are finally corrected with the equilibrium populations based on this updated density, the velocity of the body and local temperature.

We compare the flow variables such as the drag coefficient, base coefficient pressure, separation angle, and mean recirculation length with the available numerical and experimental data in Table 3.4. The drag coefficient C_d is defined as

$$C_d = \frac{F_D}{\frac{1}{2}\rho U_0^2 A}, \tag{3.56}$$

where F_D is the drag force and $A = \pi D_0^2/4$. The discrepancy in drag coefficient compared to experimental and DNS studies [72, 112] can be attributed to the resolution; accurate drag values and C_p values are typically achieved over 256 points per diameter[49] where as the current simulation was performed with only 80 points per diameter. The recirculation length is defined as the distance between the rear end of the sphere and the location where the velocity in the streamwise direction changes its sign. The angular distribution of the pressure coefficient C_p defined as

$$C_p = \frac{P - P_0}{\frac{1}{2}\rho U_0^2} \tag{3.57}$$

is plotted over the surface of the sphere in Fig. 3.21. C_p profiles from an experimental study, and a DNS study are also shown for reference. It is to be noted that capturing the C_p distribution requires a very high resolution of the sphere [49] while with the current model, we find a reasonable agreement with only 80 points per diameter.

The averaged profile of the velocity in the streamwise direction normalized with the freestream velocity at three different locations ($x/D_0 = 0.2, 1.6, 3.0$) in the wake of the sphere are shown in Fig. 3.22. The averaged profiles of the flow show a good agreement with the DNS [112], LES [145] and experimental [72] studies.

3.10 Conclusion

In this chapter, we have presented an energy conserving lattice Boltzmann model which is suitable for compressible hydrodynamics, aeroacoustics and thermoacoustic problems. It recovers the pressure dynamics and the isentropic sound speed in addition to the effects of viscous heating, heat conduction with a high degree of accuracy. The theoretical requirements and the methodology to construct this model have been discussed, and the test cases confirm its stability for a wide range of parameters. With improved accuracy in the velocity space and better representation of the curved surfaces, this model raises the prospect of direct simulations of turbulent flows involving objects. This has been shown via simulations of Kida-Peltz flow, channel flow and flow past a sphere. The specific heat ratio and Prandtl number of this model are fixed. This restriction on the Prandtl number and specific heat ratio is the subject of the next chapter.

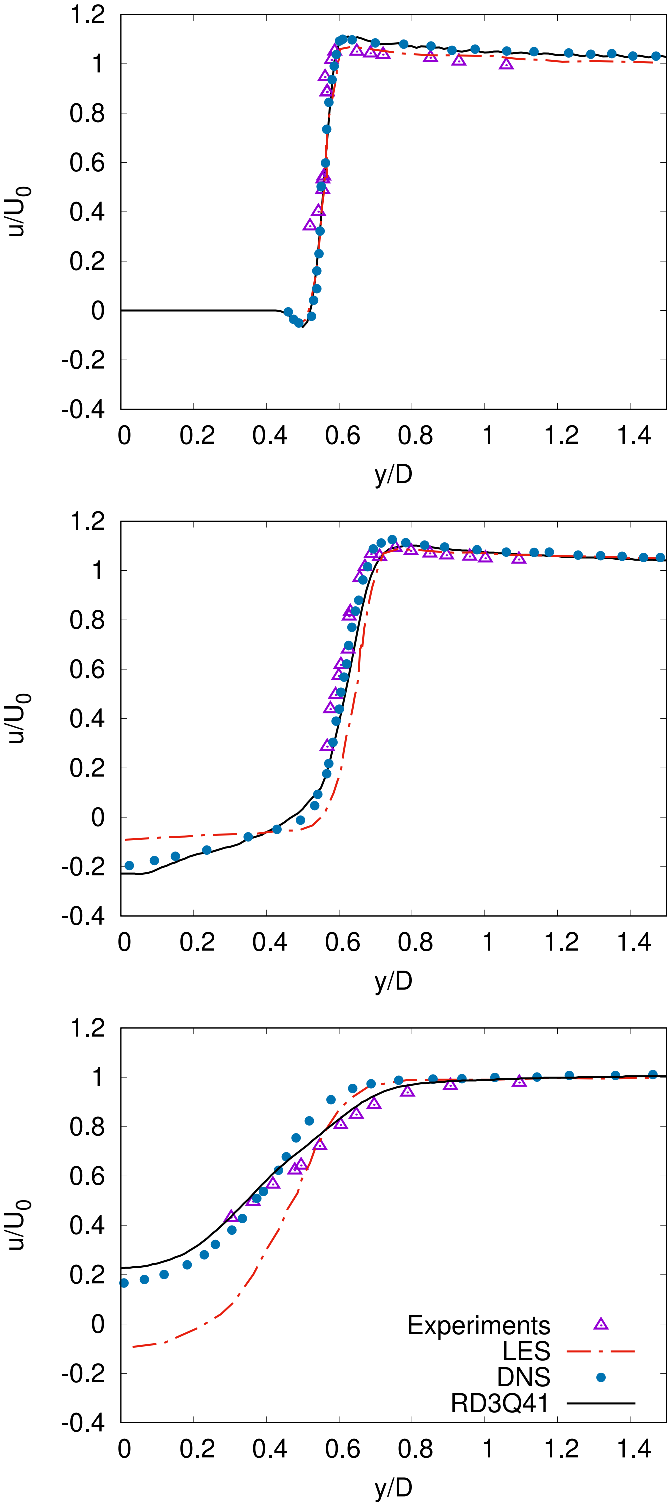

Fig. 3.22 Averaged profile of the normalised velocity at three different locations ($x/D = 0.2, 1.6, 3.0$) in the wake of the sphere from the present study (solid line) compared with DNS [112], LES [145] and experimental [72] studies.

Chapter 4

Reduced kinetic model of polyatomic gases

4.1 Introduction

The dynamics of a dilute monoatomic gas in terms of the single-particle distribution function is described by the Boltzmann equation [32, 35]. Unlike the continuum Navier–Stokes–Fourier hydrodynamics equation, the Boltzmann equation is a valid description even at highly non-equilibrium states [32, 90, 98], encountered in the presence of strong shock waves at high Mach number (ratio of flow speed to sound speed) and in a highly rarefied flow characterized by a large Knudsen number (ratio of the mean free path to characteristic length scale) [8, 103, 125]. However, any analysis of the integro-differential Boltzmann equation is a formidable task, even for the simplest problems. Thus, one often models the Boltzmann dynamics via a simplified collision term that converts the evolution equation to a partial differential equation [3, 6, 7, 23, 56, 63, 86, 87, 116, 121]. An important example is the BGK model [23], which states that the relaxation of the distribution function towards the Maxwell–Boltzmann (MB) form happens in a time scale corresponding to the mean free time τ with the assumption that every moment of the distribution function relaxes at the same rate. The BGK model is quite successful in replicating qualitative features of the Boltzmann dynamics (collisional invariants, the zero of the collision,

---

Work presented in this chapter has been published in

- Journal of Fluid Mechanics - *Reduced kinetic model of polyatomic gases*, Volume 963, Pages A7. ©The Author(s), 2023. Published by Cambridge University Press. Reprinted with permission
- Journal of Computational Sciences - *Extended BGK model for diatomic gases*, Volume 45, Pages 101179. ©2020 Elsevier B.V.

H-theorem, conservation laws, etc). However, the BGK model predicts the Prandtl number of the fluid to be unity, while the value predicted by the Boltzmann equation for monoatomic gas is $2/3$. Thus, several other variations of the collision model such as ES–BGK model [6, 63], the quasi-equilibrium models [56, 87], the Shakhov model [116], and the Fokker-Plank model [121, 123] are used as kinetic models with tunable Prandtl number. The ES–BGK model is a simple but elegant improvement over the BGK model. This model assumes that the distribution function relaxes to an anisotropic Gaussian distribution within mean free time τ. The anisotropic Gaussian in itself evolves towards the MB distribution with a second time scale. The presence of a second time scale as free parameter ensures that the time scales related to momentum and thermal diffusivity are independent and thus permits one to vary the Prandtl number in the range of $2/3$ to ∞.

Despite their success, the Boltzmann collision kernel and its aforementioned simplifications are limited to monoatomic gases as they do not account for the internal molecular structure. However, many real gases such as nitrogen, oxygen, or methane are polyatomic. At the macroscopic level, the internal molecular structure predominantly manifests in terms of modified specific heat ratio γ and bulk viscosity $\eta_{\rm b}$, which is crucial for a number of aerodynamic and turbomachinery engineering applications [135, 142]. The specific heat ratio predicted by the Boltzmann equation is that of a monoatomic gas ($\gamma = 5/3$), whereas that of a diatomic gas is $7/5$.

Two-particle kinetic theory as an extension of the Boltzmann equation as expected correctly predicts the specific heat ratio for polyatomic gases along with heat conductivity and the bulk viscosity [35, 138, 142]. However, it is often not feasible to do any analysis on the Boltzmann-type equation for polyatomic gases. Therefore, several simplifications to model polyatomic gases have also been proposed. They essentially incorporate the rotational kinetic energy by decomposing the two-particle distribution function into two independent single-particle distribution functions [6, 21, 70, 83, 96, 102, 132, 137, 140, 142]. Furthermore, a thermodynamic framework and extensions thereof were developed for modelling highly nonequilibrium phenomena in dense and rarefied polyatomic gases where the Navier–Stokes–Fourier theory is no longer valid [14, 99, 113]. A few BGK like models have also been proposed for polyatomic gases which accept the Prandtl number as a tunable parameter [6, 29].

Hydrodynamic simulations for a realistic system require the development of reduced-order models to account for rotational degrees of freedom ideally without increasing the phase-space dimensionality. Indeed, the standard approach is to demonstrate that the two-particle distribution function describing the translational and rotational degrees of freedom can be approximated by considering two single-particle distribution functions (one for the translational and another for the rotational degrees of freedom) whose dynamics are coupled to each other [6]. However, recently it was pointed out that a simplified description in terms of single-particle distribution function for the translational degree of freedom and a scalar field variable for rotational kinetic energy is sufficient for modelling the change in specific heat ratio for a dilute diatomic gas in the hydrodynamic limit [75]. This model supplemented the standard Boltzmann BGK equation with an advection-relaxation equation for the evolution of rotational energy. It preserved the correct conservation laws for diatomic gases in the hydrodynamic limit and satisfied the H theorem. However, the model was restricted to diatomic gases and a Prandtl number $7/5$, limiting its application for heat transfer problems.

We propose a kinetic model of polyatomic gases to tune Prandtl number, specific heat ratio, and bulk viscosity in a physically transparent fashion. To do so, we write a new collision kernel which is a linear combination of the ES–BGK and BGK kernels that are locally relaxing to different temperatures at different timescales. The ratio of the two relaxation timescales is used to tune the Prandtl number. We couple the evolution of the single-particle distribution function (with this modified collision kernel) via an advection-diffusion-relaxation equation for the rotational energy. The rotational contribution to the internal energy alters the specific heat ratio to that of a polyatomic gas and allows to model bulk viscosity contribution arising out of the rotational degree of freedom. Such an extension of the ES–BGK model indeed reproduces the hydrodynamic behaviour of a polyatomic gas and also has a valid H theorem. These minimal extensions of the ES–BGK model of monoatomic gas are constructed at a single-particle level for polyatomic gases and are phenomenological by construction. It is commensurate with the top-down modelling approach as developed in the context of the lattice Boltzmann models and aim to be analytically and numerically tractable [8, 16, 17, 127]. The present model which requires only the solution of an advection-diffusion-relaxation equation along with the Boltzmann ES–BGK equation adds only a minor complexity over analogous monoatomic gas ES–BGK model and can be implemented in the mesoscale framework such as lattice Boltzmann (LB) method quite easily. This approach is distinctly different and is more detailed than the existing approach in the LB models where the effect of rotational degree of freedom is further coarse-grained and the correction needed to model specific heat ratio is directly added as a force term in the BGK collision model [37, 66, 70, 102]. In contrast, this model of polyatomic gas enlarges the set of microscopic degrees of freedom and models dynamics of rotational energy in an explicit manner.

The chapter is organized as follows: A brief kinetic description of polyatomic gases is given in Sections 4.2. In Section 4.5 an extension to the ES–BGK model for polyatomic gases is proposed. The lattice Boltzmann formulation is described in Section 4.6. The proposed model is numerically validated in Section 4.7. Finally, in Section 4.8, we discuss the outlook of the present work.

4.2 Kinetic description of a polyatomic gas

The dynamics of dilute monoatomic gases is well-described by the Boltzmann equation in terms of the evolution of the single-particle distribution function f, where $f(\boldsymbol{x},\boldsymbol{c},t)\,d\boldsymbol{x}d\boldsymbol{c}$ is the probability of finding a particle within $(\boldsymbol{x},\boldsymbol{x}+d\boldsymbol{x})$, possessing a velocity in the range $(\boldsymbol{c},\boldsymbol{c}+d\mathbf{c})$ at a time t and has been discussed in Chapter 2. The rotational degrees of freedom of a polyatomic gas manifest themselves at the continuum level in terms of change in specific heat ratio γ and a non-zero bulk viscosity due to interaction among the translational component $E_{\rm T}=\rho u^2/2+3\rho\theta_T/2$ and rotational component $E_{\rm R}$ of energy. Thus, the rotational degrees of freedom need to be explicitly accounted for in any microscopic or kinetic description. Indeed, typically the kinetic descriptions are in terms of a two-particle distribution function $F(\boldsymbol{x},\boldsymbol{c},t,I)$, which defines the probability of finding a molecule with a position in the range $(\boldsymbol{x},\boldsymbol{x}+d\boldsymbol{x})$ possessing a velocity in the range $(\boldsymbol{c},\boldsymbol{c}+\boldsymbol{dc})$ in an internal energy parameter range $(I,I+dI)$ due to the additional degrees of freedom [96, 114, 77]. The internal energy due to these additional degrees of freedom is defined by assuming a continuous variable in the internal energy space as $e_{\rm int}=I^{2/\delta}$.

For a polyatomic gas with δ additional rotational degrees of freedom, the moments of this distribution function give the density, momentum, and total energy (with $\delta=0$ corresponding to a monoatomic gas)

$$\{\rho,\rho\boldsymbol{u},E_T+E_R\}=\left\langle\left\langle\left\{1,\boldsymbol{c},\frac{c^2}{2}+I^{2/\delta}\right\},F\right\rangle\right\rangle, \tag{4.1}$$

like its monoatomic counterpart and the operator $\langle\langle,\rangle\rangle$ is defined as $\langle\langle\phi_1(\boldsymbol{c},I),\phi_2(\boldsymbol{c},I)\rangle\rangle=\int\int\phi_1(\boldsymbol{c},I)\phi_2(\boldsymbol{c},I)d\boldsymbol{c}dI$. For the reduced-order modeling, the distribution function $F(\boldsymbol{x},\boldsymbol{c},t,I)$ is often split into two coupled distribution functions $f_1(\boldsymbol{x},\boldsymbol{c},t)$ and $f_2(\boldsymbol{x},\boldsymbol{c},t)$ defined as $f_1(\boldsymbol{x},\boldsymbol{c},t) = \int F(\boldsymbol{x},\boldsymbol{c},I,t)dI$, $f_2(\boldsymbol{x},\boldsymbol{c},t) = \int F(\boldsymbol{x},\boldsymbol{c},I,t)I^{2/\delta}dI$, where f_1 is related to the translational energy and f_2 with the rotational energy dynamics [6, 114]. The moments of reduced distribution $f_1(\boldsymbol{x},\boldsymbol{c},t)$ are then same as the moments of single-particle distribution function $f(\boldsymbol{x},\boldsymbol{c},t)\,d\boldsymbol{x}d\boldsymbol{c}$.

By construction, we have the zeroth moment of $f_2(\boldsymbol{x},\boldsymbol{c},t)$ as the rotational energy

$$E_R = \left\langle\left\langle \frac{c^2}{2} + I^{2/\delta}, F\right\rangle\right\rangle - \left\langle f_1, \frac{c^2}{2}\right\rangle = \left\langle\left\langle F, I^{2/\delta}\right\rangle\right\rangle \equiv \langle f_2, 1\rangle = \frac{\delta}{2}\rho\theta_R. \tag{4.2}$$

In other words, the temperature θ consists of contributions from the translational and rotational temperatures, and they follow the relation

$$\theta = \frac{3}{3+\delta}\theta_T + \frac{\delta}{3+\delta}\theta_R, \tag{4.3}$$

and in thermodynamic equilibrium the equipartition of energy requires $\theta_R = \theta_T$. The heat flux for a polyatomic gas is $q_\alpha = q_\alpha^T + q_\alpha^R$ where q_α^T is the translational heat flux and q_α^R is an additional heat flux due rotational energy.

Like the monoatomic gas, the evolution equation for this distribution function $F(\boldsymbol{x},\boldsymbol{c},t,I)$ with collisional kernel $\Omega(F,F)$ in the Boltzmann form is

$$\partial_t F + c_\alpha \partial_\alpha F = \Omega(F,F), \tag{4.4}$$

which is consistent with the equipartition of energy at equilibrium [107, 77]. Similar to the monoatomic gas, one defines the BGK collision kernel in terms of the two-particle distribution function for a polyatomic gas as [29]

$$\begin{aligned} \Omega_{\mathrm{BGK}} &= \frac{1}{\tau}\left(F^{\mathrm{MB}}(\rho,\boldsymbol{u},\theta,I) - F\right), \\ F^{\mathrm{MB}}(\rho,\boldsymbol{u},\theta,I) &= \frac{\rho\Lambda_\delta}{(2\pi\theta)^{3/2}\theta^{\delta/2}}\exp\left(-\left(\frac{(\boldsymbol{c}-\boldsymbol{u})^2}{2\theta} + \frac{I^{2/\delta}}{\theta}\right)\right), \end{aligned} \tag{4.5}$$

with normalisation factor $\Lambda_\delta = \int \exp(-I^{2/\delta})dI$. Equation (4.4) with Ω_{BGK} is written as two kinetic equations for the reduced distributions $f_1(\boldsymbol{x},\boldsymbol{c},t)$ and $f_2(\boldsymbol{x},\boldsymbol{c},t)$ by multiplying with 1 and $I^{2/\delta}$ and then integrating over the internal energy variable as

$$\begin{aligned}\partial_t f_1 + c_\alpha \partial_\alpha f_1 &= \frac{1}{\tau}\left(f_1^{\mathrm{MB}}(\rho, \boldsymbol{u}, \theta) - f_1\right), \\ \partial_t f_2 + c_\alpha \partial_\alpha f_2 &= \frac{1}{\tau}\left(\frac{\delta}{2}\theta f_1^{\mathrm{MB}}(\rho, \boldsymbol{u}, \theta) - f_2\right).\end{aligned} \tag{4.6}$$

This approach, where two reduced distributions are weakly coupled via temperature, recovers all the features of Eq.(4.4) and is widely adopted for polyatomic gases. [6] extended this approach via an extended ES–BGK collision kernel as

$$\Omega_{\mathrm{ESBGK}}(F) = \frac{Z_{\mathrm{ES}}}{\tau}\left(F^{\mathrm{ES}}(\rho, u, \lambda_{ij}, \theta_{\mathrm{rel}}) - F\right), \tag{4.7}$$

where $\lambda_{ij} = (1-\alpha)\left[(1-b)\theta_T \delta_{ij} + b\Theta_{ij}\right] + \alpha\theta\delta_{ij}$ with a generalized Gaussian F^{ES}

$$F^{\mathrm{ES}}(\rho, u, \lambda_{ij}, \theta_{\mathrm{rel}}) = \frac{\rho\Lambda_\delta}{\theta_{\mathrm{rel}}^{\delta/2}\sqrt{\det[2\pi\lambda_{\mathrm{ij}}]}} \exp\left(-\frac{1}{2}\xi_i \lambda_{ij}^{-1}\xi_j - \frac{I^{2/\delta}}{\theta_{\mathrm{rel}}}\right), \tag{4.8}$$

with $\theta_{\mathrm{rel}} = \alpha\theta + (1-\alpha)\theta_R$ and $Z_{\mathrm{ES}} = 1/(1-b+b\alpha)$. Similar to the monoatomic ES–BGK model, the parameter b is used to tune the Prandtl number, while parameter α is used to tune the bulk viscosity coefficient independently. The reduced description which generalizes the ES–BGK model in terms of the f_1 and f_2 is

$$\begin{aligned}\partial_t f_1 + c_\alpha \partial_\alpha f_1 &= \frac{Z_{\mathrm{ES}}}{\tau}\left(f^{\mathrm{ES}}(\rho, u, \lambda_{ij}) - f_1\right), \\ \partial_t f_2 + c_\alpha \partial_\alpha f_2 &= \frac{Z_{\mathrm{ES}}}{\tau}\left(\frac{\delta}{2}\theta_{\mathrm{rel}} f^{\mathrm{ES}}(\rho, u, \lambda_{ij}) - f_2\right).\end{aligned} \tag{4.9}$$

For polyatomic gases, the energy equation gets an additional contribution from the rotational energy. In both the BGK and ES–BGK models, the evolution equation for translational part of the energy and the rotational part of the energy $E_R = \delta\rho\theta_R/2$ are of the form

$$\begin{aligned}\partial_t E_T + \partial_\alpha\left[(E_T + \rho\theta)u_\alpha + q_\alpha^T + u_\gamma \hat{\sigma}_{\alpha\gamma}\right] &= \frac{Z_E}{\tau}\frac{3\rho}{2}(\theta - \theta_T), \\ \partial_t E_R + \partial_\alpha\left(E_R u_\alpha + q_\alpha^R\right) &= \frac{Z_E}{\tau}\frac{\delta\rho}{2}(\theta - \theta_R),\end{aligned} \tag{4.10}$$

with $Z_E = 1$ for the BGK model and $Z_E = \alpha Z_{\mathrm{ES}}$ for the ES–BGK model. The evolution equation for the total energy is written as the sum of Eqs. (4.10) as

$$\partial_t \left(E_T + E_R\right) + \partial_\alpha \left[\left(E_T + E_R + \rho\theta\right) u_\alpha + q_\alpha + u_\gamma \hat{\sigma}_{\alpha\gamma}\right] = 0, \tag{4.11}$$

where the relationship between translational, rotational temperatures (Eq.(4.3)) is used to show that energy is collisional invariant.

From Eqs. (4.6) and (4.9), the stress evolution and the translational heat flux evolution equations in explicit form are

$$\begin{aligned}
&\partial_t \sigma_{\alpha\beta} + \partial_\gamma \left(u_\gamma \sigma_{\alpha\beta}\right) + \partial_\gamma \overline{Q_{\alpha\beta\gamma}} + \frac{4}{5}\overline{\partial_\beta q^T_\alpha} + 2\rho\theta_T \overline{\partial_\beta u_\alpha} + 2\overline{\partial_\gamma u_\alpha \sigma_{\gamma\beta}} = -\frac{1}{\tau}\sigma_{\alpha\beta},\\
&\quad \partial_t q^T_\alpha + \partial_\beta \left(u_\beta q^T_\alpha\right) + \overline{Q_{\alpha\beta\gamma}}\partial_\beta u_\gamma + \frac{1}{2}\partial_\beta R_{\alpha\beta} + \frac{7}{5} q^T_\beta \partial_\beta u_\alpha + \frac{2}{5} q^T_\alpha \partial_\eta u_\eta + \frac{2}{5} q^T_\beta \partial_\alpha u_\beta\\
&\quad -\frac{5}{2}\theta_T \partial_\alpha(\rho\theta_T) - \frac{\sigma_{\alpha\beta}}{\rho}\partial_\beta(\rho\theta_T) - \frac{5}{2}\theta_T \partial_\kappa \sigma_{\kappa\alpha} - \frac{\sigma_{\alpha\beta}}{\rho}\partial_\kappa \sigma_{\kappa\beta} = -\frac{Z_q}{\tau} q^T_\alpha,
\end{aligned} \tag{4.12}$$

with $Z_q = 1$ for BGK and $Z_q = Z_{\mathrm{ES}}$ for the ES–BGK model. Multiplying rotational energy equation from Eq.(4.10) with u_α and using velocity evolution we have

$$\partial_t \left(E_R u_\alpha\right) + \partial_\beta \left(E_R u_\alpha u_\beta\right) + u_\alpha \partial_\beta q^R_\beta + \frac{E_R}{\rho}\partial_\beta \left(\rho\theta\delta_{\alpha\beta} + \hat{\sigma}_{\alpha\beta}\right) = \frac{Z_E}{\tau}\frac{\delta}{2}\rho u_\alpha \left(\theta - \theta_R\right). \tag{4.13}$$

The rotational heat flux evolution can be obtained as first moment of f_2 dynamics as

$$\partial_t q^R_\alpha + \partial_\beta \left(u_\beta q^R_\alpha\right) + q^R_\beta \partial_\beta u_\alpha + \partial_\beta \sigma^R_{\alpha\beta} + \partial_\alpha \left(\rho\theta^2\right) - \frac{\delta}{2}\theta_R \partial_\beta \left(\rho\theta\delta_{\alpha\beta} + \hat{\sigma}_{\alpha\beta}\right) = -\frac{Z_q}{\tau} q^R_\alpha. \tag{4.14}$$

A Chapman-Enskog analysis shows that the momentum equation yields the familiar compressible Navier–Stokes equation form as

$$\partial_t(\rho u_\alpha) + \partial_\beta(\rho u_\alpha u_\beta) + \partial_\alpha p - \partial_\beta \left(2\eta\overline{\partial_\beta u_\alpha} + \eta_b \partial_\kappa u_\kappa \delta_{\alpha\beta}\right) = 0 \tag{4.15}$$

with the shear and bulk viscosities

$$\eta = p\tau, \qquad \frac{\eta_b}{\eta} = \frac{2\delta}{3(3+\delta)Z_E}. \tag{4.16}$$

Similarly, an analysis of the translational and rotational heat flux dynamics at $O(\mathrm{Kn})$ leads to $q^T_\alpha = -\kappa_T \partial_\alpha \theta$, $q^R_\alpha = -\kappa_R \partial_\alpha \theta$, with the translational and rotational thermal conductivities

$\kappa_T = 5p\tau/(2Z_q)$, $\kappa_R = \delta p\tau/(2Z_q)$ respectively. The effective thermal conductivity $\kappa = \kappa_T + \kappa_R = (5+\delta)p\tau/(2Z_q)$ Thus, the Prandtl number is $\mathrm{Pr} = Z_q$ i.e., $\mathrm{Pr} = 1$ for BGK model and $\mathrm{Pr} = 1/(1-b+b\alpha)$ for the ES–BGK model.

In the kinetic theory of gases, one often builds an extended moment system in terms of physically relevant lower-order moments [57]. In this spirit of Grad's moment method, one may ask whether a reduced description for rotational degrees of freedom is feasible. It should be noted that the evolution equation of f_1 is only weakly coupled with the evolution of f_2 via θ_R. An appropriate choice in the current context is a reduced description in terms of lower-order moments of second distribution f_2. For example, the rotational component can be modelled by the evolution of two scalars – rotational energy and its flux (which are the zeroth and the first moment of f_2). Such a class of reduced-order kinetic models might be better suited for large-scale hydrodynamic simulations.

4.3 Energy conserving kinetic model for a diatomic gas

The collision relaxation towards equilibrium for a diatomic gas can be interpreted as a two-step process, each having its own timescale. In the first step, the particles undergo collisions due to which the translational kinetic energy relaxes to its equilibrium value over a timescale τ. During the second step, due to more collisions, the rotational kinetic energy relaxes to its equilibrium value over a timescale τ_1.

Here, we remind that for diatomic or polyatomic gases, the rotational degrees of freedom have multiple effects on the dynamics. The leading order change is thermodynamic, where c_P and γ are changed [36]. The next order is a small departure from equilibrium where local thermodynamic equilibrium is a good approximation, and Navier-Stokes-Fourier equations can be used. At this level, the role of additional degrees of freedom is to modify the transport properties, leading to phenomena like non-zero bulk viscosity and enhanced thermal conductivity due to rotational heat flux [34]. Finally, in a highly non-equilibrium situation (encountered for high Mach or high-frequency dynamics), the rotational temperature relaxes much more slowly than the translational temperature. In such scenarios, assuming instantaneous equilibration between translational and rotational degrees of freedom is inadequate and requires an additional time scale τ_1 for the relaxation of rotational temperature [34, 96].

A single particle distribution function is used to model the hydrodynamics via a Boltzmann-BGK-like model

$$\partial_t f(\mathbf{x},\mathbf{c},t)+(\boldsymbol{c}\cdot\nabla)f(\mathbf{x},\mathbf{c},t)=\frac{1}{\tau}\left[f^{\mathrm{MB}}(\rho(\mathbf{x},t),\boldsymbol{u}(\mathbf{x},t),\theta(\mathbf{x},t))-f(\mathbf{x},\mathbf{c},t)\right]. \tag{4.17}$$

The kinetic-equation is supplemented with an advection-relaxation type equation to describe the evolution of rotational energy [61]

$$\partial_t\left[\rho\theta_R(\mathbf{x},t)\right]+\nabla\cdot\left[\rho\theta_R(\mathbf{x},t)\,\boldsymbol{u}(\mathbf{x},t)\right]=\frac{\rho\theta_T(\mathbf{x},t)-\rho\theta_R(\mathbf{x},t)}{\tau_1}, \tag{4.18}$$

where τ,τ_1 are the relaxation rates for the translational and rotational energies respectively. The conservation laws for the mass and momentum can be obtained by taking the zeroth and first moment of the Eq.(4.17) as

$$\partial_t\rho+\partial_\alpha(\rho u_\alpha)=0, \tag{4.19}$$

and

$$\partial_t(\rho u_\alpha)+\partial_\beta\left(\rho u_\alpha u_\beta+\rho\theta_T\delta_{\alpha\beta}+\sigma_{\alpha\beta}\right)=0. \tag{4.20}$$

We define a modified stress tensor $\hat{\sigma}_{\alpha\beta}=\rho(\theta_T-\theta)\delta_{\alpha\beta}+\sigma_{\alpha\beta}$ and use the relation $p=\rho\theta$ to rewrite the Eq.(4.20) as

$$\partial_t(\rho u_\alpha)+\partial_\beta\left(\rho u_\alpha u_\beta+p\delta_{\alpha\beta}+\hat{\sigma}_{\alpha\beta}\right)=0. \tag{4.21}$$

The evolution of the translational kinetic energy and internal energy can be computed as the second moment of the Eq.(4.17)

$$\partial_t\left(\frac{\rho u^2}{2}+\frac{3\rho\theta_T}{2}\right)+\partial_\beta\left[\left(\frac{\rho u^2}{2}+\frac{5\rho\theta_T}{2}\right)u_\beta+\sigma_{\beta\gamma}u_\gamma+q_\beta\right]=\frac{3\rho}{2\tau}\left[\theta-\theta_T\right]. \tag{4.22}$$

Similarly, the evolution of the rotational energy is obtained from the Eq.(4.18) is

$$\partial_t(\rho\theta_R)+\partial_\alpha(\rho\theta_R u_\alpha)=\frac{\rho}{\tau_1}(\theta_T-\theta_R). \tag{4.23}$$

Therefore, the total energy (E) is defined as the sum of rotational and translational energies is

$$E=\frac{1}{2}(\rho u^2+3\rho\theta_T)+\rho\theta_R, \tag{4.24}$$

which along with Eq.(4.3) gives

$$E = \frac{1}{2}\rho u^2 + \frac{5}{2}\rho\theta. \tag{4.25}$$

The evolution of the total energy obtained by adding Eqs.(4.22) and (4.23) is

$$\partial_t E + \partial_\beta \left[E u_\beta + \rho\theta_T u_\beta + \sigma_{\beta\gamma} u_\gamma + q_\beta\right] = \frac{3\rho}{2\tau}\left[\theta - \theta_T\right] + \frac{\rho}{\tau_1}\left(\theta_T - \theta_R\right). \tag{4.26}$$

As the total energy is conserved during a collision, the right-hand side of the above equation must vanish, which fixes the ratio of the relaxation times τ and τ_1 using Eq.(4.3) to be

$$\tau_1 = \frac{5}{3}\tau. \tag{4.27}$$

This reduces Eq.(4.26) to,

$$\partial_t E + \partial_\beta \left[E u_\beta + p u_\beta + \hat{\sigma}_{\beta\gamma} u_\gamma + q_\beta\right] = 0, \tag{4.28}$$

the total energy equation in the final form in terms of p and $\hat{\sigma}_{\beta\gamma}$. Therefore, we see that the conservation laws for the current model are correct. In the next section, we propose a way to overcome this restriction on the ratio of relaxation times by relaxing the temperature to a modified temperature which is tunable based on the relaxation times.

4.4 Extended BGK Model for diatomic gas with variable relaxation time ratios

To overcome the restriction on the ratios of relaxation times to $5/3$, we propose another model where the single-particle distribution function is relaxed to a non-physical temperature θ_1 locally as

$$\partial_t f(\mathbf{x},\mathbf{c},t) + (\boldsymbol{c}\cdot\nabla) f(\mathbf{x},\mathbf{c},t) = \frac{1}{\tau}\left[f^{\mathrm{MB}}(\rho(\mathbf{x},t), \boldsymbol{u}(\mathbf{x},t), \theta_1(\mathbf{x},t)) - f(\mathbf{x},\mathbf{c},t)\right]. \tag{4.29}$$

The form of temperature θ_1 is determined by the energy conservation and derived in the next few steps. The conservation laws for mass and momentum remain the same as the previous model and follow Eq.(4.19) and Eq.(4.21). The evolution of the translational kinetic energy and internal energy is determined by the second moment of the Eq.(4.29)

$$\partial_t\left(\frac{\rho u^2}{2}+\frac{3\rho\theta_T}{2}\right)+\partial_\beta\left[\left(\frac{\rho u^2}{2}+\frac{5\rho\theta_T}{2}\right)u_\beta+\sigma_{\beta\gamma}u_\gamma+q_\beta\right]=\frac{3\rho}{2\tau}\left[\theta_1-\theta_T\right]. \tag{4.30}$$

and the evolution of the rotational energy is the same as the previous model and is given by Eq.(4.18) and is rewritten here

$$\partial_t\left(\rho\theta_R\right)+\partial_\alpha\left(\rho\theta_R u_\alpha\right)=\frac{\rho}{\tau_1}\left(\theta_T-\theta_R\right). \tag{4.31}$$

Evolution of total energy is given by adding Eqns.(4.30) and (4.31) is

$$\partial_t E+\partial_\beta\left[Eu_\beta+\rho\theta_T u_\beta+\sigma_{\beta\gamma}u_\gamma+q_\beta\right]=\frac{3\rho}{2\tau}\left[\theta_1-\theta_T\right]+\frac{\rho}{\tau_1}\left(\theta_T-\theta_R\right). \tag{4.32}$$

As the total energy is conserved during collision, the right hand side of the above equation is set to zero, which leads to the following form of θ_1:

$$\theta_1=\left[1-\frac{2\tau}{3\tau_1}\right]\theta_T+\frac{2\tau}{3\tau_1}\theta_R. \tag{4.33}$$

This ensures that the conservation laws for the proposed model are exactly similar to that of the previous model and of a diatomic gas. It is to be noted that the previous model is indeed a special case of the current model when the ratio of relaxation times(τ_1/τ) is set to $5/3$.

In the next section, we will prove the H theorem, an essential feature of the kinetic theory, for both the proposed models.

- **The H theorem:**

  We now prove the H theorem for both the proposed kinetic models of the diatomic gas. Motivated by the form of Sackur-Tertrode entropy [65], and assuming that rotational energy can be described in terms of ρ and θ_R, we choose a quantity H_1 as

  $$H_1=H+k\rho\ln\theta_R, \tag{4.34}$$

  where $H=\int d\boldsymbol{c} f\ln f$, and k is an unknown factor.

  - **For model with fixed relaxation time ratio:**

    On multiplying Eq.(4.17) with $\ln f$, and integrating over the velocity space we obtain the evolution of H as

$$\partial_t H + \nabla \cdot J^H = \frac{1}{\tau} \int \left(\left(f^{\mathrm{MB}}(\rho, \boldsymbol{u}, \theta) - f \right) \ln \left(\frac{f}{f^{\mathrm{MB}}(\rho, \boldsymbol{u}, \theta)} \right) \right) d\boldsymbol{c} - \frac{3\rho}{2\tau} \frac{\theta - \theta_T}{\theta}, \tag{4.35}$$

where J^H is related to the flux of the entropy. The evolution of the rotational energy [Eq.(4.18)] can be rewritten in a simplified form as

$$\partial_t \ln \theta_R + \boldsymbol{u} \cdot \nabla \ln \theta_R = \frac{\theta_T - \theta_R}{\tau_1 \theta_R}. \tag{4.36}$$

Multiplying the above equation with ρ and exploiting continuity and Eq.(4.27) we obtain

$$\partial_t \left(\rho \ln \theta_R \right) + \nabla \cdot \left(\rho \boldsymbol{u} \ln \theta_R \right) = -\frac{5\rho}{2\tau_1} \frac{\theta - \theta_T}{\theta_R}. \tag{4.37}$$

Thus, by adding Eq.(4.66) and Eq.(4.68) the evolution of H_1 is obtained as

$$\partial_t H_1 + \nabla \cdot \left(J^H + k \rho \boldsymbol{u} \ln \theta_R \right) = \Omega, \tag{4.38}$$

where the entropy production Ω is

$$\Omega = \frac{1}{\tau} \int \left(\left(f^{\mathrm{MB}}(\rho, \boldsymbol{u}, \theta) - f \right) \ln \left(\frac{f}{f^{\mathrm{MB}}(\rho, \boldsymbol{u}, \theta)} \right) \right) d\boldsymbol{c} - \frac{\rho}{2} \left(\theta - \theta_T \right) \left[\frac{3}{\tau \theta} + \frac{5k}{\tau_1 \theta_R} \right]. \tag{4.39}$$

We now choose $k = -1$, and use Eqns. (4.3), (4.27), to obtain

$$\begin{aligned} \Omega &= \frac{1}{\tau} \int \left(\left(f^{\mathrm{MB}}(\rho, \boldsymbol{u}, \theta) - f \right) \ln \left(\frac{f}{f^{\mathrm{MB}}(\rho, \boldsymbol{u}, \theta)} \right) \right) d\boldsymbol{c} - \frac{3\rho}{2\tau \theta \theta_R} \left(\theta - \theta_T \right) \left(\theta_R - \theta \right) \\ &= \frac{1}{\tau} \int \left(\left(f^{\mathrm{MB}}(\rho, \boldsymbol{u}, \theta) - f \right) \ln \left(\frac{f}{f^{\mathrm{MB}}(\rho, \boldsymbol{u}, \theta)} \right) \right) d\boldsymbol{c} - \frac{\rho}{\tau \theta \theta_R} \left(\theta - \theta_R \right)^2 \\ &\leq 0. \end{aligned} \tag{4.40}$$

We see that the entropy production Ω is non-positive, hence the proposed kinetic model satisfies the H theorem.

- **Model with variable relaxation time ratio:**

  Similar to the previous model, one can write the entropy production Ω for the current model as

$$\Omega = \frac{1}{\tau}\int\left(\left(f^{\mathrm{MB}}(\rho,\boldsymbol{u},\theta)-f\right)\ln\left(\frac{f}{f^{\mathrm{MB}}(\rho,\boldsymbol{u},\theta)}\right)\right)d\boldsymbol{c}-\frac{3\rho}{2\tau}\left(\theta_1-\theta_T\right)\left[\frac{1}{\theta_1}+\frac{k}{\theta_R}\right]. \tag{4.41}$$

We now choose $k=-1$, and substitute $(\theta_R-\theta_1)$ from Eq.(4.33) to obtain

$$\begin{aligned}\Omega &= \frac{1}{\tau}\int\left(\left(f^{\mathrm{MB}}(\rho,\boldsymbol{u},\theta)-f\right)\ln\left(\frac{f}{f^{\mathrm{MB}}(\rho,\boldsymbol{u},\theta)}\right)\right)d\boldsymbol{c}-\frac{3\rho}{2\tau\theta_1\theta_R}\left(\theta_1-\theta_T\right)\left[\theta_R-\theta_1\right]\\ &= \frac{1}{\tau}\int\left(\left(f^{\mathrm{MB}}(\rho,\boldsymbol{u},\theta)-f\right)\ln\left(\frac{f}{f^{\mathrm{MB}}(\rho,\boldsymbol{u},\theta)}\right)\right)d\boldsymbol{c}-\frac{3\rho}{2\tau\theta_1\theta_R}\left[\frac{3\tau_1}{2\tau}-1\right]\left(\theta_1-\theta_T\right)^2\\ &\leq 0.\end{aligned} \tag{4.42}$$

Assuming that the two relaxation times are of the same order, we see that the entropy production Ω is non-positive and hence satisfies the *H* theorem. This feature of the model can be exploited to write a nonlinearly stable numerical scheme [10, 17].

- **Hydrodynamics:**

  In this section, via a Chapman-Enskog analysis we show that the macroscopic equations obtained from both the proposed models match the energy conserving hydrodynamic description of a diatomic gas [32].

  For the Chapman-Enskog analysis, the distribution function and time derivative are expanded in powers of smallness parameter τ as

$$f = f^{(0)}+\tau f^{(1)}+\cdots \tag{4.43}$$

$$\partial_t\phi = \partial_t^{(0)}\phi+\tau\partial_t^{(1)}\phi+\cdots. \tag{4.44}$$

  Based on their relaxation rate, the moments are categorized into slow moments (M^{slow}) and fast moments (M^{fast}). The conserved quantities i.e, mass, momentum and total energy are slow moments and are not perturbed from their equilibrium values

$$M^{\mathrm{slow}} = \left\{\rho,\rho u_\alpha,\frac{1}{2}(\rho u^2+5\rho\theta)\right\}. \tag{4.45}$$

Translational and rotational temperatures along with the higher moments (the stress and heat flux) are the fast moments

$$M^{\text{fast}} = \left\{\theta_T, \theta_R, \sigma_{\alpha\beta}\right\}. \tag{4.46}$$

The relation between the base states for perturbation for θ_T, θ_R and θ are obtained from zero of collision from Eq.(4.22) and Eq.(4.23) as

$$\theta = \theta_T \qquad \text{and} \qquad \theta_{\mathrm{T}} = \theta_{\mathrm{R}}. \tag{4.47}$$

Similarly for a variable relaxation time ratio model, we have

$$\theta_1 = \theta_T \qquad \text{and} \qquad \theta_{\mathrm{T}} = \theta_{\mathrm{R}}. \tag{4.48}$$

This relation suggests that the base state for all the temperatures is the same θ [Eq.(4.3)]. Substituting the expansion of time derivative in the conservation laws we obtain the following at the zeroth-order:

$$\begin{aligned} \partial_t^{(0)}\rho + \partial_\alpha\left(\rho u_\alpha\right) &= 0, \\ \partial_t^{(0)}\left(\rho u_\alpha\right) + \partial_\beta\left(\rho u_\alpha u_\beta + \rho\theta\delta_{\alpha\beta}\right) &= 0, \\ \partial_t^{(0)}\left(\frac{\rho u^2}{2} + \frac{5}{2}\rho\theta\right) + \partial_\alpha\left[u_\alpha\left(\frac{\rho u^2}{2} + \frac{5}{2}\rho\theta\right) + \rho\theta u_\alpha\right] &= 0. \end{aligned} \tag{4.49}$$

It can be verified that the above set of equations satisfy the evolution of pressure

$$\left(\partial_t^{(0)} + u_\beta\partial_\beta\right)\left(\frac{p}{\rho^\gamma}\right) = 0, \tag{4.50}$$

At $O(\tau)$ the conservation laws are

$$\begin{aligned} \partial_t^{(1)}\rho &= 0, \\ \partial_t^{(1)}\left(\rho u_\alpha\right) + \partial_\alpha(\rho\theta_T^{(1)}) + \partial_\beta\sigma_{\alpha\beta}^{(1)} &= 0, \\ \partial_t^{(1)}E + \partial_\beta\left(\sigma_{\alpha\beta}^{(1)}u_\alpha + \rho\theta_T^{(1)}u_\beta + q_\beta^{(1)}\right) &= 0. \end{aligned} \tag{4.51}$$

Momentum equation from Eq. (4.76) and Eq. (4.78) is

$$\partial_t(\rho u_\alpha) + \partial_\beta \left(\rho u_\alpha u_\beta + \rho\theta\delta_{\alpha\beta}\right) + \left(\partial_\alpha(\tau\rho\theta_T^{(1)}) + \partial_\beta(\tau\sigma_{\alpha\beta}^{(1)})\right) = 0 \tag{4.52}$$

From the evolution equations of translational temperature and stress tensor the values of $\rho\theta_T^{(1)}$ and $\sigma_{\alpha\beta}^{(1)}$ are obtained to be

$$\begin{aligned} \rho\theta_T^{(1)} &= -\frac{4}{15}\rho\theta\partial_\gamma u_\gamma \\ \sigma_{\alpha\beta}^{(1)} &= -2\rho\theta\overline{\partial_\beta u_\alpha}. \end{aligned} \tag{4.53}$$

Substituting these values in Eq.(4.52) we have

$$\partial_t(\rho u_\alpha) + \partial_\beta(\rho u_\alpha u_\beta) + \partial_\alpha p - \partial_\beta\left(2\tau p\,\overline{\partial_\beta u_\alpha} + \frac{4\tau p}{15}\delta_{\alpha\beta}\partial_\kappa u_\kappa\right) = 0. \tag{4.54}$$

We obtain the Navier-Stokes equation

$$\partial_t(\rho u_\alpha) + \partial_\beta(\rho u_\alpha u_\beta) + \partial_\alpha p - \partial_\beta\left(2\eta\overline{\partial_\beta u_\alpha} + \eta_b\partial_\kappa u_\kappa\delta_{\alpha\beta}\right) \tag{4.55}$$

with shear viscosity (η) and bulk viscosity (η_b) values of

$$\begin{aligned} \eta &= p\tau \qquad \text{and} \\ \eta_b &= \frac{4p\tau}{15} \equiv \frac{4\eta}{15}. \end{aligned} \tag{4.56}$$

The relation between shear and bulk viscosities in terms of number of internal degrees freedom matches with the value reported in [102]

$$\eta_b = \frac{2S}{D(D+S)}\eta \tag{4.57}$$

where S is the number of internal degrees of freedom.

It should be noted that bulk viscosity for a monoatomic gas is zero and the non-zero bulk viscosity is due to the rotational energy.

In the next sections, we propose a kinetic model with both tunable specific heat ratio and Prandtl number.

4.5 Reduced ES–BGK model for polyatomic gases

An extended BGK model for diatomic gases was formulated by [75] wherein the BGK collision model was coupled with the rotational part of energy (zeroth moment of f_2) which in itself follows an advection-relaxation equation.

We extend this approach by a generalized ES-BGK model for polyatomic gases with tunable Prandtl numbers where the collision term is a linear combination of ES–BGK and the BGK collision kernels. In this model, the ES–BGK term describes relaxation to a temperature θ_T over a time τ whereas the BGK collision kernel describes relaxation to a temperature θ over a time τ_1. The kinetic equation of the unified model along with the evolution equation for the rotational energy is

$$\begin{aligned}
\partial_t f_1 + c_\alpha \partial_\alpha f_1 &= \frac{1}{\tau}\left(f^{\mathrm{ES}}(\rho, \boldsymbol{u}, \theta_T \delta_{\alpha\beta} + b\sigma_{\alpha\beta}) - f_1\right) + \frac{1}{\tau_1}\left(f^{\mathrm{MB}}(\rho, \boldsymbol{u}, \theta) - f_1\right), \\
\partial_t (E_R) + \partial_\alpha \left(E_R u_\alpha + q^R_\alpha\right) &= \frac{1}{\tau_1}\left(\frac{\delta}{2}\rho\theta - E_R\right),
\end{aligned} \tag{4.58}$$

with the form of heat flux due to internal degrees of freedom as

$$q^R_\alpha = -\kappa_R \partial_\alpha \theta_R. \tag{4.59}$$

This model is a minimal extension of the monoatomic ES–BGK model needed for modeling polyatomic gases which also recovers all important features such as the positivity, macroscopic limit, and the H theorem. Here, the Prandtl number is a tunable parameter due to the presence of two relaxation time scales, whereas the rotational part of the internal energy alters the specific heat ratio to that of a polyatomic gas. The model satisfies the H theorem, thus ensuring convergence to a unique equilibrium state. A few important characteristic of the present model are as follows:

- **Conservation Laws**: The mass and momentum conservation equations for the proposed model are obtained by taking the zeroth and first moments of f_1 evolution (Eq.(4.58)). The second moment signifying translational energy evolution equation is

$$\partial_t E_T + \partial_\beta \left[(E_T + \rho\theta_T) u_\beta + \sigma_{\beta\gamma} u_\gamma + q^T_\beta\right] = \frac{\rho}{\tau_1}\left(\frac{3}{2}\theta - \frac{3}{2}\theta_T\right), \tag{4.60}$$

which when combined with the rotational energy equation shows that the total energy is conserved. This implies that the evolution equation for slow moments

$$M_{\text{slow}} = \left\{ \rho, \rho u_\alpha, \frac{1}{2}\rho u^2 + \frac{3+\delta}{2}\rho\theta) \right\}, \tag{4.61}$$

mass density, momentum density, and total energy density are

$$\begin{aligned} \partial_t \rho + \partial_\alpha(\rho u_\alpha) &= 0, \\ \partial_t(\rho u_\alpha) + \partial_\beta \left(\rho u_\alpha u_\beta + \rho\theta\delta_{\alpha\beta} + \hat{\sigma}_{\alpha\beta}\right) &= 0, \\ \partial_t\left(E_T + E_R\right) + \partial_\beta\left[\left(E_T + E_R + \rho\theta\right)u_\beta + \hat{\sigma}_{\beta\gamma}u_\gamma + q_\beta\right] &= 0. \end{aligned} \tag{4.62}$$

Thus, the conservation laws have correct macroscopic form.

It should also be noted that diatomic and polyatomic gases exhibit non-vanishing angular momentum. For such molecules, the total angular momentum indeed has two components: the angular momentum around the center of inertia of the molecule and the intrinsic rotational angular momentum. However, as demonstrated by Rykov [114] via a scaling analysis, the rotational contribution to the total angular momentum is negligible compared to the angular momentum due to the motion of the centre of mass. Let's define the angular momentum due to rotation as $\mathbf{M}$ with a rotational moment of inertia J and a mean angular velocity $\boldsymbol{\omega}$. From the equipartition of energy at equilibrium for a molecule of mass m with a mean translational velocity $\mathbf{v}$, we have the following relation between one translational and one rotational degree of freedom (for a diatomic gas):

$$\frac{1}{3}\frac{mv^2}{2} = \frac{1}{2}\frac{M^2}{2J} \equiv \frac{1}{2}\frac{J\omega^2}{2}, \tag{4.63}$$

with $\mathbf{M} = J\boldsymbol{\omega}$ and $v = |\mathbf{v}|$, $\omega = |\boldsymbol{\omega}|$ represent the magnitudes of the translational and angular velocities, respectively. The rotational moment of inertia J is of the order $\mathrm{O}(ma^2)$, where a is the size of the molecule. The scale of $\boldsymbol{\omega}$ can be obtained from the above relation to be $\mathrm{O}(v/a)$. The total angular momentum $\mathbf{K}$ can be written as

$$\mathbf{K} = m\left(\mathbf{x} \times \mathbf{v}\right) + \mathbf{M}. \tag{4.64}$$

The scale of $\mathbf{M} = J\boldsymbol{\omega}$ can be obtained from the scales of J and $\boldsymbol{\omega}$ to be $\mathrm{O}(mva)$. The quantity $m(\mathbf{x} \times \mathbf{v})$ is of the order $\mathrm{O}(mvL)$, where L is the macroscopic length scale. It can be seen that the intrinsic rotational angular momentum is $\mathrm{O}(a/L)$ times smaller than the angular momentum due to the motion of the centre of mass, and thus, its contribution to the total angular momentum can be neglected. It should be noted that the size of the molecule a is still much smaller than the mean free path λ for dilute gases. Hence, this analysis still holds even for cases where the mean free path becomes comparable to the macroscopic length scales L.

- **H–Theorem**: For polyatomic gases, a part of entropy production should be due to rotational degrees of freedom. In the current model, as internal degrees of freedom are accounted for in a mean-field manner, similar to the Enskog equation one would expect that entropy contribution should only depend on rotational energy [111]. Thus, we write generalized H–function for polyatomic gas H_1 in Sackur–Tetrode form as a sum of Boltzmann part for monoatomic contribution and rotational part $k\rho \ln \theta_R$ [65]

$$H_1 = H + k\rho \ln \theta_R, \tag{4.65}$$

with k being an unknown scale factor to be fixed later. On multiplying Eq.(4.58) with $\ln f$, and integrating over the velocity space we obtain the evolution of H as

$$\partial_t H + \partial_\alpha J^H_\alpha = \Sigma^{\mathrm{ESBGK}} + \frac{\tau}{\tau_1}\Sigma^{\mathrm{BGK}}\left(f^{\mathrm{MB}}(\rho, \boldsymbol{u}, \theta)\right) - \frac{3\rho}{2\tau_1}\frac{\theta - \theta_T}{\theta}, \tag{4.66}$$

where J^H_α is related to the entropy flux with $\Sigma^{\mathrm{ESBGK}}, \Sigma^{\mathrm{BGK}}$ being the entropy production due to the ES–BGK and the BGK terms respectively. The evolution of the rotational energy (second equation in Eq.(4.58)) can be rewritten as

$$\partial_t \ln \theta_R + u_\alpha \partial_\alpha \ln \theta_R + \frac{2}{\delta \rho \theta_R}\partial_\alpha q^R_\alpha = \frac{\theta - \theta_R}{\tau_1 \theta_R}. \tag{4.67}$$

Multiplying the above equation with ρ and exploiting continuity we obtain

$$\partial_t (\rho \ln \theta_R) + \partial_\alpha \left(\rho u_\alpha \ln \theta_R + \frac{2}{\delta}\frac{q^R_\alpha}{\theta_R}\right) = \frac{\rho}{\tau_1}\frac{\theta - \theta_R}{\theta_R} - \frac{2}{\delta}\frac{q^R_\alpha}{\theta_R^2}\partial_\alpha \theta_R. \tag{4.68}$$

Thereby, adding Eq.(4.66) and Eq.(4.68) and using the form of q^R_α from Eq.(4.59) the evolution of H_1 is obtained as

$$\partial_t H_1 + \partial_\alpha \left(J^H_\alpha + k\rho u_\alpha \ln \theta_R + k\frac{2}{\delta}\frac{q^R_\alpha}{\theta_R} \right) = \Sigma^{\text{ESBGK}} + \Sigma^{\text{BGK}} + \hat{\Sigma}, \tag{4.69}$$

where the right hand side is the net entropy production with contributions from the ES–BGK collision, the BGK collision, and the rotational component of the model. Here,

$$\hat{\Sigma} = -\frac{3\rho}{2\tau_1}\frac{\theta-\theta_T}{\theta} + \frac{k\rho}{\tau_1}\frac{\theta-\theta_R}{\theta_R} + k\frac{2}{\delta}\kappa_R\left(\frac{\partial_\alpha\theta_R}{\theta_R}\right)^2. \tag{4.70}$$

Similar to the standard BGK or ES–BGK case [6], the entropy production $\hat{\Sigma}$ in this model is non-positive too. This is achieved by choosing $k = -\delta/2$ and exploiting the relation Eq.(4.3) to rewrite $\hat{\Sigma}$ as

$$\hat{\Sigma} = -\frac{\delta}{2}\frac{\rho}{\tau_1}\frac{(\theta-\theta_R)^2}{\theta\theta_R} - \kappa_R\left(\frac{\partial_\alpha\theta_R}{\theta_R}\right)^2 \le 0. \tag{4.71}$$

Hence, the proposed model satisfies the H theorem.

- **Hydrodynamics**: In order to derive the hydrodynamic limit and the transport coefficients, the moments are typically categorized into fast M_{fast} and slow moments M_{slow}. The stress tensor and the heat flux constitutes the relevant set of fast moments along with the translational and rotational temperatures as they are not conserved

$$M_{\text{fast}} = \left\{\theta_T, \theta_R, \sigma_{\alpha\beta}, q_\alpha\right\}. \tag{4.72}$$

The base state is obtained from zero of collision from Eq.(4.58) as

$$f = f^{\text{MB}} \implies \theta = \theta_T \quad \text{and} \quad \theta = \theta_R. \tag{4.73}$$

Thus, the fast moment can be expanded around their equilibrium values in a series as

$$M_{\text{fast}} = M_{\text{fast}}\left(f^{\text{MB}}\right) + \tau M^{(1)}_{\text{fast}} + \cdots. \tag{4.74}$$

In Chapman–Enskog expansion, the time derivative of any quantity ϕ is expanded as

$$\partial_t \phi = \partial_t^{(0)} \phi + \tau \partial_t^{(1)} \phi + \mathscr{O}(\tau^2). \tag{4.75}$$

The set of conservation laws (Eqs.(4.62)) upon substituting the expansion of time derivative provide the definition of time derivative at $\mathscr{O}(1)$ of slow variables as Euler equations

$$\begin{aligned} \partial_t^{(0)} \rho + \partial_\alpha (\rho u_\alpha) &= 0, \\ \partial_t^{(0)} (\rho u_\alpha) + \partial_\beta \left(\rho u_\alpha u_\beta + \rho \theta \delta_{\alpha\beta}\right) &= 0, \\ \partial_t^{(0)} E + \partial_\beta \left(E u_\beta + \rho \theta u_\beta\right) &= 0. \end{aligned} \tag{4.76}$$

Thus, pressure evolution at $O(1)$ satisfies the adiabatic condition for a polyatomic gas

$$\left(\partial_t^{(0)} + u_\beta \partial_\beta\right) \left(\frac{p}{\rho^\gamma}\right) = 0, \text{ where } \gamma = \frac{5+\delta}{3+\delta}. \tag{4.77}$$

Similarly, at order $\mathscr{O}(\tau)$ we have

$$\begin{aligned} \partial_t^{(1)} \rho &= 0, \\ \partial_t^{(1)} (\rho u_\alpha) + \partial_\alpha (\rho \theta_T^{(1)}) + \partial_\beta \sigma_{\alpha\beta}^{(1)} &= 0, \\ \partial_t^{(1)} E + \partial_\beta \left(\sigma_{\alpha\beta}^{(1)} u_\alpha + \rho \theta_T^{(1)} u_\beta + q_\beta^{(1)}\right) &= 0. \end{aligned} \tag{4.78}$$

We derive the evolution equations for kinetic energy, internal energy, pressure, stress, heat flux, translational, and rotational temperatures for the proposed model. Using the momentum evolution equation Eq.(4.62), we obtain the evolution equation for $\rho u_\alpha u_\beta$ as

$$\partial_t \left(\rho u_\alpha u_\beta\right) + \partial_\gamma (\rho u_\alpha u_\beta u_\gamma) + u_\alpha \partial_\gamma (\rho \theta_T \delta_{\beta\gamma} + \sigma_{\beta\gamma}) + u_\beta \partial_\gamma (\rho \theta_T \delta_{\alpha\gamma} + \sigma_{\alpha\gamma}) = 0. \tag{4.79}$$

Evolution of kinetic energy obtained by taking the trace of the above equation is

$$\partial_t \left(\frac{1}{2} \rho u^2\right) + \partial_\gamma \left(\frac{1}{2} \rho u^2 u_\gamma\right) + u_\beta \partial_\gamma (\rho \theta_T \delta_{\beta\gamma} + \sigma_{\beta\gamma}) = 0. \tag{4.80}$$

Subtracting the above equation from the evolution equation of total energy from Eq.(4.62), gives the evolution equation for internal energy $e = (3+\delta)\rho\theta/2$ as

$$\partial_t e + \partial_\beta \left(e u_\beta\right) + \partial_\beta q_\beta + \sigma_{\beta\gamma}\partial_\gamma u_\beta + \rho\theta_T \partial_\gamma u_\gamma = 0, \tag{4.81}$$

and the evolution equation of pressure $p = \rho\theta$ as

$$\partial_t p + \partial_\beta \left(p u_\beta\right) + \left(\frac{2}{3+\delta}\right)\left(\partial_\beta q_\beta + \sigma_{\beta\gamma}\partial_\gamma u_\beta + \rho\theta_T \partial_\gamma u_\gamma\right) = 0. \tag{4.82}$$

Using the pressure and continuity equation, the evolution equation for temperature θ is

$$\partial_t \theta + u_\beta \partial_\beta \theta + \left(\frac{2}{(3+\delta)\rho}\right)\left(\partial_\beta q_\beta + \sigma_{\beta\gamma}\partial_\gamma u_\beta + \rho\theta_T \partial_\gamma u_\gamma\right) = 0. \tag{4.83}$$

From the evolution of kinetic energy (Eq.(4.80)) and the translational temperature (Eq.(4.60)), the evolution for translational energy can be evaluated as

$$\partial_t \left(\frac{3\rho\theta_T}{2}\right) + \partial_\beta \left(\frac{3\rho\theta_T}{2} u_\beta\right) + \rho\theta_T \partial_\beta u_\beta + \sigma_{\beta\gamma}\partial_\beta u_\gamma + \partial_\beta q^T_\beta = \frac{\rho}{\tau_1}\left(\frac{3}{2}\theta - \frac{3}{2}\theta_T\right). \tag{4.84}$$

Using the continuity equation, the evolution for translational temperature θ_T is

$$\partial_t \theta_T + u_\beta \partial_\beta \theta_T + \frac{2}{3}\theta_T \partial_\beta u_\beta + \frac{2}{3\rho}\sigma_{\beta\gamma}\partial_\beta u_\gamma + \frac{2}{3\rho}\partial_\beta q^T_\beta = \frac{1}{\tau_1}\left(\theta - \theta_T\right). \tag{4.85}$$

For the evolution of the stress tensor $\sigma_{\alpha\beta}$, we multiply the kinetic equation (Eq.(4.58)) with $\xi_\alpha \xi_\beta$ and integrate over the velocity space to obtain

$$\begin{aligned} &\partial_t(\rho\theta_T\delta_{\alpha\beta} + \sigma_{\alpha\beta}) + \partial_\kappa Q^T_{\alpha\beta\kappa} + \partial_\kappa \left(u_\kappa(\rho\theta_T\delta_{\alpha\beta} + \sigma_{\alpha\beta})\right) + (\rho\theta_T\delta_{\kappa\beta} + \sigma_{\kappa\beta})\partial_\kappa u_\alpha \\ &+ (\rho\theta_T\delta_{\kappa\alpha} + \sigma_{\kappa\alpha})\partial_\kappa u_\beta = \frac{1}{\tau}(b-1)\,\sigma_{\alpha\beta} + \frac{1}{\tau_1}\left(\rho\theta\delta_{\alpha\beta} - \rho\theta_T\delta_{\alpha\beta} - \sigma_{\alpha\beta}\right). \end{aligned} \tag{4.86}$$

Thereafter, multiplying Eq.(4.84) with $\delta_{\alpha\beta}$ and subtracting from the above equation one obtains evolution of stress tensor as

$$\partial_t(\sigma_{\alpha\beta})+\partial_\gamma\left(u_\gamma\sigma_{\alpha\beta}\right)+\partial_\gamma\overline{Q^T_{\alpha\beta\gamma}}+\frac{4}{5}\overline{\partial_\beta q^T_\alpha}+2\rho\theta_T\overline{\partial_\beta u_\alpha}+2\overline{\partial_\gamma u_\alpha\sigma_{\gamma\beta}}=\left(\frac{1}{\tau}(b-1)-\frac{1}{\tau_1}\right)\sigma_{\alpha\beta}. \tag{4.87}$$

Similarly, the evolution equation for translational heat flux is obtained by multiplying the kinetic equation (Eq.(4.58)) with $\xi^2\xi_\alpha$ to obtain

$$\begin{aligned}&\partial_t q^T_\alpha+\partial_\beta\left(u_\beta q^T_\alpha\right)+\overline{Q^T_{\alpha\beta\gamma}}\partial_\beta u_\gamma+\frac{1}{2}\partial_\beta R_{\alpha\beta}+\frac{7}{5}q^T_\beta\partial_\beta u_\alpha+\frac{2}{5}q^T_\alpha\partial_\eta u_\eta+\frac{2}{5}q^T_\beta\partial_\alpha u_\beta\\&-\frac{5}{2}\theta_T\partial_\alpha(\rho\theta_T)-\frac{\sigma_{\alpha\beta}}{\rho}\partial_\beta(\rho\theta_T)-\frac{5}{2}\theta_T\partial_\kappa\sigma_{\kappa\alpha}-\frac{\sigma_{\alpha\beta}}{\rho}\partial_\kappa\sigma_{\kappa\beta}=-\left(\frac{1}{\tau}+\frac{1}{\tau_1}\right)q^T_\alpha.\end{aligned} \tag{4.88}$$

The expressions for $\rho\theta_T^{(1)}$ and $\sigma^{(1)}_{\alpha\beta}$ can be obtained from the evolution equations of translational temperature and stress tensor respectively as

$$\rho\theta_T^{(1)}=-\frac{2\delta}{3(3+\delta)}\frac{\tau_1}{\tau}p\partial_\gamma u_\gamma,\quad \sigma^{(1)}_{\alpha\beta}=-\frac{2p\overline{\partial_\beta u_\alpha}}{B-b}, \tag{4.89}$$

where $B=1+\tau/\tau_1$. Substituting the above expressions in momentum conservation equation, $O(\tau)$ hydrodynamics with shear viscosity η and bulk viscosity η_b is

$$\eta=\frac{p\tau}{B-b},\quad \text{and}\quad \eta_b=\frac{2\delta}{3(3+\delta)}p\tau_1. \tag{4.90}$$

Similarly, translational thermal conductivity for the model is obtained from the translational heat flux evolution (Eq.(4.88)). A Chapman–Enskog expansion of Eq.(4.88) by substituting $q^T_\alpha=(q^T_\alpha)^{\text{MB}}+\tau(q^T_\alpha)^{(1)}+\mathscr{O}(\tau^2)$ at $\mathscr{O}(1)$ yields

$$\left(1+\frac{\tau}{\tau_1}\right)(q^T_\alpha)^{(1)}=-\frac{5}{2}\rho\theta\partial_\alpha\theta. \tag{4.91}$$

Thus, the translational thermal conductivity is $\kappa_T=5p\tau/(2B)$ which means the total thermal conductivity $\kappa=\kappa_T+\kappa_R$ with $k_r=\kappa_R/\kappa_T$ is $\kappa=5p\tau/(2B)(1+k_r)$. Hence,

$$\text{Pr}=\frac{\eta C_p}{\kappa}=\left(\frac{B}{B-b}\right)\left(1+\frac{\delta}{5}\right)\left(\frac{1}{1+k_r}\right). \tag{4.92}$$

To summarize, the parameter δ is determined directly from specific heat ratio γ. While the rotational relaxation time τ_1 is fixed based on δ and bulk viscosity η_b. The translational relaxation time τ is then determined based on δ, shear viscosity η, and τ_1. The parameter b is then fixed using τ, τ_1, Pr, and k_r thereby imposing the target Prandtl number.

4.6 Discretizing via lattice Boltzmann Method

In this section, we formulate a lattice Boltzmann scheme for solving the proposed model. We employ the RD3Q41 model proposed in Chapter 2.

The kinetic equation (Eq.(4.58)) in discrete in velocity space for populations f_{1i} is

$$\partial_t f_{1i}(\boldsymbol{x},\boldsymbol{c},t)+c_\alpha\partial_\alpha f_{1i}(\boldsymbol{x},\boldsymbol{c},t)=\Omega_i(\boldsymbol{x},t), \tag{4.93}$$

where

$$\Omega_i(\boldsymbol{x},t)=\frac{1}{\tau}\left[f_{1i}^{\mathrm{ES}}(\rho,\boldsymbol{u},\theta_T\delta_{\alpha\beta}+b\sigma_{\alpha\beta})-f_{1i}\right]+\frac{1}{\tau_1}\left[f_{1i}^{\mathrm{Eq}}(\rho,\boldsymbol{u},\theta)-f_{1i}\right], \tag{4.94}$$

with moments of the discrete populations f_{1i} defined as

$$\rho(f_1)=\sum_i f_{1i},\ \ \rho u_\alpha(f_1)=\sum_i f_{1i}c_{i\alpha},\quad \theta_T(f_1)=\frac{1}{3\rho(f_1)}\left(\sum_i f_{1i}c_i^2-\rho\mathbf{u}^2\right). \tag{4.95}$$

To have a numerically efficient scheme for the N coupled partial differential equations of Eq.(4.93), it is desirable to have large time steps, i.e., $\Delta t \gg \tau$. Upon integrating Eq.(4.93) along the characteristics and approximating the integral related to collision term via trapezoid rule, we obtain the implicit relation

$$f_{1i}(\boldsymbol{x}+\boldsymbol{c}\Delta t,t+\Delta t)=f_{1i}(\boldsymbol{x},t)+\frac{\Delta t}{2}\left[\Omega_i(\boldsymbol{x},t)+\Omega_i(\boldsymbol{x}+\boldsymbol{c}t,t+\Delta t)\right], \tag{4.96}$$

which is made explicit by a transformation to an auxiliary population $g_{1i}(\boldsymbol{x},\boldsymbol{c},t)=f_{1i}(\boldsymbol{x},\boldsymbol{c},t)-(\Delta t/2)\Omega_i(\boldsymbol{x},\boldsymbol{c},t)$. This implies the evolution equation for g_{1i} is

$$g_{1i}(\boldsymbol{x}+\mathbf{c}_i\Delta t,t+\Delta t)=g_{1i}(\boldsymbol{x},t)(1-2\beta^*)+2\tau^*\beta^*\Omega_i(\boldsymbol{x},\boldsymbol{c},t), \tag{4.97}$$

with $1/\tau^* = 1/\tau + 1/\tau_1$ and $\beta^* = \Delta t/(2\tau^* + \Delta t)$. The moments of the auxiliary distribution g_1 are related to the moments of discrete populations f_1 as

$$\begin{aligned} &\rho(g_1) = \rho(f_1),\ \mathbf{u}(g_1) = \mathbf{u}(f_1),\ \theta_T(g_1) = \theta_T(f_1) + \frac{\delta \Delta t}{2\tau_1(3+\delta)} \left(\theta_T(f_1) - \theta_R\right), \\ &\sigma_{\alpha\beta}(g_1) = \sigma_{\alpha\beta}(f_1) \left(1 + \frac{\Delta t}{2\tau^*} - \frac{\Delta t}{2\tau} b\right). \end{aligned} \tag{4.98}$$

To solve the second part of Eq.(4.58) that represents the internal energy, we write

$$\frac{\partial \theta_{\mathrm{R}}}{\partial t} + u_\alpha \frac{\partial \theta_{\mathrm{R}}}{\partial x_\alpha} = \frac{1}{\tau_1} \left(\theta - \theta_{\mathrm{R}}\right) + \frac{2}{\rho \delta} \kappa_R \nabla^2 \theta_{\mathrm{R}}, \tag{4.99}$$

by exploiting the Eqs. (4.3), (4.59), and the continuity equation. The above equation is an advection-relaxation-diffusion equation that is solved by the steps detailed below:

1. The relaxation equation
$$\frac{\partial \theta_{\mathrm{R}}}{\partial t} = \frac{1}{\tau_1} \left(\theta - \theta_{\mathrm{R}}\right), \tag{4.100}$$
is first solved using the backward Euler method for a half-time step along with the relation in Eq. (4.3) to obtain
$$\theta_{\mathrm{R}}^{t+\Delta t/2} = \frac{1}{1+X} \theta_{\mathrm{R}}^{t} + \frac{X}{1+X} \theta_T(f_1), \tag{4.101}$$
where $X = 3\Delta t/(2\tau_1(3+\delta))$.

2. The MacCormack scheme [92], which uses forward and backward differences for spatial derivatives in the predictor and corrector steps respectively, is used to solve the advection equation
$$\frac{\partial \theta_{\mathrm{R}}}{\partial t} + u_\alpha \frac{\partial \theta_{\mathrm{R}}}{\partial x_\alpha} = 0. \tag{4.102}$$

3. The diffusion equation
$$\frac{\partial \theta_{\mathrm{R}}}{\partial t} = \frac{2}{\rho \delta} \kappa_R \nabla^2 \theta_{\mathrm{R}}, \tag{4.103}$$
is then solved using the standard forward time centered space (FTCS) scheme to get $\theta_{\mathrm{R}}^{\mathrm{dif}}$.

4. Finally, the second part of relaxation is completed by an advance of $\theta_{\mathrm{R}}^{\mathrm{dif}}$ by another half time-step $\Delta t/2$ leading to the final solution at $t + \Delta t$ as
$$\theta_{\mathrm{R}}^{\mathrm{t+\Delta t}} = \frac{1}{1+X} \theta_{\mathrm{R}}^{\mathrm{dif}} + \frac{X}{1+X} \theta_T(f_1). \tag{4.104}$$

Note that the choice of the solver for the evolution equation of rotational energy is independent of the lattice Boltzmann solver used for solving f_1. The use of a scalar equation for rotational energy offers a significant computational advantage over using an additional distribution function, with memory usage and computational time reduced by a factor of 3-4. The difference between the two approaches lies in the treatment of internal degrees of freedom, but the accuracy remains the same for both formulations when the same flow solver is used (for low Knudsen problems). The computational cost savings are entirely due to using a scalar variable instead of a full distribution function.

In contrast, solving kinetic equations with a $D3Q15$ velocity model requires at least five times more storage than advection-diffusion-reaction solvers, which typically work with 2-3 variables per grid point. We remind that both kinetic equation and advection-diffusion solvers are memory-bound, hence, the cost of floating point variables does not have a significant impact on the computational cost of either method. Instead, the number of memory read and write operations determines the computational cost.

A 15 velocity lattice Boltzmann model, for instance, requires 30 memory read/write operations per grid point for advection, and another 30 memory read/write operations and approximately 100 FLOP per grid point for the collision step. Thus, a simulation of the second kinetic equation requires 60 memory read/write operations and around 100 FLOP per grid point. Since most stencil-based finite difference type codes, including lattice Boltzmann codes, are memory-bound due to slower memory access in modern computers, the proposed model with advection-diffusion-relaxation would require only about 20-24 reads and writes per grid point. This leads to a 3-4 times reduction in computational time when using a scalar equation compared to a D3Q15 stencil.

In the next section, we validate the proposed numerical model by simulating a few benchmark problems related to acoustics, hydrodynamics, and heat transfer such as propagation of an acoustic pulse, startup of a simple shear flow, thermal conduction, and viscous heat dissipation.

4.7 Validation

In this section, we validate the model by contrasting simulation result with various benchmark results. As a first example, we consider a periodic domain $[-\pi, \pi]$ with $128 \times 4 \times 4$ lattice points to verify numerical sound speed. We initialize the domain with a pressure fluctuation of

Table 4.1 Specific heat ratios of real fluids [58] and their effective rotational degrees of freedom.

Fluid	γ	Effective-δ
Argon, Helium	1.66	0.03
Air	1.403	1.96
Nitrogen	1.404	1.95
Steam	1.33	3.06
Methane	1.31	3.45
Ethane	1.22	6.09
Ethyl alcohol	1.13	12.38
Benzene	1.1	17
n-Pentane	1.086	20.26
Hexane	1.08	22
Methylal	1.06	30.33

the form $p(x,t=0) = p_0(1+\varepsilon\cos(x))$ with $p_0 = \theta_0$. The pressure pulse is expected to reach the same state as the initial condition after one acoustic time period (t_a). The L_2-norm of the pressure fluctuation is computed using the current state and initial state which is expected to be minimum when the waves are in-phase. The number of time-steps taken to achieve the least L_2-norm is used to compute t_a and the speed of sound as $c_s = L/t_a$ where L is the domain length. The $\gamma = c_s^2/\theta_0$ is thus computed from the speed of sound and the lattice temperature. Here, we demonstrate the versatility of the model by simulating several real fluids by imposing the effective rotational degrees of freedom δ as given in Table 4.1. We show in Figure 4.1 that our model accurately recovers the specific heat ratio for various polyatomic gases, even for fractional (effective) rotational degrees of freedom. The proposed model remains accurate even for fractional rotational degrees of freedom, thereby achieving any target specific heat ratio values. In Figure 4.2, we perform a grid convergence study for air and observe a second order convergence. We perform additional validation studies by restricting our attention to diatomic gases with variable Prandtl number.

Next, we study the absorption of sound in a dissipative compressible medium. The presence of both viscosity and thermal conductivity leads to the dissipation of energy in the sound waves. For an emitted wave, the pressure perturbations p' far away from the source decays during a finite time is [81]

$$p'(r,t) \propto (\mathrm{La}\, rL)^{-1/2} \exp\left(-\frac{(r-c_s t)^2}{2\mathrm{La}\, rL}\right), \tag{4.105}$$

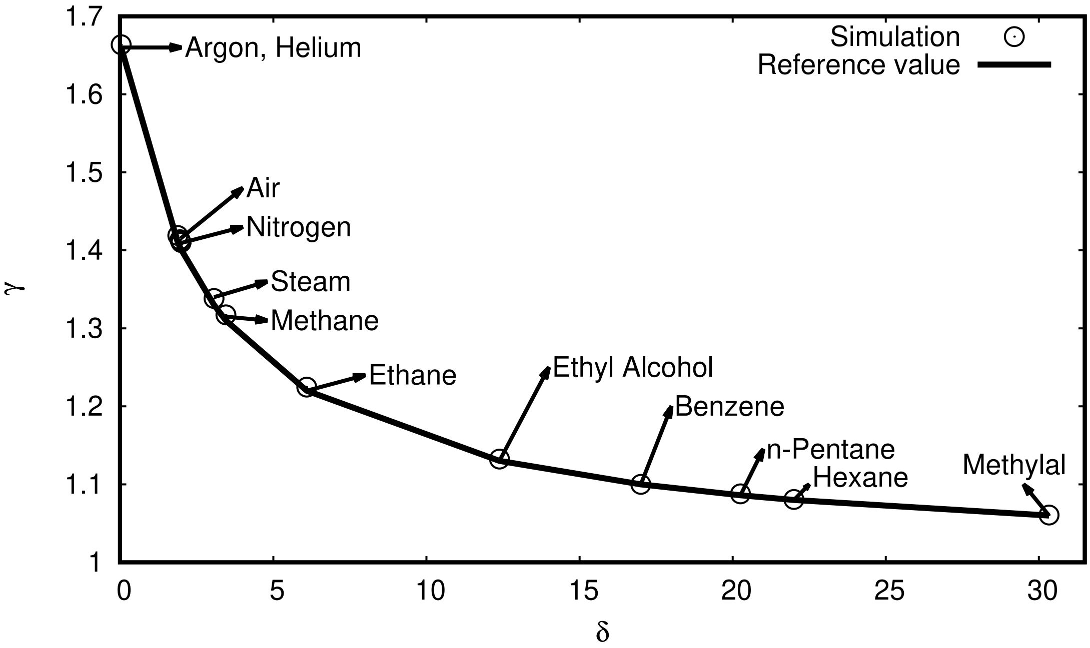

Fig. 4.1 Specific heat ratio in simulating sound propagation in different gases. The line represents the reference value with δ the number of effective rotational degrees of freedom for various gases as listed in Table 4.1

.

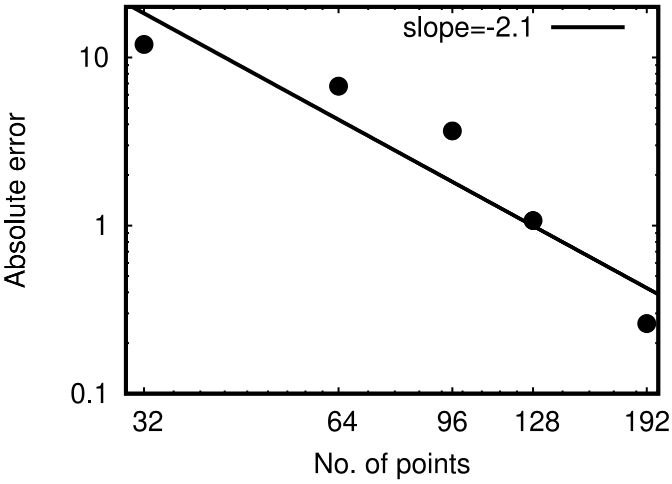

Fig. 4.2 Grid convergence study showing a second order convergence for air.

.

Table 4.2 Variation of Landu Number La (Eq. 4.106) with Pr at Kn $= 10^{-3}$.

Pr	La
1.4	2.3302×10^{-3}
2.0	2.0311×10^{-3}
5.0	1.6124×10^{-3}
10.0	1.4729×10^{-3}

where the dimensionless Landau number La is [13]

$$\mathrm{La} = \mathrm{Kn}\left(\frac{4}{3}+\lambda\right)+\frac{\mathrm{Kn}}{\mathrm{Pr}}(\gamma-1). \tag{4.106}$$

Here, λ is the ratio of bulk to shear viscosities and Kn is the Knudsen number. The form of pressure perturbation shows that the wave profile is Gaussian-like at large distances and the width of the wave is proportional to $\sqrt{\mathrm{La}}$ for a fixed domain length L.

To demonstrate the effectiveness of the LB scheme, we perform a simulation at a fixed Kn value of 10^{-3} on a domain of size 400×400 at Prandtl numbers 1.4, 2, 5, and 10. We initialize the domain with a normal density perturbation of amplitude 0.001 at the center of the fluid of uniform density 1 at rest. From Eq.(4.90) and setting $\tau = (3/5)\tau_1$ one obtains $\lambda = 224/(225\,\mathrm{Pr})$.

Using this above relation and $\gamma = 7/5$ the Landau number La is calculated as

$$\mathrm{La} = \mathrm{Kn}\left(\frac{4}{3}+\frac{314}{225}\frac{1}{\mathrm{Pr}}\right). \tag{4.107}$$

The Landau numbers for the chosen set of parameters are listed in Table 4.2. It is evident that La is a linear function of $1/\mathrm{Pr}$ which suggests that the width of the Gaussian increases with a decrease in Pr number. The pressure fluctuations far from the source of perturbation after $t = 0.2t_a$ for various Prandtl numbers are plotted in Figure 4.3, where $t_a = L/c_s$ is the acoustic time scale. It is evident that as expected the width of the wave decreases with an increase in the Prandtl number.

Next, we investigate the propagation of an acoustic pulse in a diatomic gas with $\gamma = 7/5$ where the isentropic speed of sound is $c_s = \sqrt{\gamma\theta}$. An axisymmetric pressure pulse is initialized at the centre of a domain of size $[-1,1]$ with $256\times256\times4$ grid points. The acoustic pulse is of the form

$$p(x,y,t=0) = p_0\left(1+\varepsilon e^{-\alpha r^2}\right), \tag{4.108}$$

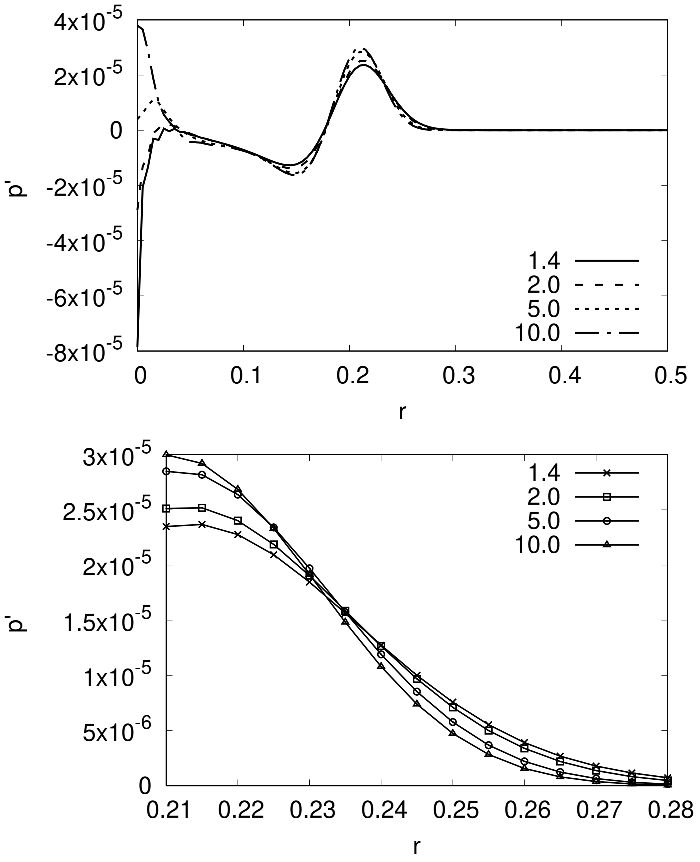

Fig. 4.3 Pressure perturbations versus Pr (zoomed in the bottom plot): the width of the Gaussian wave increases with a decrease in Pr.

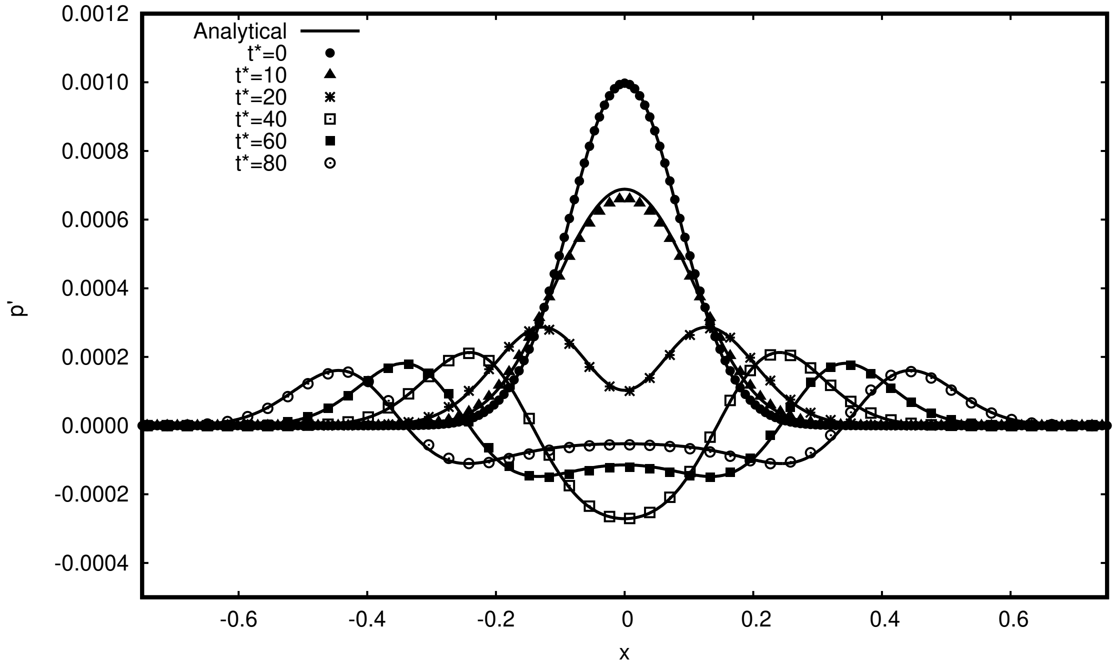

Fig. 4.4 Comparison of the pressure fluctuation along the centerline at time t^* from LB simulation(points) and exact solution(line).

with $p_0 = \theta_0$, $\varepsilon = 0.001$, $b = 0.1$, $\alpha = \ln(2)/b^2$, and $r = \sqrt{x^2+y^2}$. For low amplitudes of pressure fluctuations and low viscosity, the exact form of the pressure fluctuation is known as the solution of the linearized Euler equations as [131]

$$p'(x,y,t) = p_0 \times \frac{\varepsilon}{2\alpha}\int_0^\infty \exp\left(\frac{-\xi^2}{4\alpha}\right)\cos(c_s\xi t)J_0(\xi r)\xi \, d\xi, \tag{4.109}$$

where J_0 is the Bessel function of the first kind of zero-order [1]. Figure. 4.4 shows that the pressure fluctuations from the simulation and the exact solution along the centerline of y-axis are in agreement.

Next, we simulate the transient hydrodynamics in the startup of a simple shear flow between two flat plates separated by a distance L on a grid of size $128 \times 64 \times 8$ with diffusive wall boundary condition [9] and periodicity in the other two directions. Here, the top plate is suddenly started with a velocity u_w while the bottom plate remains stationary. The viscous effects play an important role in the development of the flow which is driven by momentum diffusion. Figure 4.5 contrasts the solutions at various diffusion times $t^* = t/(L^2/\nu)$ obtained from our simulations with the known analytical solution for the velocity [106]

$$u^* = \frac{u}{u_w} = \frac{y}{L} - \frac{2}{\pi}\sum_{k=1}^{\infty}\left[\frac{1}{k}\exp\left(-k^2\pi^2\frac{\nu t}{L^2}\right)\sin\left(k\pi\left(1-\frac{y}{L}\right)\right)\right]. \tag{4.110}$$

As expected, the simulation recovers the analytical solution with good accuracy.

Next, we investigate the effects of thermal conduction by considering a setup consisting of fluid confined in a square cavity of size $[L,L]$ with 128×128 points and stationary walls. The top wall maintained at a higher temperature T_1, while the other three walls are maintained at a temperature $T_0(< T_1)$. Diffusive wall boundary conditions are applied in both directions. The analytical solution for the temperature profile at steady state is [85]

$$\frac{T-T_0}{T_1-T_0} = \frac{2}{\pi}\sum_{n=1}^{\infty}\frac{(-1)^{n+1}+1}{n}\sin\left(n\pi x\right)\frac{\sinh(n\pi y)}{\sinh(n\pi)}. \tag{4.111}$$

Figure 4.6 shows that the simulated temperature profiles along lines $x = 0.1L,\ 0.2L$, and $0.5L$ and along $y = 0.25L,\ 0.5L$, and $0.75L$ for a temperature difference of $0.1\theta_0$ matches well with the analytical solution.

Next, we validate our model for a thermal Couette flow problem to evaluate its capability in simulating viscous heat dissipation at various Prandtl numbers. We study the steady-state of a flow induced by a wall at $y = H$ moving with a constant horizontal velocity U_0 and maintained at a constant elevated temperature T_1. The lower wall at $y = 0$ is kept stationary at a constant temperature T_0 ($T_1 > T_0$). The analytical solution for the temperature profile for this setup is [24]

$$\frac{T-T_0}{\Delta T} = \frac{y}{H} + \frac{\mathrm{Pr\,Ec}}{2}\frac{y}{H}\left(1-\frac{y}{H}\right), \tag{4.112}$$

where $\Delta T = T_1 - T_0$ is the temperature difference between the two walls and $\mathrm{Ec} = U_0^2/(c_p\Delta T)$ is the Eckert number that represents the ratio of viscous dissipation to heat conduction with $c_p = 7/2$ as the specific heat at constant pressure for a diatomic gas.

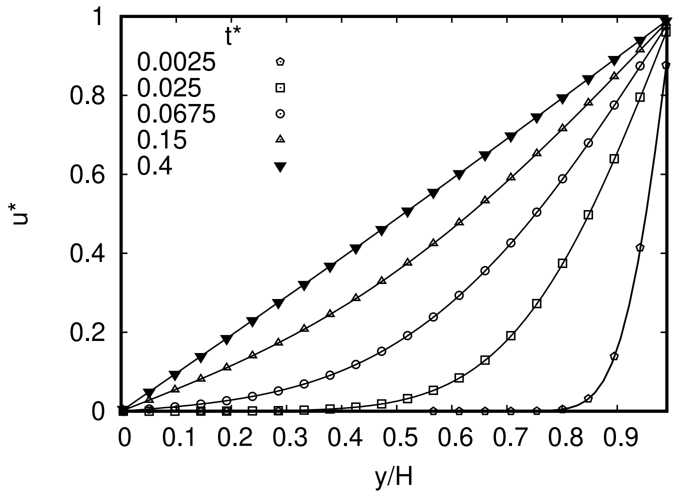

Fig. 4.5 Transients in a planar Couette flow

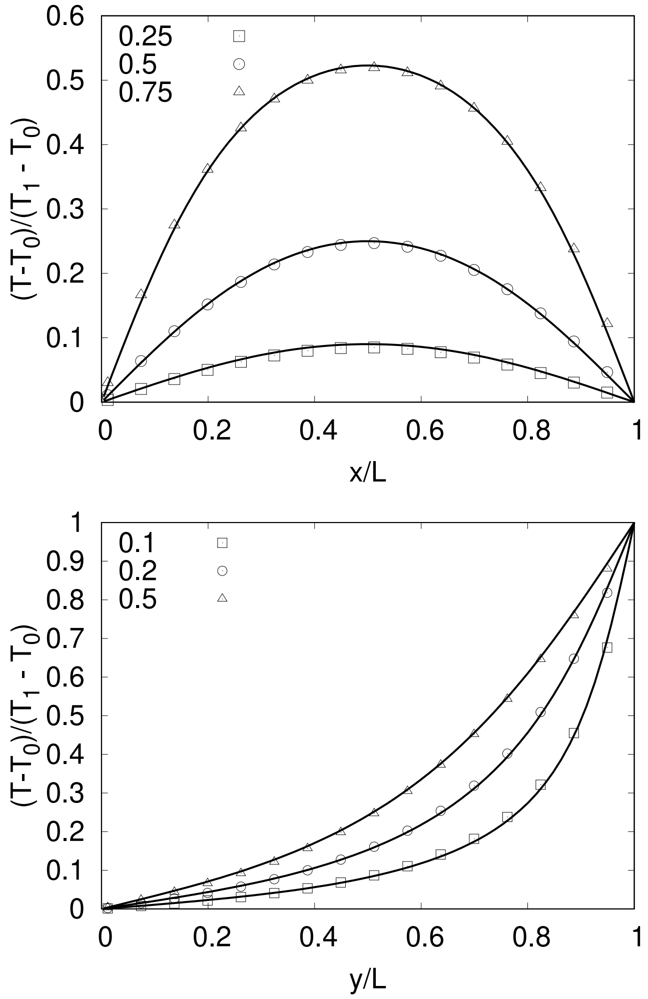

Fig. 4.6 Temperature profiles at $y = 0.25L,\ 0.5L$, and $0.75L$ (left) and at $x = 0.1L,\ 0.2L$, and $0.5L$ (right) in a 2D heated cavity.

Simulations were performed for $\mathrm{Pr} = 0.75,\ 2.5,\ 5.0,\ 7.5$, and 10 at Eckert number fixed at unity on a domain with 128 grid points. The walls were maintained at temperatures $\theta_0 + 0.5\Delta\theta$ and $\theta_0 - 0.5\Delta\theta$ and plate velocity U_0 is chosen corresponding to a Mach number of 0.1. Figure 4.7 compares the temperature profiles obtained analytically and via simulations and they are found to be in good agreement.

4.7.1 Transonic flows

A higher-order model capable RD3Q167 of simulating transonic flows is employed [59] for the following validation cases. The energy shells and their corresponding velocities with weights for this RD3Q167 model velocities are given in Table 4.3.

We present a Sod's test problem with a initial density ratio of 8 and pressure ratio of 10 on the left and right halves of the domain

$$\begin{pmatrix}\rho_L\\ u_L\\ p_L\end{pmatrix} = \begin{pmatrix}1\\ 0\\ 1\end{pmatrix},\ \begin{pmatrix}\rho_R\\ u_R\\ p_R\end{pmatrix} = \begin{pmatrix}0.125\\ 0\\ 0.1\end{pmatrix} \tag{4.113}$$

on a grid of size $4096 \times 4 \times 4$ for this test case. In Figure 4.8, we present the density, Mach number and pressure profiles at time=0.1 for specific-heat ratios of helium($\delta = 0.03$), air ($\delta = 1.96$) and methylal($\delta = 30.33$) as given in Table 4.1 and contrast the solution with exact Reimann solution.

To demonstrate the capability of the proposed model to simulate complex flows, we show a qualitative simuation of flow past a circular cylinder at a Reynolds number of 5000 defined based on diameter and free-stream velocity. The specific-heat ratio for this simulation was chosen to be 1.22 with additional rotational degrees of freedom $\delta = 6$. The Mach number for the present simulation is fixed at 0.45 with the 40 lattice points per diameter. We show the vorticity profile around the cylinder after 10 convection times in Figure 4.9. It should be noted that the proposed formulation is quite stable even for such a severely under-resolved simulation. The noise around the cylinder is a direct result of under-resolution, which limits the simulation's ability to capture finer flow details.

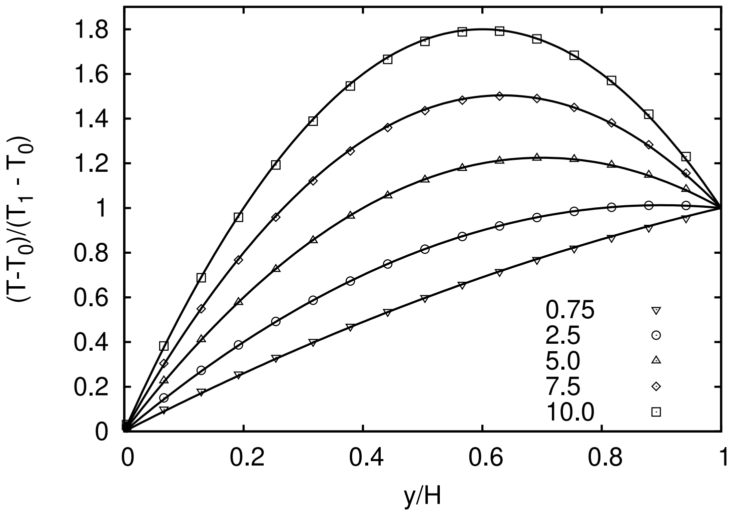

Fig. 4.7 Temperature profiles at steady state (symbols) compared to the analytical solution (lines) at varying Prandtl numbers.

Table 4.3 Velocities and their corresponding weights for the RD3Q167 model with $\theta_0 = 0.7374708021487686$.

Discrete Velocities(c_i)	Weight(w_i)
$(0,0,0)$	0.0296445287398454
$(\pm 1,0,0),(0,\pm 1,0),(0,0,\pm 1)$	0.011144397119839009
$(\pm 2,0,0),(0,\pm 2,0),(0,0,\pm 2)$	0.000992582094090251
$(\pm 3,0,0),(0,\pm 3,0),(0,0,\pm 3)$	0.00043229649222277557
$(\pm 1,\pm 1,0),(\pm 1,0,\pm 1),(0,\pm 1,\pm 1)$	0.0078020595256513905
$(\pm 2,\pm 2,0),(\pm 2,0,\pm 2),(0,\pm 2,\pm 2)$	0.0008848260211852592
$(\pm 3,\pm 3,0),(\pm 3,0,\pm 3),(0,\pm 3,\pm 3)$	6.6974998420071616e-6
$(\pm 2,\pm 1,0),(\pm 2,0,\pm 1),(0,\pm 2,\pm 1),$ $(\pm 1,\pm 2,0),(\pm 1,0,\pm 2),(0,\pm 1,\pm 2)$	0.004147252375006042
$(\pm 0.5,\pm 0.5,\pm 0.5)$	0.044780123964114515
$(\pm 1,\pm 1,\pm 1)$	0.007147942701081054
$(\pm 1.5,\pm 1.5,\pm 1.5)$	0.0026467301988094528
$(\pm 2,\pm 2,\pm 2)$	0.000012175651763644929
$(\pm 2.5,\pm 2.5,\pm 2.5)$	4.816438635687508e-6
$(\pm 1.5,\pm 0.5,\pm 0.5),(\pm 0.5,\pm 1.5,\pm 0.5),(\pm 0.5,\pm 0.5,\pm 1.5)$	0.01038287235627671
$(\pm 3,\pm 1,\pm 1),(\pm 1,\pm 3,\pm 1),(\pm 1,\pm 1,\pm 3)$	0.00021497980321030788

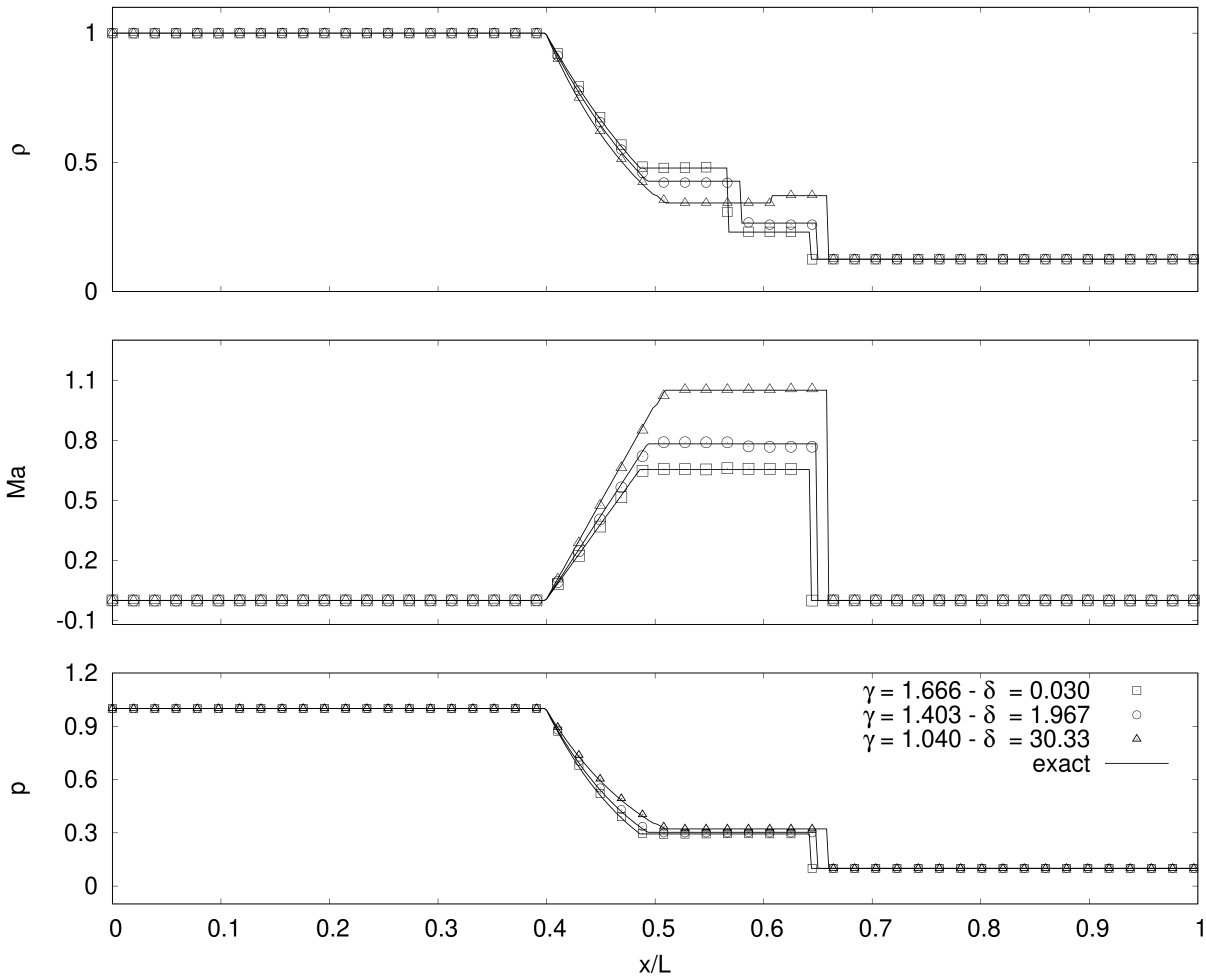

Fig. 4.8 Density, Mach number and pressure after time=0.1 for Sod's test problem

.

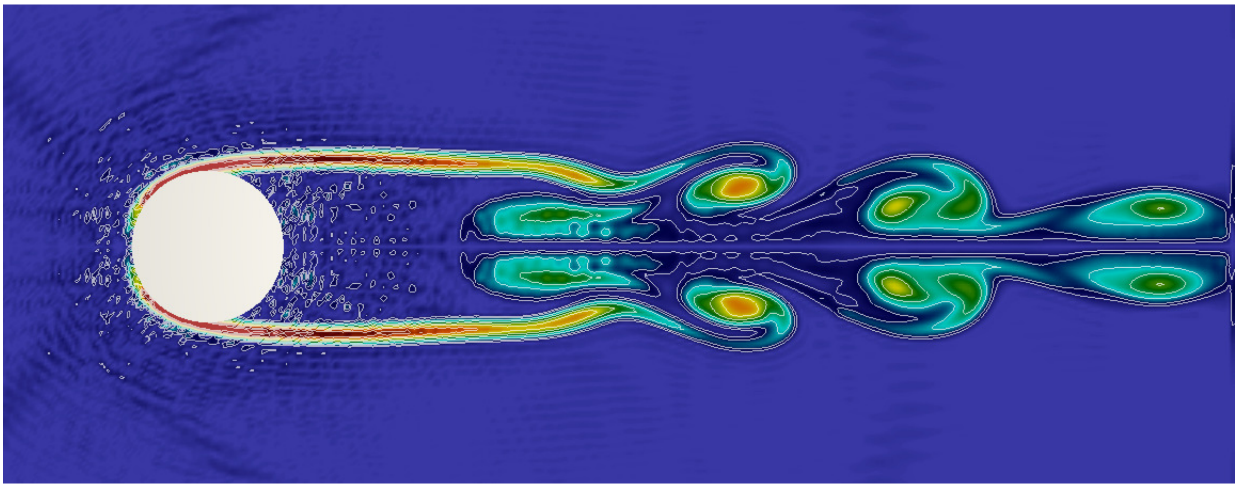

Fig. 4.9 Vorticity profile around the circular cylinder after 10 convection times.

4.8 Conclusion

We have proposed a kinetic model for polyatomic gases with a tunable Prandtl number, by augmenting the ES–BGK model, an extension of the BGK model, at the level of the single-particle distribution function with an advection-diffusion-relaxation equation for the rotational energy.

The kinetic equation of the unified model along with the evolution equation for the rotational energy is

$$\begin{aligned} \partial_t f_1 + c_\alpha \partial_\alpha f_1 &= \frac{1}{\tau}\left(f^{\mathrm{ES}}(\rho, \boldsymbol{u}, \theta_T \delta_{\alpha\beta} + b\sigma_{\alpha\beta}) - f_1\right) + \frac{1}{\tau_1}\left(f^{\mathrm{MB}}(\rho, \boldsymbol{u}, \theta) - f_1\right), \\ \partial_t\left(E_R\right) + \partial_\alpha\left(E_R u_\alpha + q^R_\alpha\right) &= \frac{1}{\tau_1}\left(\frac{\delta}{2}\rho\theta - E_R\right), \end{aligned} \tag{4.114}$$

with the form of heat flux due to internal degrees of freedom as

$$q^R_\alpha = -\kappa_R \partial_\alpha \theta_R. \tag{4.115}$$

We show that close to the hydrodynamic limit, the internal degrees of freedom tend to be well represented just by rotational kinetic energy density and the proposed model recovers the compressible hydrodynamic equations of polyatomic gases as its macroscopic limit. It was shown that the transport coefficients of the model can be tuned for simulation of flows at different Prandtl numbers and specific heat ratios. A set of free parameters such as number of rotational degrees of freedom, translation relaxation time, rotational relaxation time, rotational thermal conductivity, and a free parameter b in the ES–BGK model can be used to tune the specific heat ratio, shear viscosity, bulk viscosity and set a target Prandtl number. This framework is general enough to deal with a more complex model of internal structures. We also demonstrated that the model respects the H theorem. The simplicity of the model makes it suitable for LB and other numerical implementations.

Chapter 5

Integration of stiff equations

5.1 Introduction

Physical systems encountered in natural sciences are often multiscale in nature as the phenomena of interest occur over a disparate range of space and time scales [27, 47]. This happens as several physical mechanisms are present in the system, each acting at a particular time scale. For example, in reactive systems such as combustion, chemical kinetics rate equations frequently involve intermediate reactions happening at much shorter time scales where a few system components go rapidly to equilibrium [55, 141]. Typically, we are only interested in long-term behavior of these systems. However, these large-scale effects are significantly modified in general by phenomena happening at a short time scale. Thus, one needs to compute the effect of the fast-scale motions on the slow-scale motion correctly.

An automated and efficient numerical solution of an initial value problem for ordinary differential equations

$$\frac{dy}{dt} = f(y(t), t), \qquad y(t = 0) = y_0, \tag{5.1}$$

were $t \geq t_0$ and $y : \mathscr{R} \to \mathscr{R}^n$ remained an active topic of research since the very early days of computing [47]. Most of the solution methodologies would reconstruct time trajectory by recognizing that a continuous approximation can be obtained by connecting neighboring points via smooth polynomial curves such as straight lines (explicit/implicit Euler method), parabola (midpoint or trapezoidal method) or nth order curves (explicit/implicit Runge-Kutta method). When these reconstructions respect causality and use only tangent information from the past, the resultant methods are explicit. On the other hand, when numerical reconstruction of ODE trajectory uses tangent information from the future, the unknown solution $y(t^{\text{new}})$ appears both on the left-hand side and right-hand side in a non-linear fashion. Thus, the resulting methods are termed implicit methods. One often needs to use Newton-Raphson and linear equation solvers as the resulting equations are non-linear systems of equations. Generally, explicit methods are simpler to use, and thus, they still exist as a natural first choice. In particular, explicit methods are useful for solving hyperbolic partial differential equations and Hamiltonian dynamics. On the other hand, for stiff ODE or parabolic PDE, the implicit method tends to be the method of choice [117]. Regardless of the use of explicit or implicit methods, the computational challenge of stiff multiscale systems stems from trying to resolve efficiently the slow time scale behavior while incorporating the effects from the fast and intermediate time scales. The relative merits of both classes of methods are extremely well understood[139] . For example, the conventional wisdom till recently was that all reasonable methods for stiff systems must be implicit to avoid a severe restriction on the step size [15, 117].

Indeed, in the presence of multiple time scales in a problem, the overall efficiency of a conventional explicit method for a stiff ODE is relatively poor. This is related to the fact that an important consequence of stiffness or presence of time scale separation is that one has a slowly varying solution (slow manifold), which is such that some perturbations to it are damped in a very short duration[118]. In particular, a slight error in the predicted solution can put the trajectory on a nearby solution curve that steeply approaches (thus a very large slope) the slow manifold. For step sizes that are too large, the wrong computation of the fast transients leads to a predicted solution which becomes increasingly worse and moves further away from the slow manifold; the explicit method becomes unstable. Thus, one must follow the fastest time scale to capture the rapid variations in a stable fashion [47, 52, 91].

In contrast to explicit methods, implicit methods generally do not suffer from the restriction of time steps constrained to the fastest time scale of the original ODE. Some implicit techniques are very efficient in damping exponentially decaying mode, while many others show oscillatory behavior. We need exponentially decaying modes to be damped out to recover the slow dynamics. Thus, it is widely accepted that efficient integration of stiff ODEs requires a class of implicit methods (A-stable), which also shows efficient damping of exponentially decaying mode (L-stable). A good implicit method takes a considerably large time jump in contrast to a typical explicit method for stiff ODE. However, in general, the cost of an implicit method is relatively high due to the need to solve linear or non-linear equations at every time step. In recent years, due to the increase in the compute performance capability (number of floating point operations FLOPs) of modern hardware, there has been a revival of interest in explicit methods, which, in contrast to implicit methods, are often an order of magnitude more efficient for single time-step. However, an explicit method typically has a minimal stability region; thus, it often requires a time step that is too small. This necessity of taking a large number of steps nullifies the advantage of a low cost per time. Several attempts were made in the last two decades to obtain explicit schemes for the stiff system of equations which can take large steps. Among them, perhaps one of the most elegant and successful ones is the so-called projective integration methods introduced by Gear and Kevrikidis[53], which are effective methods for the computation of long-time behavior in complex multiscale problems. The central idea is to use short bursts of appropriately initialized simulations to estimate the time derivative of the quantities of interest and then use polynomial extrapolation to jump forward. Traditionally, stiff systems of ODE are solved via the Gear scheme and its derivative method [52]. In this chapter, we briefly summarise the projective Euler method and propose a modification to the scheme that increases the stability window.

5.2 Stiff differential equations

In this section, we will review the fundamental concepts of integrating the slow dynamics and analyze how slowly varying solutions are affected by perturbations which are damped in a very short duration[118]. Consider a uniform grid in time with $t_n = nh$ where n is a non-negative integer, and h is the time-step. On this grid, we consider the discrete form of Eq.(5.1) as

$$y^{n+1} = y^n + h\left[\theta f(y^n, t_n) + (1-\theta) f(y^{n+1}, t_n + h)\right], \tag{5.2}$$

which for $\theta = 1$ is the forward Euler method which reconstructs the solution locally from the slope information at the point and for $\theta = 0$ is the backward Euler method, an implicit method, which uses slope at t_{n+1}. The value $\theta = 1/2$ corresponds to the second-order Trapezoidal scheme.

As a first example, let us consider an initial value problem of the form

$$\frac{dx}{dt} = -\frac{1}{\tau}(x - g(t)) + \frac{dg}{dt} \tag{5.3}$$

whose general solution is

$$x(t) = \exp\left(-\frac{t}{\tau}\right)(x(0) - g(0)) + g(t). \tag{5.4}$$

From which the long term solution can be deduced as

$$\lim_{t>>\tau} y(t) = g(t). \tag{5.5}$$

As a specific example we consider $g(t) = A\cos(\omega t)$ with $x(t=0) = x_0$. We can notice from the exact solution

$$x(t) = (x_0 - A)\exp\left(-\frac{t}{\tau}\right) + A\cos(\omega t), \tag{5.6}$$

that for $\omega\tau \ll 1$, the ODE has a fast, exponentially decaying component and a slow trigonometric part which survives for a long time. Each gray line in Figure 5.1 (called a solution curve) corresponds to the time evolution of the system starting at a different initial condition. Starting from any initial condition, one can notice how the system exponentially converges to the slower dynamics of $\cos(t)$.

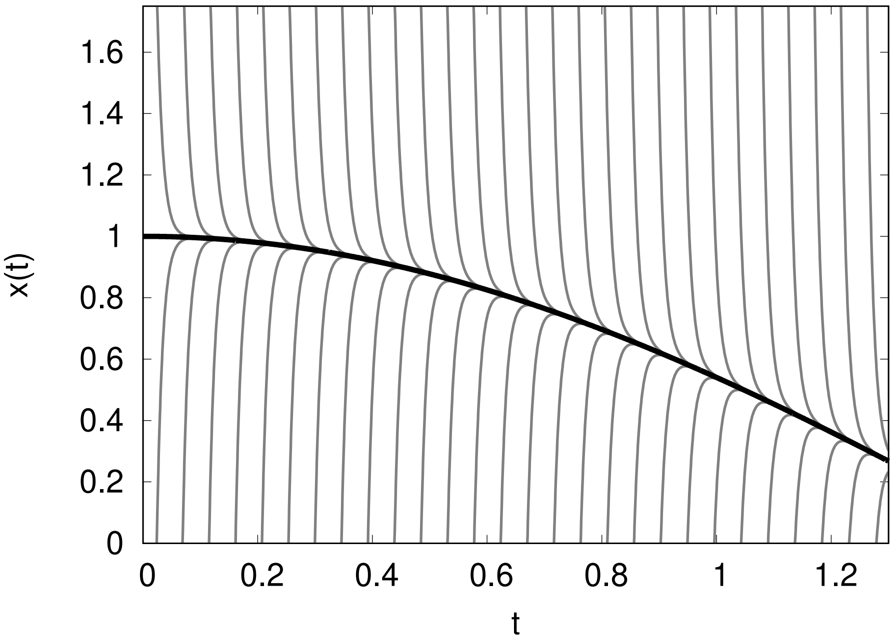

Fig. 5.1 Solution curves for $\omega = 1$, $A = 1, \tau = 0.01$.

One can see that when the numerically predicted solution is approaching the slow manifold but is on a nearby solution curve, the slope of the predicted solution is very large due to the fast time scales. This causes the explicit methods to take very small time steps to account for the rapidly changing solution erroneously. If the time step is too large, the explicit method becomes unstable as the predicted solution keeps moving further away from the actual slow manifold.

5.3 Projective integration methods

The projective integration technique [53], is an explicit method for solving stiff systems which can take large time steps. This method operates on the principle that given an approximation of the time derivative along the system's slow dynamics, one can leverage this approximation to take significantly larger time steps. This is achieved by extrapolating from the current state to a predicted future state along the slow dynamics. The geometric idea behind estimating a slow time derivative lies in the observation that any integrator (called an inner integrator from now on) employing a very small time step will, at the outset, will have dominant component along the direction of the fast time derivative. However, as integration progresses, the trajectory will gradually shift towards the slow manifold, with the direction of motion becoming more parallel to the slow dynamics. This phenomenon allows for the adoption of substantially larger projective steps by evaluating the chord slopes, which represent the transition from fast to slow dynamics. This approach is visually depicted in Figure 5.2, where integrators with small time steps (h) are denoted as red circles. After several integration steps, the solution approaches the slow manifold, effectively mitigating the fast transients. At this juncture, represented by the blue circle, the chord slope is calculated, and a much larger projective step (kh) is taken as the trajectory aligns more closely with the slow manifold. The error in extrapolation will again give a dominant component of the gradient at point A (in Figure 5.2) in the direction of slow manifold. This process can be repeated in the hope that it would give a good approximation to the overall dynamics.

The inner integrator could be any stable and at least a first-order accurate method. Here, we illustrate the projective forward Euler method, where the inner integrator is the forward Euler method. The projective integration step starts with advancing the solution for m small steps of size h as shown in Figure 5.3. The solution is then advanced by another time step by running the inner integrator once again to estimate the gradient of the slow manifold. Hence, the gradient

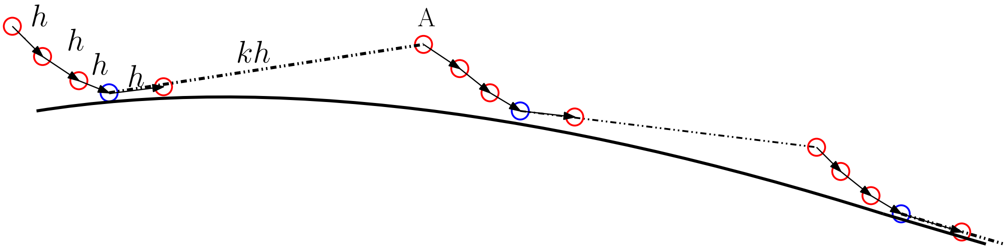

Fig. 5.2 Geometric idea of a projective integration step. The local slope is shown with a solid arrow.

can be approximated to be

$$\left.\frac{dy}{dt}\right|_{n+m} = \frac{y^{n+m+1} - y^{n+m}}{h}. \tag{5.7}$$

We follow the notation where y^{n+r} is the function value evaluated at time $(n + r \times h)$ for any real value r. A larger projective jump is performed using the estimated gradient by taking a time step that is k times the small time step as

$$y^{n+m+k} = y^{n+m} + (kh)\left.\frac{dy}{dt}\right|_{n+m}. \tag{5.8}$$

Using the approximation from Equation 5.7, we have

$$y^{n+m+k} = y^{n+m} + k(y^{n+m+1} - y^{n+m}). \tag{5.9}$$

The total length of the projective integration step, also called the outer integrator, is $(m+k)h$. It is to be noted that the derivative estimation and projective jump steps are computationally very cheap as they are just arithmetic operations acting on an array.

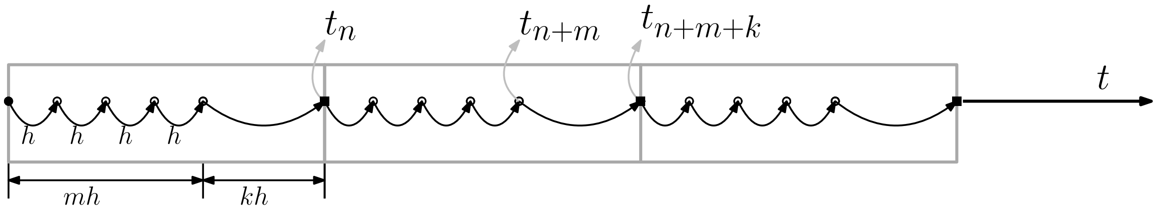

Fig. 5.3 Illustration of a projective integration step.

In the next section we perform absolute stability analysis for the regular projective Euler method.

5.4 Stability analysis

For a constant coefficient system of equations $dy/dt = Ay$, when a linear numerical integration method like forward Euler or projective forward Euler method is applied, it is equivalent to applying it separately to a constant set of equations $dy/dt = -\lambda y$ where λ are the eigenvalues of the matrix A. Hence, the linear stability can be studied on the Dahlquist's test equation

$$\frac{dy}{dt} = -\lambda\, y, \tag{5.10}$$

where λ is positive.

For the projective Euler method the slope of the chord at time $(n+m)h$ is

$$\left.\frac{dy}{dt}\right|_{n+m} = -\lambda\,(1-\lambda h)^m y^n. \tag{5.11}$$

Performing a projective integration using the derivative estimate, a recurrence relation can be obtained as

$$y^{n+m+k} = [1-k\lambda h]\,(1-\lambda h)^m y^n. \tag{5.12}$$

One can now get an estimate for the possible jump in the projective step via a stability analysis. From the above equation, for the scheme to be stable, the methods should satisfy

$$|[1-kz]\,(1-z)^m| \leq 1 \tag{5.13}$$

where $z = \lambda h$. We can now estimate the projective jump from the above stability criteria. The permitted jump during the projection step is

$$k \leq \frac{1}{z}\left[1+\frac{1}{(1-z)^m}\right]. \tag{5.14}$$

We remind that for the forward Euler method to be stable $0 \leq z \leq 2$. We analyze the behavior of the projective method within two distinct intervals: $0 \leq z \leq 1$ and $1 < z \leq 2$. In the first interval, $0 \leq z \leq 1$, one can see that the values of k are very large. This can be attributed to the factors $1/z$ and $1/(1-z)^m$. As both z and $|1-z|$ lie within the range $[0,1]$, their reciprocals are significantly greater than unity for smaller z values, thus amplifying the value of k. Conversely, within the interval $1 \leq z \leq 2$, the value of k rapidly approaches unity as z increases beyond

1.5. This convergence effectively reduces the projective method to the standard forward Euler method, thereby imposing a severe constraint on its applicability and undermining its intended advantages. For systems whose eigenvalues are not known a priori this is a significant restriction as half of the stability zone is out of bounds for the projective integration step.

To this extent, we propose a minor modification to the protective method in the next section.

5.5 Modified projective integration method

In this section, we present a modification to the projective integration method. Similar to the projective forward Euler method, we march forward m steps with the forward Euler method and then compute the slope of the chord at y^{n+m}. We march one more step with the inner integrator to obtain an estimate of y^{n+m+1}. We then compute an estimate for the function $\left(y^{n+m+1}\right)^*$ at time $n+m+1$ using the average of function values y^{n+m} and y^{n+m+1} as

$$\left(y^{n+m+1}\right)^* = y^{n+m} + h\, f\left(\frac{y^{n+m} + y^{n+m+1}}{2}\right).$$

Note that this is a variation of mid-point method and not the Heun method of trapezoidal integration, where one would use the average of slopes instead to get an estimate as

$$\left(y^{n+m+1}\right)^* = y^{n+m} + h\left(\frac{f\left(y^{n+m}\right) + f\left(y^{n+m+1}\right)}{2}\right).$$

We use this function value to compute the new gradient approximation as

$$\left.\frac{dy}{dt}\right|_{n+m} = \frac{\left(y^{n+m+1}\right)^* - y^{n+m}}{h},$$

and perform a projective jump of k - steps, which gives the final relation

$$\tilde{y}^{n+m+k} = y^{n+m} + k\left(\left(y^{n+m+1}\right)^* - y^{n+m}\right). \tag{5.15}$$

5.6 Stability analysis for the modified projective method

We now perform absolute stability analysis for the proposed modification of the projective Euler method to get estimates on the possible jump in the projective jump. Following the procedure

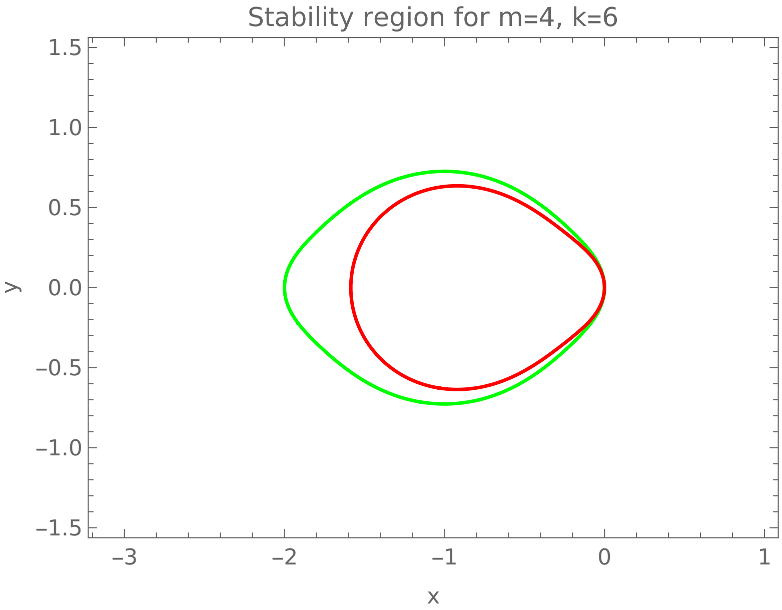

Fig. 5.4 Stability region for $m=4$ and $k=6$ values (Proposed scheme - Green, Regular Projective Euler - Red)

outlined in Section 5.4, computing the derivative using a trapezoidal approximation, the slope of the chord at time $(n+m)h$ is

$$\left.\frac{dy}{dt}\right|_{n+m} = -\lambda\left(1-\frac{\lambda h}{2}\right)(1-\lambda h)^m y^n. \tag{5.16}$$

A recurrence relation can obtained to be

$$\tilde{y}^{n+m+k} = [1-k\lambda h]\,(1-\lambda h)^m y^n, \tag{5.17}$$

with the stability criteria as

$$\left|\left[1-kz\left(1-\frac{z}{2}\right)\right](1-z)^m\right| \leq 1. \tag{5.18}$$

It can be seen that the modified projective method increases the stability zone. In Figure 5.4, we show compare the the stability zone for the regular and modified projective method based on their respective stability limits.

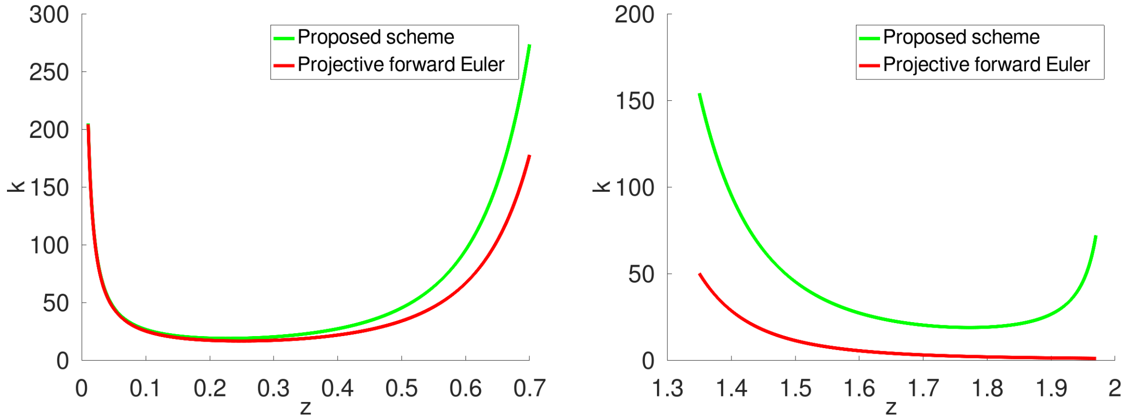

Fig. 5.5 Contrasting allowed projective jump k value for both schemes for different z values. The ranges are chosen such that the k value doesn't approach infinity ($k \to \infty$ when $z \to 0, 1$ for regular projective scheme and $z \to 0, 1, 2$ for the proposed scheme).

We can now estimate the projective jump from the above stability criteria. The permitted jump during the projection step for the modified projective method is

$$k \leq \frac{1}{\left(\mathbf{1} - \frac{\mathbf{z}}{\mathbf{2}}\right)} \frac{1}{z} \left[1 + \frac{1}{(1-z)^m} \right]. \tag{5.19}$$

From the above equation, we can see that when the inner integrator is executed an even number of times (i.e. when m is even) and as z approaches 2, the proposed modified projective order method will have a significantly higher projective jump while the regular method limits its value to 1. This amplification is due to the $(1 - z/2)$ factor in the denominator arising from the modified slope computation. Figure 5.5 provides a graphical comparison of the k values for both schemes showing this disparity.

Hence, it can be seen that the proposed modified projective method not only provides a better estimate for the local derivative estimate of the slow manifold but also enables a significantly higher jump in the projection step compared to the regular projective method.

5.7 Validation

In the next section, we present some canonical test cases from various fields. Here, we contrast the solutions for our proposed method with forward Euler solutions. The number of iterations that the forward Euler method needs will be a few orders of magnitude higher in each case.

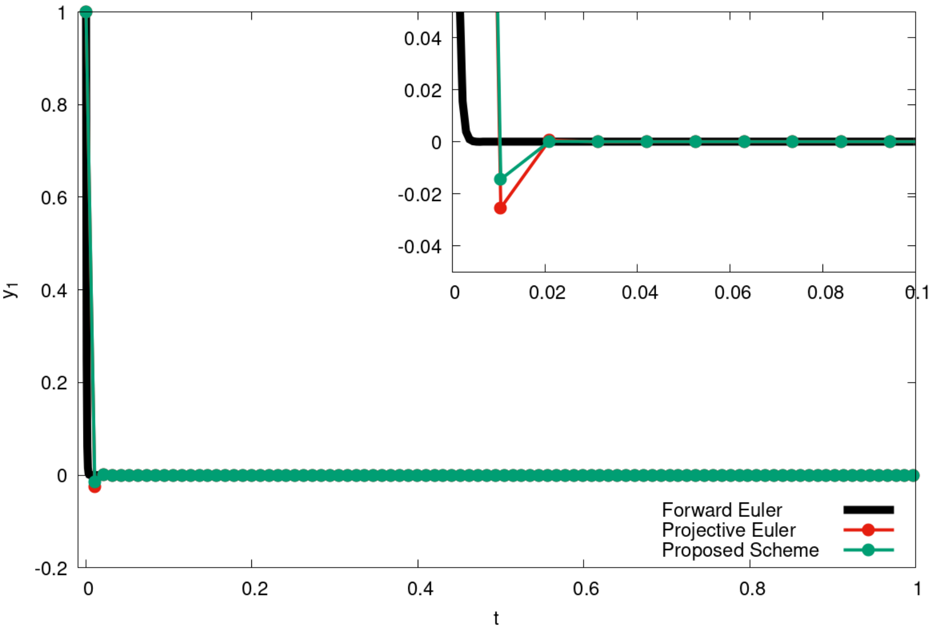

Fig. 5.6 Evolution of y_1 for Dahlquist's test equation at $\lambda h = 0.75$ with $(m,k) = (4,10)$.

We begin validation of the scheme with Dahlquist's test equation

$$\frac{dy_1}{dt} = -\lambda y_1, \qquad y_1(t=0) = y_0, \tag{5.20}$$

on $t \in [0,1]$ with $y_0 = 1$ and $\lambda = 1000$. The minimum time step h that forward Euler method needs to solve this problem is $0 \leq \lambda h \leq 2$. It needs to be noted that the amplification factor for forward Euler method is non-negative if $0 \leq \lambda h \leq 1$ and is negative when $1 < \lambda h \leq 2$. Negative amplification factor leads to spurious oscillations. We demonstrate that the proposed method does marginally well in the $0 \leq \lambda h \leq 1$ regime compared to the regular projective method in Figure 5.6 where λh value was chosen to be 0.75. In the $1 < \lambda h \leq 2$ limit, the proposed method significantly outperforms the standard projective method with fewer oscillations as shown in Figure 5.7 for $\lambda h = 1.75$. The number of inner integrator steps m was chosen to be 4 with a projective jump $k = 10$ for both the projective methods.

We now extend the analysis to the test equation with cosine component

$$\frac{dy_1}{dt} = -\lambda(y_1 - 10\cos(t)), \qquad y(t=0) = 1. \tag{5.21}$$

We show in that in the limit $\lambda h < 1$, both the methods perform similarly. This can be seen in Figure 5.8 where λh is set to 0.9. The proposed method does significantly better in $1 < \lambda h < 2$

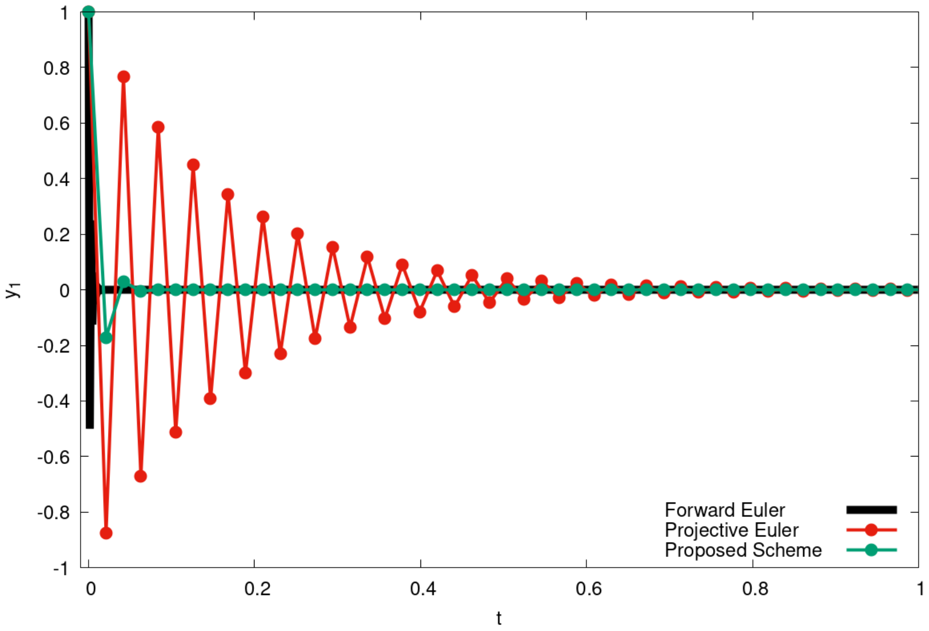

Fig. 5.7 Evolution of y_1 for Dahlquist's test equation at $\lambda h = 1.5$ with $(m,k) = (4,10)$.

range. This can be seen from the comparison of both methods at $\lambda h = 1.6$ in Figure 5.9. The regular projective method fails to converge at $\lambda h = 1.75$, while the proposed method converges to the long time solution of cosine component. λ, m and k values for this setup are chosen to be $1000, 4$ and 10 respectively.

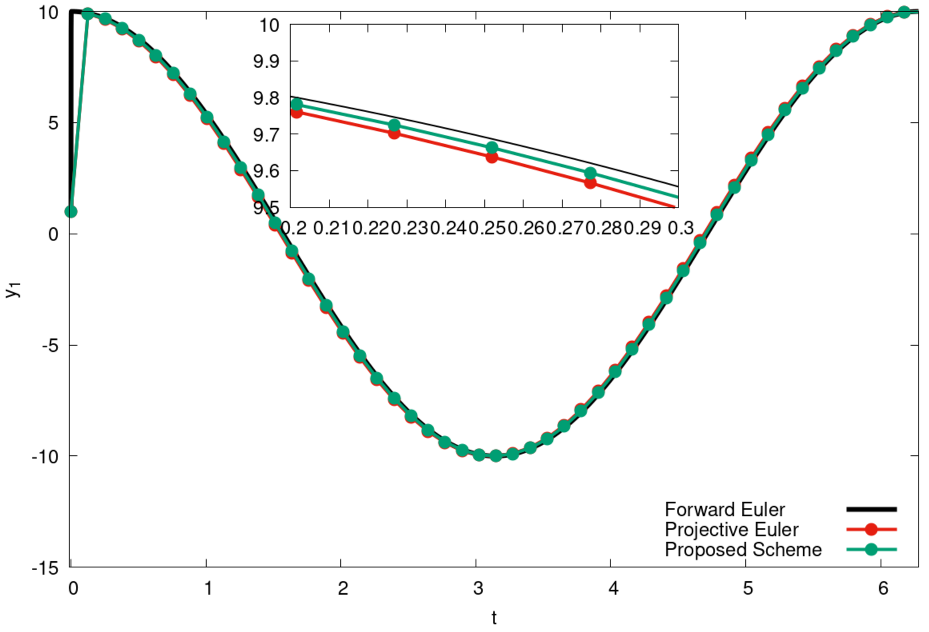

Fig. 5.8 Test equation with cosine component at $\lambda h = 0.9$

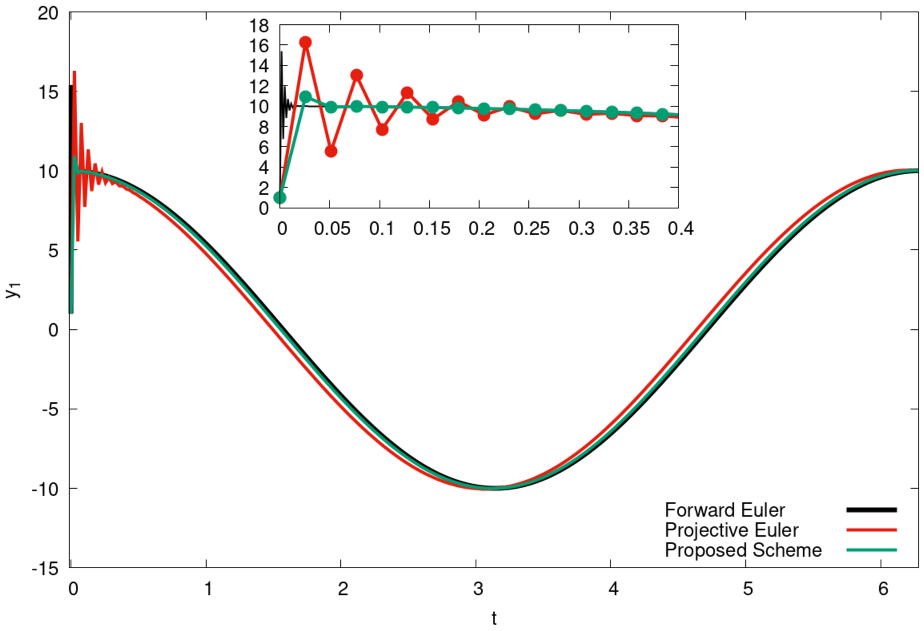

Fig. 5.9 Test equation with cosine component at $\lambda h = 1.6$

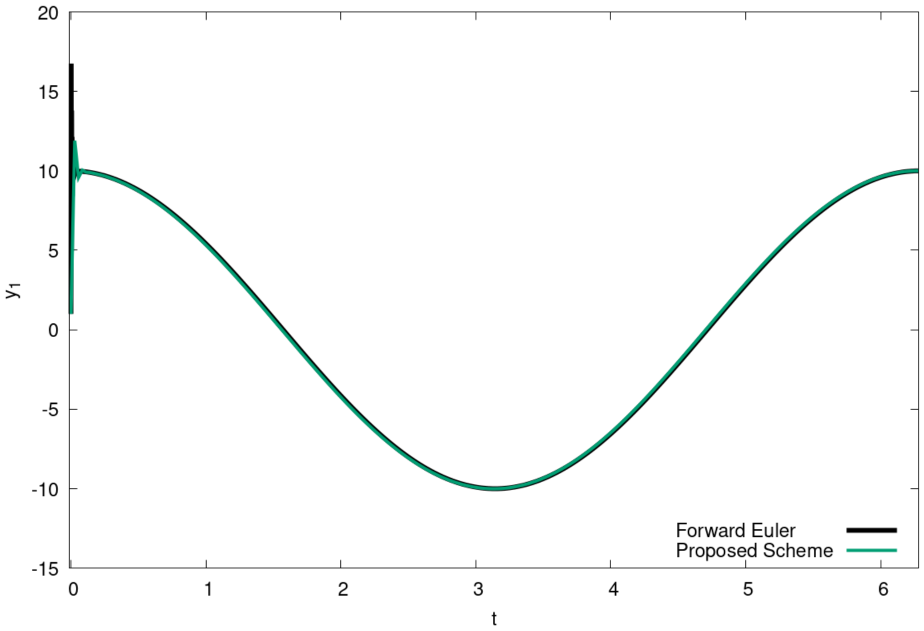

Fig. 5.10 Test equation with cosine component at $\lambda h = 1.75$. Regular projective method fails to converge in this limit and is not shown.

The HIRES problem, also known as the High Irradiance Response problem, is derived from plant physiology [115]. It is characterized by a chemical reaction involving eight reactants ($y_1 \cdots y_8$). The chemical reactions are described by the following stiff system of non-linear differential equations.

$$\frac{d}{dt}\begin{pmatrix} y_1 \\ y_2 \\ y_3 \\ y_4 \\ y_5 \\ y_6 \\ y_7 \\ y_8 \end{pmatrix} = \begin{pmatrix} -1.71y_1 + 0.43y_2 + 8.32y_3 + 0.0007 \\ 1.71y_1 - 8.75y_2 \\ -10.03y_3 + 0.43y_4 + 0.035y_5 \\ 8.32y_2 + 1.71y_3 - 1.12y_4 \\ -1.745y_5 + 0.43y_6 + 0.43y_7 \\ -280y_6y_8 + 0.69y_4 + 1.71y_5 - 0.43y_6 + 0.69y_7 \\ 280y_6y_8 - 1.81y_7 \\ -280y_6y_8 + 1.81y_7 \end{pmatrix}, \quad \begin{pmatrix} y_1(t=0) \\ y_2(t=0) \\ y_3(t=0) \\ y_4(t=0) \\ y_5(t=0) \\ y_6(t=0) \\ y_7(t=0) \\ y_8(t=0) \end{pmatrix} = \begin{pmatrix} 1 \\ 0 \\ 0 \\ 0 \\ 0 \\ 0 \\ 0 \\ 0.0057 \end{pmatrix} \tag{5.22}$$

till $0 \leq t \leq 321.8122$. The evolution of these eight reactants using all the three methods are shown in the following images. It can be seen that for the same h, m and k values the proposed method is stable and matches with the solution obtained from the forward Euler method, where as the regular projective Euler method becomes unstable with spurious oscillations. (m,k) for this case are chosen to be $(4,10)$.

The time evolution of each of these reactants is given in the following figures where the solutions obtained from the regular projective scheme, modifed projective method and forward Euler method are compared. The dynamics of reactants y_1, y_2 demonstrate similar behavior across both methods compared to forward Euler method, as shown in Figures 5.11 and 5.12. While the long-term dynamics for y_3 and y_4 appear similar, a closer examination reveals that the regular projective method begins to underpredict the concentration values in the region starting from $t = 200$ as shown in Figures 5.13 and 5.14. This discrepancy becomes more pronounced for species y_5 as shown in Figure 5.15. These observations can be attributed to the onset of instability in the regular projective scheme around $t = 200$, which is evident in the evolution of species y_6 as shown in 5.16. This instability is further amplified in the dynamics of y_7 and y_8 dynamics as shown in Figures 5.17 and 5.19.

In contrast the proposed projective method successfully captures the dynamics and accurately matches the solution obtained from the forward Euler method for all species at all times. The dynamics of y_7 and y_8 with only the proposed projective scheme and the forward Euler solution are shown in Figures 5.18 and 5.20 for better comparison.

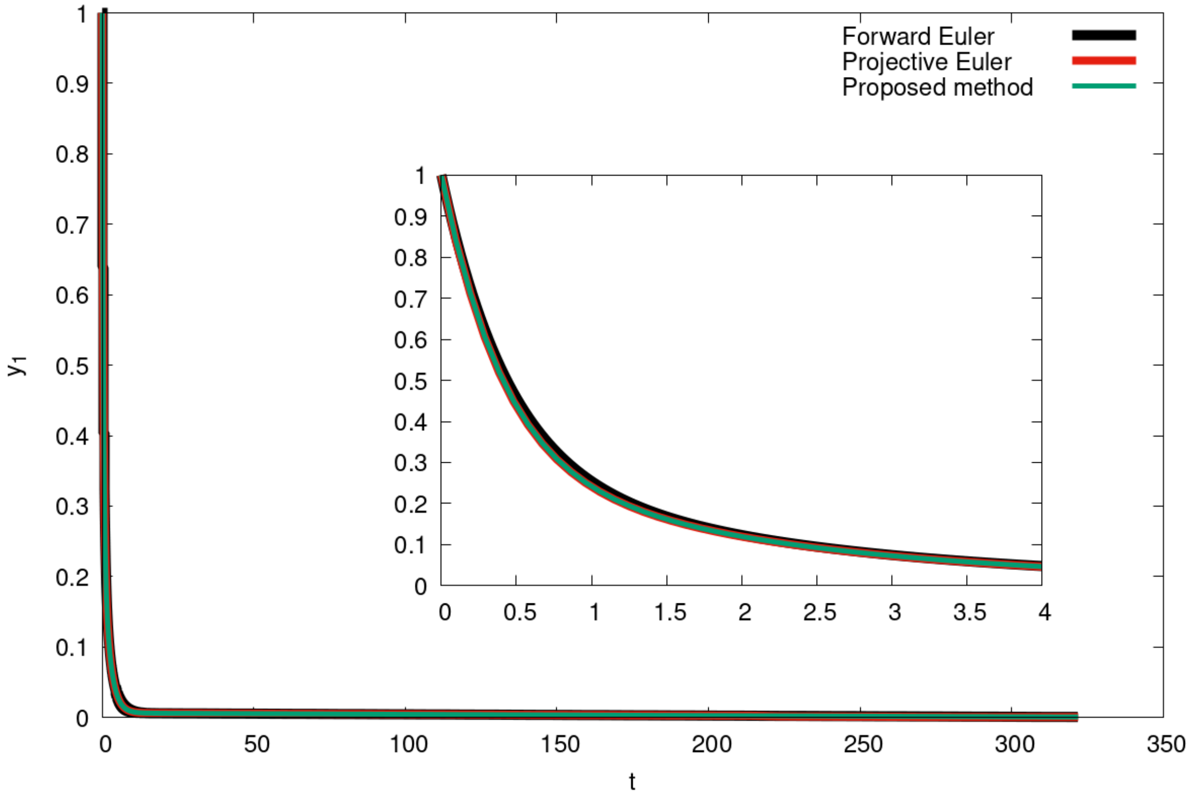

Fig. 5.11 Evolution of reactant y_1 for HIRES problem

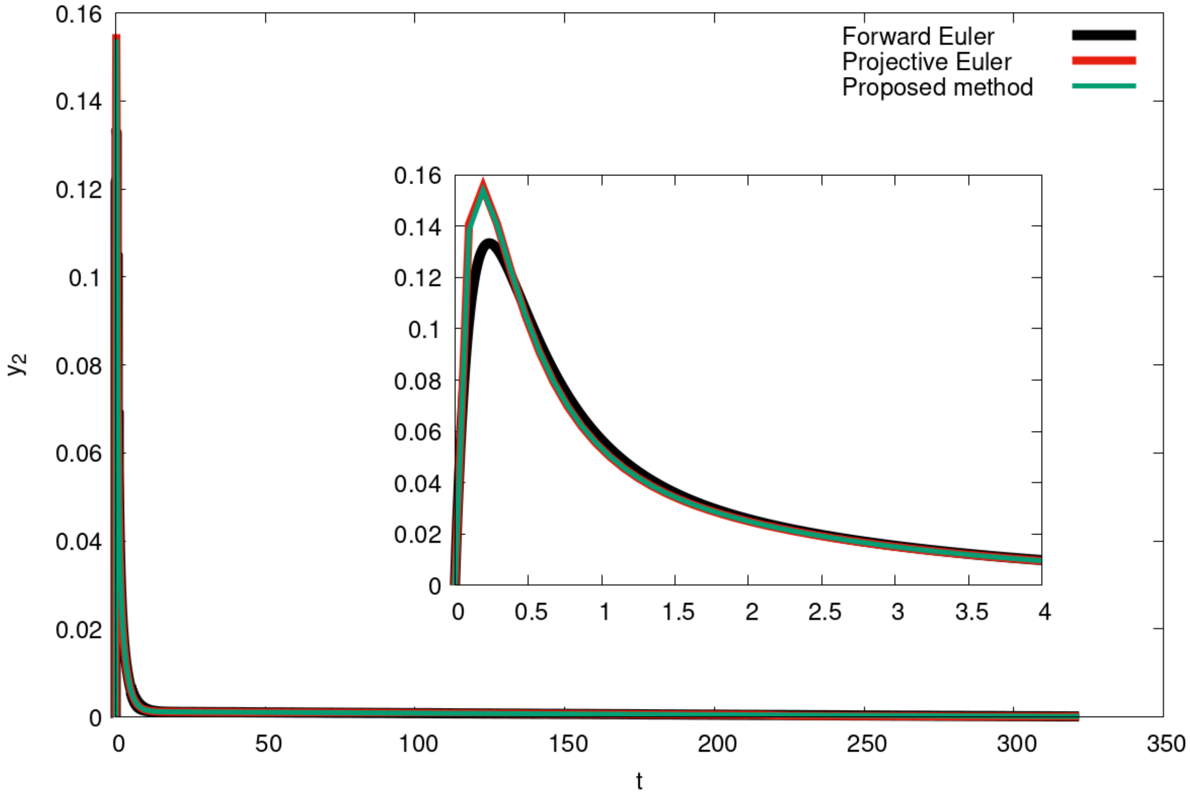

Fig. 5.12 Evolution of reactant y_2 for HIRES problem

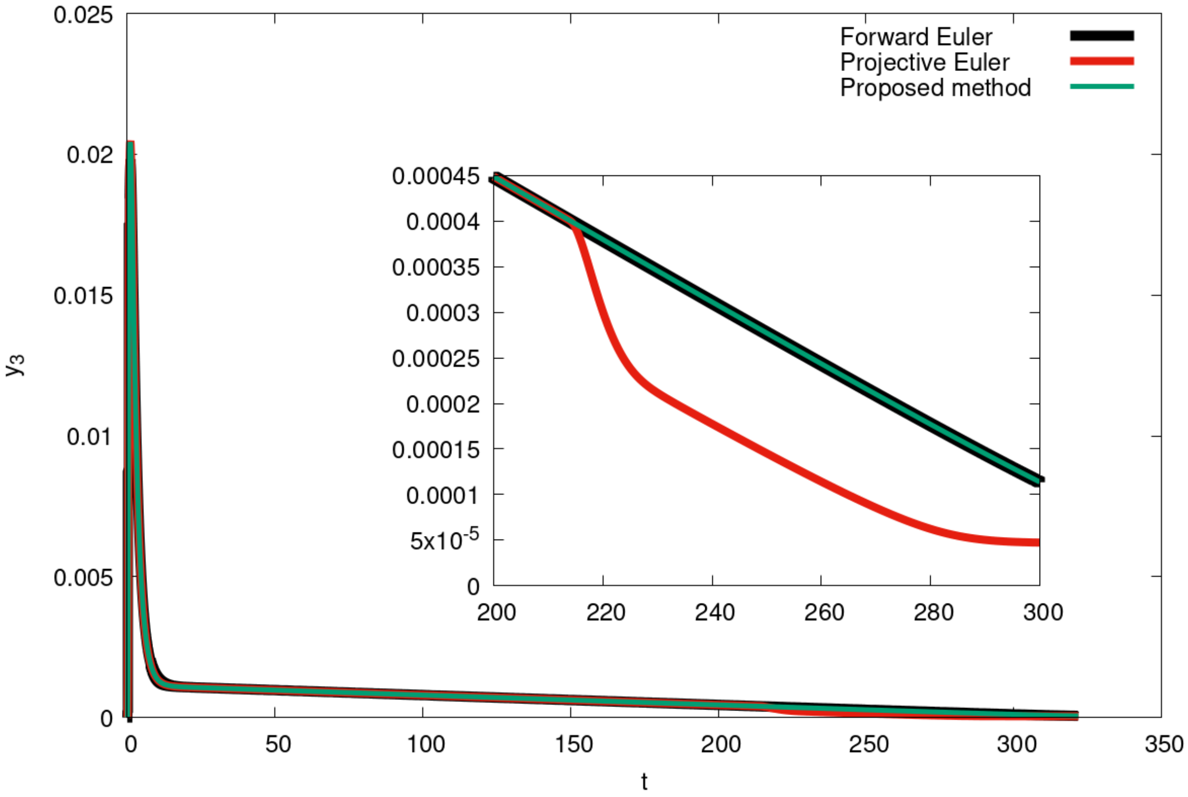

Fig. 5.13 Evolution of reactant y_3 for HIRES problem

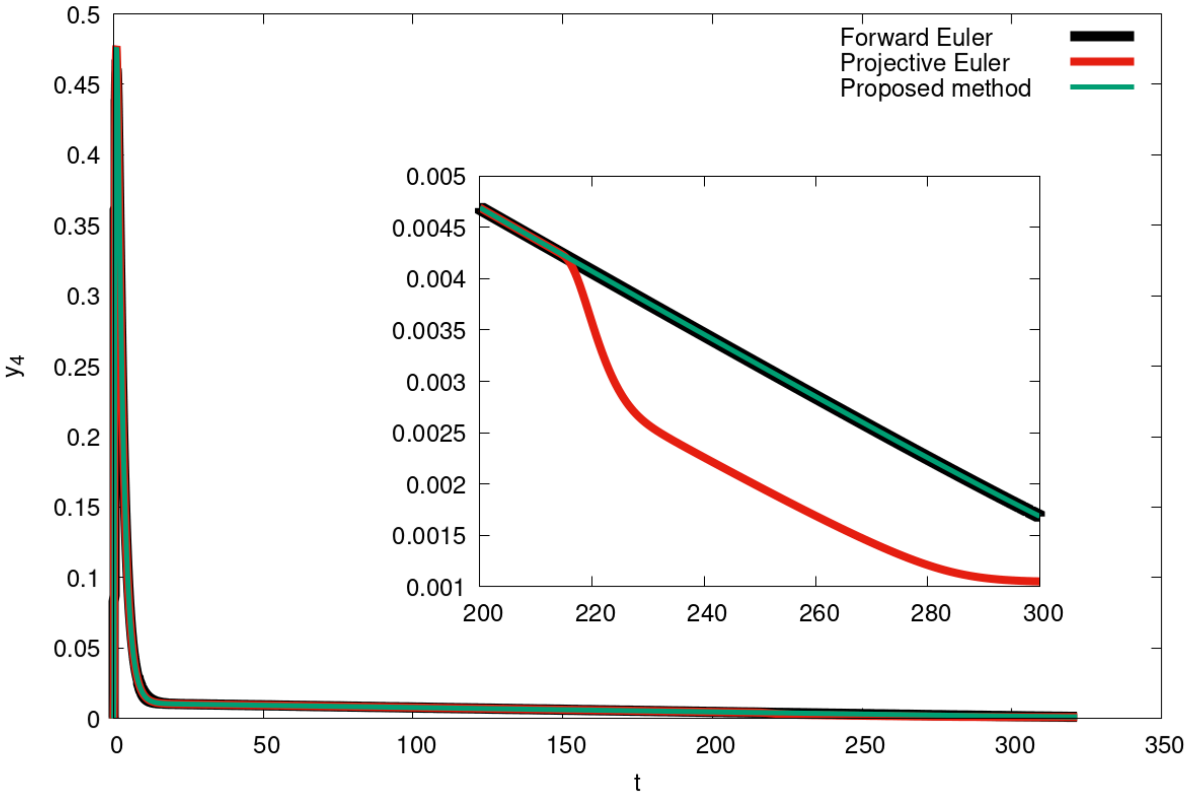

Fig. 5.14 Evolution of reactant y_4 for HIRES problem

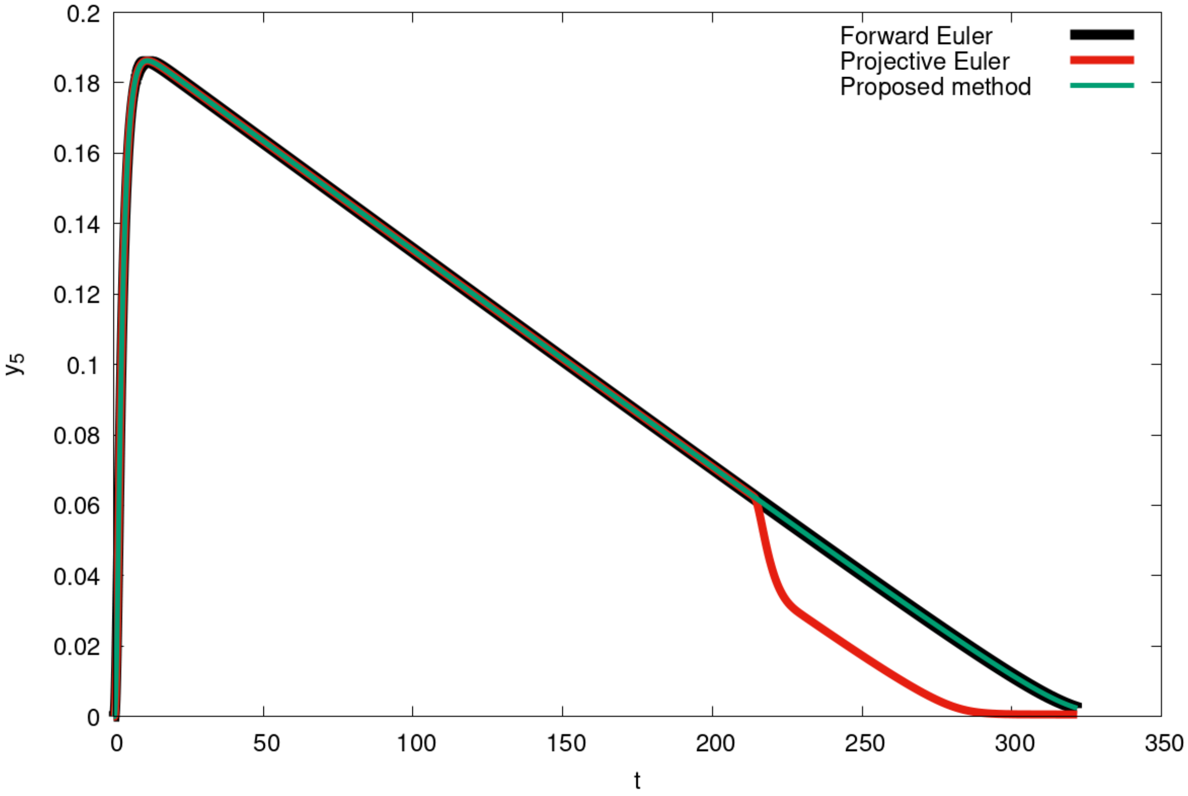

Fig. 5.15 Evolution of reactant y_5 for HIRES problem

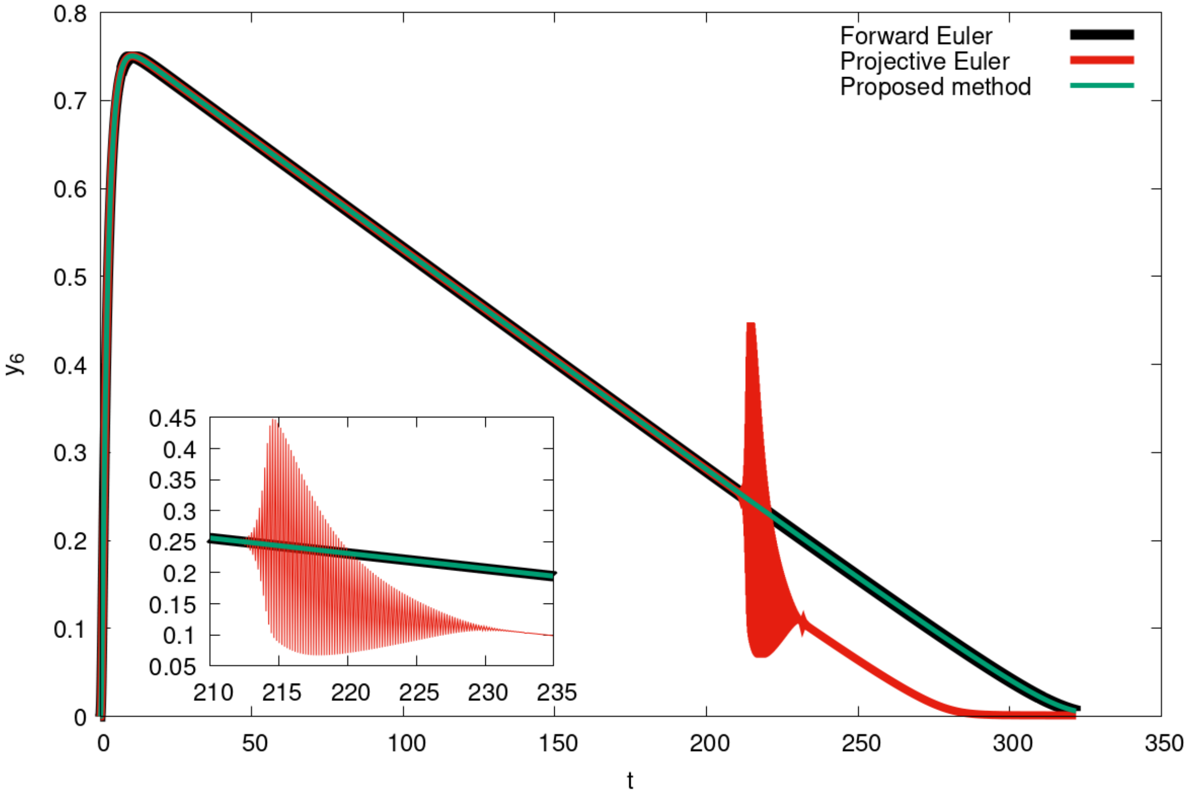

Fig. 5.16 Evolution of reactant y_6 for HIRES problem

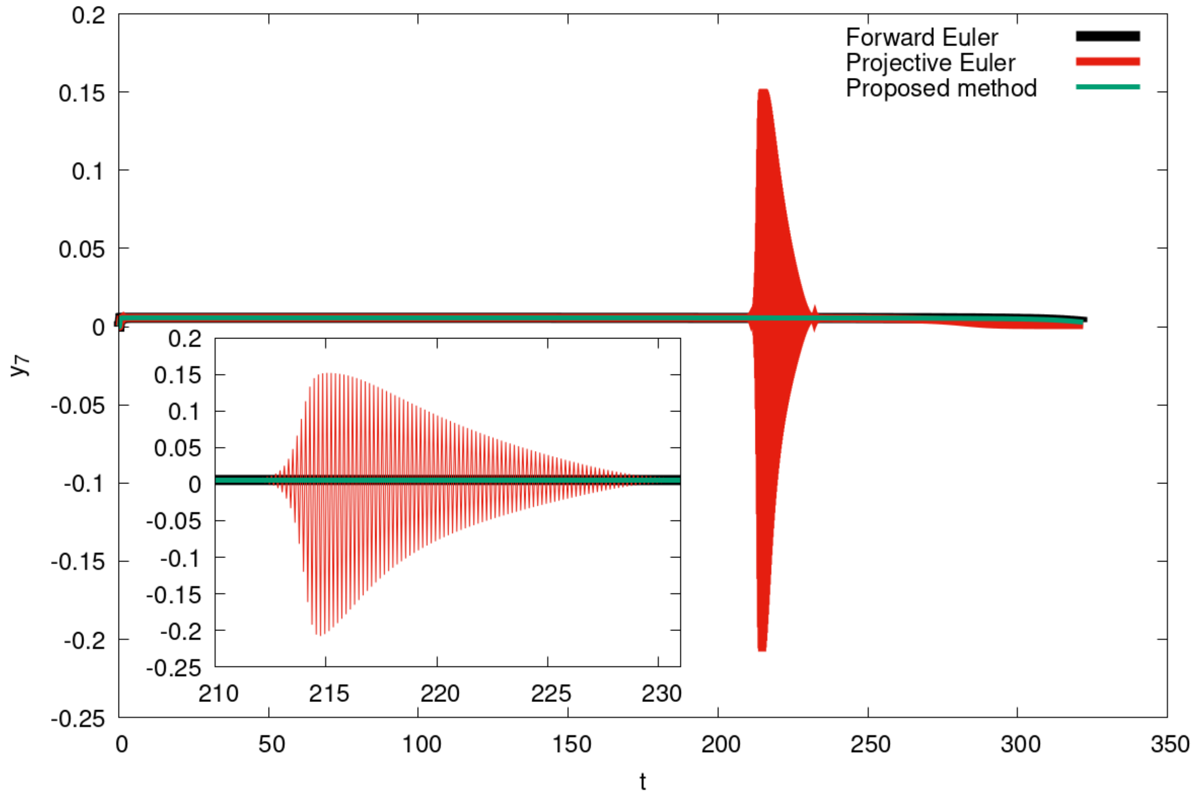

Fig. 5.17 Evolution of reactant y_7 for HIRES problem. Notice that regular projective becomes unstable.

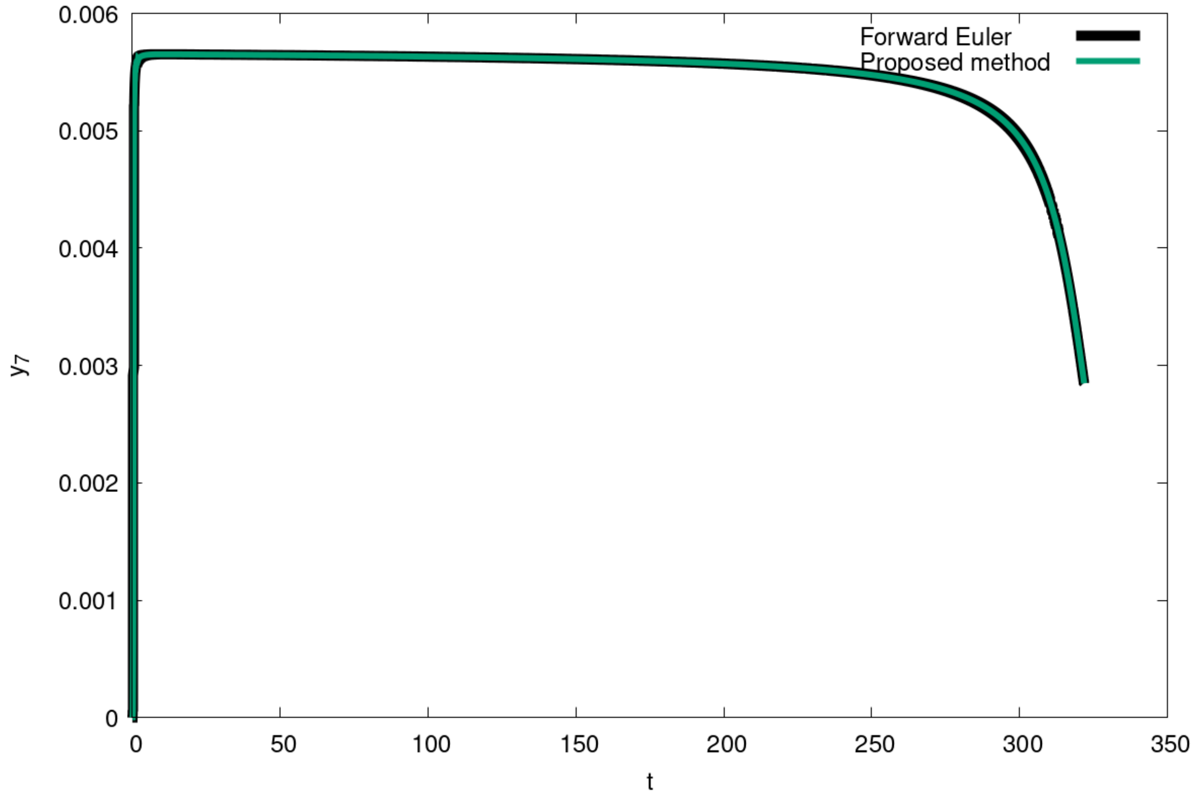

Fig. 5.18 Evolution of reactant y_7 for HIRES problem with proposed scheme

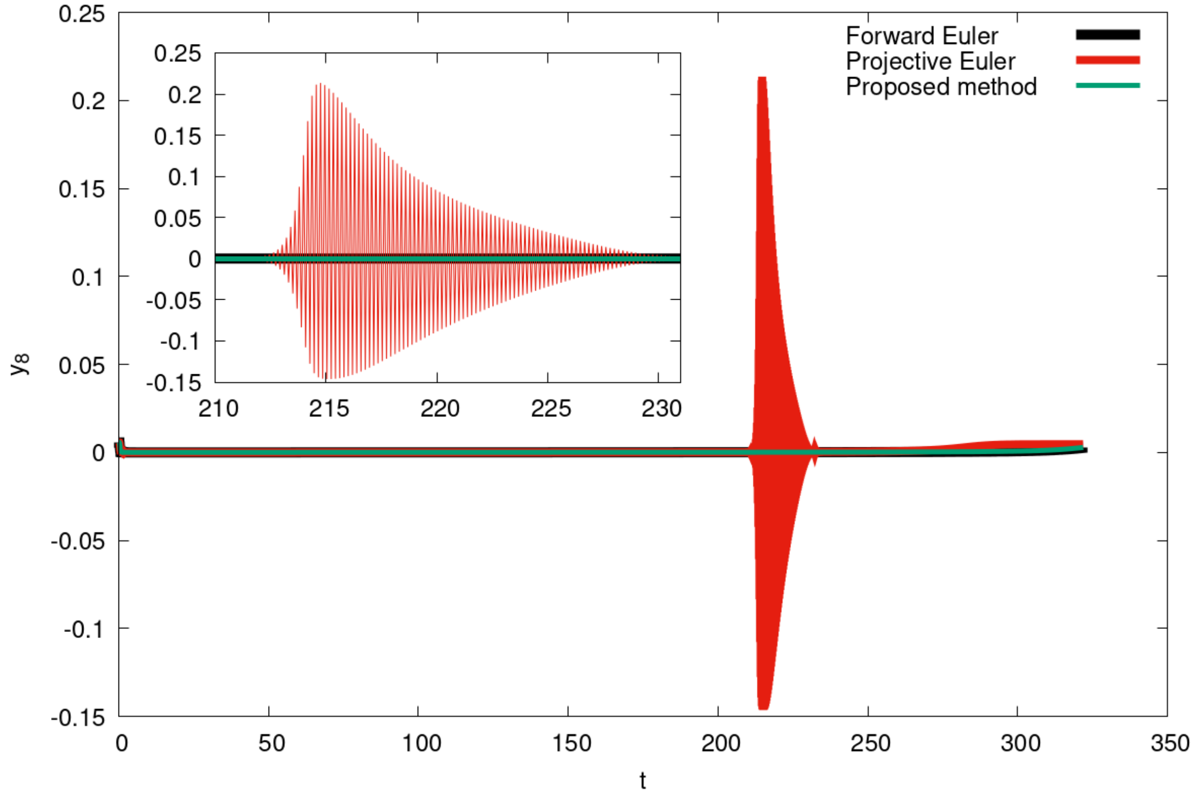

Fig. 5.19 Evolution of reactant y_8 for HIRES problem. Notice that regular projective becomes unstable.

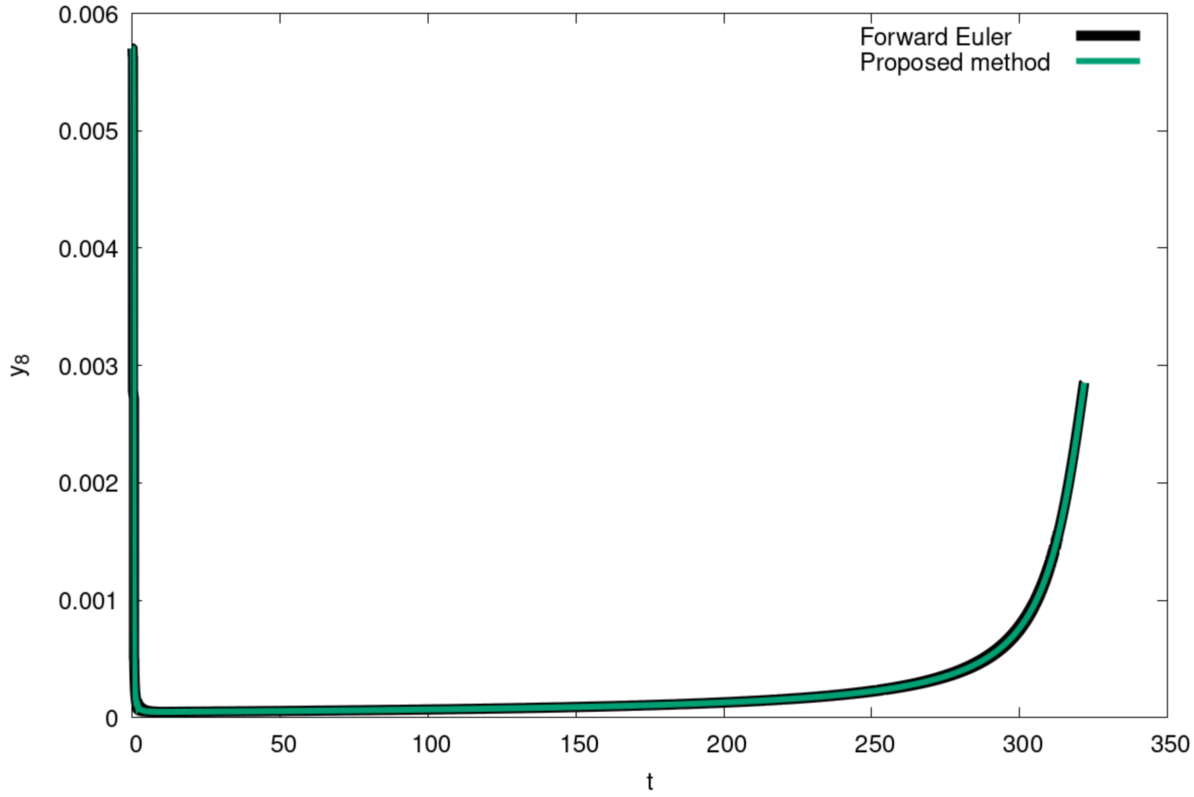

Fig. 5.20 Evolution of reactant y_8 for HIRES problem with proposed scheme

5.8 Conclusion

This work proposes a simple yet effective modification to the forward projective Euler scheme. We show that by an additional computation for estimating the slope during the projective step, a significant improvement in stability range and magnitude of projective jumps can be achieved. Unlike the regular projective forward Euler method, the proposed method allows for a substantial increase in the possible jump, particularly in the stability region $1 \leq z \leq 2$. This is advantageous for stiff systems, such as chemical reaction equations encountered in combustion, where computing the Jacobian is computationally expensive and estimates of step sizes are unknown,.

We validate the effectiveness of this approach through a series of standard examples, illustrating that the proposed method remains stable and converges to the slow manifold in regions where the standard projective Euler scheme fails to converge. This improvement has potential applications in various domains involving the numerical integration of differential equations, particularly those with stiffness and could benefit by taking large projective steps.

Chapter 6

Conclusion and Outlook

Kinetic models of polyatomic gas typically account for the internal degrees of freedom at the level of the two-particle distribution function. In this thesis, we have proposed a kinetic model for polyatomic gases with a tunable Prandtl number by augmenting the ES–BGK model, an extension of the BGK model, at the level of the single-particle distribution function with an advection-diffusion-relaxation equation for the rotational energy. We show that close to the hydrodynamic limit, the internal degrees of freedom tend to be well represented just by rotational kinetic energy density and the proposed model recovers the compressible hydrodynamic equations of polyatomic gases as its macroscopic limit. It was shown that the transport coefficients of the model can be tuned for the simulation of flows at different Prandtl numbers and specific heat ratios. A set of free parameters such as number of rotational degrees of freedom, translation relaxation time, rotational relaxation time, rotational thermal conductivity, and a free parameter b in the ES–BGK model can be used to tune the specific heat ratio, shear viscosity, bulk viscosity and set a target Prandtl number. This framework is general enough to deal with a more complex model of internal structures. We also demonstrated that the model respects the H theorem. We then demonstrated that the model's simplicity makes it suitable for LB and other numerical implementations.

We have presented an energy-conserving lattice Boltzmann model which is suitable for weakly compressible hydrodynamics, aeroacoustics and thermoacoustic problems. We showed that it recovers the pressure dynamics and the isentropic sound speed in addition to the effects of viscous heating, heat conduction with a high degree of accuracy. The theoretical requirements and the methodology to construct this model have been discussed, and the test cases confirm its stability for a wide range of parameters. With improved accuracy in the velocity space and better representation of the curved surfaces, this model raises the prospect of direct simulations of turbulent flows involving objects. This has been shown via simulations of Kida-Pelz flow, channel flow and flow past a sphere, we demonstrated that this model is capable of direct simulations of turbulent flows involving objects aswell.

With the idea of extending these approaches to reactive systems such as combustion, we explore the possibility of using projective integration methods for solving the chemical kinetics rate equations, which are stiff in nature. We performed a preliminary investigation and showed that a better estimate for derivative estimation exists in the projective integration step.

The methods presented in this thesis can be expanded for accurate simulations of reactive gas mixtures. The modified projective integration method can be used to simulate chemical reactions, and the reduced kinetic model for polyatomic gases can accurately model gases with the correct transport properties. By developing a coupled solver for chemical kinetics and hydrodynamics using the proposed energy-conserving lattice Boltzmann model, direct numerical simulations of reactive mixtures become feasible. This coupled solver would be valuable for creating digital twins of complex systems such as gasifiers. The use of explicit methods for chemical kinetics and the local nature of lattice Boltzmann methods reduce computational complexity, making this an attractive alternative to traditional solvers. The chemical kinetics solver via projective Euler method is embarassingly parallel in nature, as the equations are solved at every grid point and are independent of their neighbours at a given time step. Therefore, a coupled solver with the lattice Boltzmann method, known for its scaling efficiency across thousands of cores, is ideally suited for deployment on exascale clusters.

Such a coupled solver integrating chemical kinetics and hydrodynamics, using the proposed energy-conserving lattice Boltzmann model and projective integration methods, could make simulation of reactive gas mixtures and complex chemical processes a possibility in exascale clusters. This enables the creation of accurate digital twins of complex systems like gasifiers, for better understanding of combustion and process optimization.

References

[1] Abramowitz, M. and Stegun, I. A. (1965). *Handbook of Mathematical Functions: With Formulas, Graphs, and Mathematical Tables*, volume 55. Courier Corporation.

[2] Agrawal, A., Kushwaha, H. M., and Jadhav, R. S. (2019). *Microscale flow and heat transfer: mathematical modelling and flow physics*. Springer.

[3] Agrawal, S., Singh, S. K., and Ansumali, S. (2020). Fokker–Planck model for binary mixtures. *J. Fluid Mech.*, 899:A25.

[4] Aidun, C. K. and Clausen, J. R. (2010). Lattice-boltzmann method for complex flows. *Annu. Rev. Fluid Mech.*, 42:439–472.

[5] Alim, U. R., Entezari, A., and Moller, T. (2009). The lattice-boltzmann method on optimal sampling lattices. *IEEE Transactions on Visualization and Computer Graphics*, 15(4):630–641.

[6] Andries, P., Le Tallec, P., Perlat, J.-P., and Perthame, B. (2000). The gaussian-bgk model of boltzmann equation with small prandtl number. *European Journal of Mechanics-B/Fluids*, 19(6):813–830.

[7] Ansumali, S., Arcidiacono, S., Chikatamarla, S., Prasianakis, N., Gorban, A., and Karlin, I. (2007a). Quasi-equilibrium lattice Boltzmann method. *Euro. Phys. J. B*, 56(2):135–139.

[8] Ansumali, S., Karlin, I., Arcidiacono, S., Abbas, A., and Prasianakis, N. (2007b). Hydrodynamics beyond Navier-Stokes: Exact solution to the lattice Boltzmann hierarchy. *Phys. Rev. Lett.*, 98(12):124502.

[9] Ansumali, S. and Karlin, I. V. (2002a). Kinetic boundary conditions in the lattice Boltzmann method. *Phys. Rev. E*, 66(2):026311.

[10] Ansumali, S. and Karlin, I. V. (2002b). Single relaxation time model for entropic lattice boltzmann methods. *Phys. Rev. E*, 65(5):056312.

[11] Ansumali, S. and Karlin, I. V. (2005). Consistent lattice boltzmann method. *Phys. Rev. Lett.*, 95(26):260605.

[12] Ansumali, S., Karlin, I. V., and Öttinger, H. C. (2003). Minimal entropic kinetic models for hydrodynamics. *Europhys. Lett.*, 63(6):798.

[13] Ansumali, S., Karlin, I. V., and Öttinger, H. C. (2005). Thermodynamic theory of incompressible hydrodynamics. *Physical review letters*, 94(8):080602.

[14] Arima, T., Taniguchi, S., Ruggeri, T., and Sugiyama, M. (2012). Extended thermodynamics of dense gases. *Contin. Mech. Thermodyn.*, 24(4-6):271–292.

[15] Ascher, U. M. and Petzold, L. R. (1998). *Computer methods for ordinary differential equations and differential-algebraic equations*. SIAM.

[16] Atif, M., Kolluru, P. K., and Ansumali, S. (2022). Essentially entropic lattice boltzmann model: Theory and simulations. *Physical Review E*, 106(5):055307.

[17] Atif, M., Kolluru, P. K., Thantanapally, C., and Ansumali, S. (2017). Essentially entropic lattice Boltzmann model. *Phys. Rev. Lett.*, 119:240602.

[18] Atif, M., Namburi, M., and Ansumali, S. (2018). Higher-order lattice Boltzmann model for thermohydrodynamics. *Phys. Rev. E*, 98:053311.

[19] Batchelor, G. K. (2000). *An introduction to fluid dynamics*. Cambridge university press.

[20] Benzi, R., Succi, S., and Vergassola, M. (1992). The lattice boltzmann equation: theory and applications. *Phys. Rep.*, 222(3):145–197.

[21] Bernard, F., Iollo, A., and Puppo, G. (2019). BGK polyatomic model for rarefied flows. *J. Sci. Comput.*, 78(3):1893–1916.

[22] Bespalko, D., Pollard, A., and Uddin, M. (2012). Analysis of the pressure fluctuations from an lbm simulation of turbulent channel flow. *Comput. Fluids*, 54:143–146.

[23] Bhatnagar, P. L., Gross, E. P., and Krook, M. (1954). A model for collision processes in gases. i. small amplitude processes in charged and neutral one-component systems. *Phys. Rev.*, 94(3):511.

[24] Bird, R. B., Stewart, W. E., Lightfoot, E. N., and Klingenberg, D. J. (2015). *Introductory Transport Phenomena*, volume 1. Wiley New York.

[25] Bogey, C. and Bailly, C. (2002). Three-dimensional non-reflective boundary conditions for acoustic simulations: far field formulation and validation test cases. *Acta Acust united Ac.*, 88(4):463–471.

[26] Boghosian, B. M., Love, P. J., Coveney, P. V., Karlin, I. V., Succi, S., and Yepez, J. (2003). *Phys. Rev. E*, 68:025103(R).

[27] Brackbill, J. U. and Cohen, B. I. (2014). *Multiple time scales*, volume 3. Academic Press.

[28] Bridson, R., Houriham, J., and Nordenstam, M. (2007). Curl-noise for procedural fluid flow. *ACM Trans. Graph*, 26(3):46.

[29] Brull, S. and Schneider, J. (2009). On the ellipsoidal statistical model for polyatomic gases. *Contin. Mech. Thermodyn.*, 20(8):489–508.

[30] Buick, J., Greated, C., and Campbell, D. (1998). Lattice bgk simulation of sound waves. *Europhys. Lett.*, 43(3):235.

[31] Callen, H. B. (1998). Thermodynamics and an introduction to thermostatistics.

[32] Cercignani, C. (1988). The Boltzmann equation. In *The Boltzmann equation and its applications*, pages 40–103. Springer.

[33] Chaikin, P. M. and Lubensky, T. C. (2000). *Principles of condensed matter physics*, volume 1. Cambridge university press Cambridge.

[34] Chang, W. and Uhlenbeck, G. E. (1951). Transport phenomena in polyatomic gases. Technical report.

[35] Chapman, S. and Cowling, T. G. (1970). *The Mathematical Theory of Non-Uniform Gases: An Account of the Kinetic Theory of Viscosity, Thermal Conduction and Diffusion in Gases*. Cambridge university press.

[36] Chapman, S. and Cowling, T. G. (1990). *The mathematical theory of non-uniform gases: an account of the kinetic theory of viscosity, thermal conduction and diffusion in gases*. Cambridge university press.

[37] Chen, F., Xu, A., Zhang, G., Li, Y., and Succi, S. (2010). Multiple-relaxation-time lattice boltzmann approach to compressible flows with flexible specific-heat ratio and prandtl number. *EPL (Europhysics Letters)*, 90(5):54003.

[38] Chen, H., Chen, S., and Matthaeus, W. H. (1992). Recovery of the navier-stokes equations using a lattice-gas boltzmann method. *Phys. Rev. A*, 45(8):R5339.

[39] Chen, H. and Teixeira, C. (2000). H-theorem and origins of instability in thermal lattice boltzmann models. *Comp. Phys. Commun.*, 129(1):21–31.

[40] Chen, S. and Doolen, G. D. (1998). Lattice Boltzmann method for fluid flows. *Annu. Rev. Fluid Mech.*, 30(1):329–364.

[41] Chikatamarla, S., Ansumali, S., and Karlin, I. (2006a). Grad's approximation for missing data in lattice boltzmann simulations. *Europhys. Lett.*, 74(2):215.

[42] Chikatamarla, S., Frouzakis, C., Karlin, I., Tomboulides, A., and Boulouchos, K. (2010). Lattice boltzmann method for direct numerical simulation of turbulent flows. *J. Fluid Mech.*, 656:298–308.

[43] Chikatamarla, S. S., Ansumali, S., and Karlin, I. V. (2006b). Entropic lattice boltzmann models for hydrodynamics in three dimensions. *Phys. Rev. Lett.*, 97:010201.

[44] Chikatamarla, S. S. and Karlin, I. V. (2006). Entropy and galilean invariance of lattice boltzmann theories. *Phys. Rev. Lett.*, 97:190601.

[45] Chikatamarla, S. S. and Karlin, I. V. (2009). Lattices for the lattice boltzmann method. *Phys. Rev. E*, 79(4):046701.

[46] Crouse, B., Freed, D., Balasubramanian, G., Senthooran, S., Lew, P. T., and Mongeau, L. (2006). Fundamental aeroacoustics capabilities of the lattice-boltzmann method. In *12th AIAA/CEAS Aeroacoustics Conference (27th AIAA Aeroacoustics Conference)*, page 2571.

[47] Curtiss, C. F. and Hirschfelder, J. O. (1952). Integration of stiff equations. *Proceedings of the national academy of sciences*, 38(3):235–243.

[48] Dellar, P. J. (2001). Bulk and shear viscosities in lattice boltzmann equations. *Phys. Rev. E*, 64(3):031203.

[49] Dorschner, B., Frapolli, N., Chikatamarla, S. S., and Karlin, I. V. (2016). Grid refinement for entropic lattice boltzmann models. *Phys. Rev. E*, 94(5):053311.

[50] Frapolli, N., Chikatamarla, S., and Karlin, I. (2014). Multispeed entropic lattice Boltzmann model for thermal flows. *Phys. Rev. E*, 90(4):043306.

[51] Frisch, U. (1995). *Turbulence: the legacy of AN Kolmogorov*. Cambridge university press.

[52] Gear, C. (1969). The automatic integration of stiff ordinary differential equations. *Proc. 88*, pages 187–193.

[53] Gear, C. W. and Kevrekidis, I. G. (2003). Projective methods for stiff differential equations: problems with gaps in their eigenvalue spectrum. *SIAM Journal on Scientific Computing*, 24(4):1091–1106.

[54] Gendre, F., Ricot, D., Fritz, G., and Sagaut, P. (2017). Grid refinement for aeroacoustics in the lattice boltzmann method: A directional splitting approach. *Phys. Rev. E*, 96(2):023311.

[55] Glassman, I., Yetter, R. A., and Glumac, N. G. (2014). *Combustion*. Academic press.

[56] Gorban, A. N. and Karlin, I. V. (1994). General approach to constructing models of the Boltzmann equation. *Physica A*, 206(3-4):401–420.

[57] Grad, H. (1958). Principles of the kinetic theory of gases. In *Thermodynamik der Gase/Thermodynamics of Gases*, pages 205–294. Springer.

[58] Green, D. W. and Southard, M. Z. (2019). *Perry's chemical engineers' handbook*. McGraw-Hill Education.

[59] Hanumantharayappa, M. N., Thantanapally, C., Namburi, M., Kumaran, V., and Ansumali, S. (2021). Les/dns of flow past t106 lpt cascade using a higher-order lb model. *AIAA Propulsion and Energy 2021 Forum*, page 3485.

[60] Hardin, J., Ristorcelli, J., and Tam, C. (1994). *ICASE/LaRC workshop on benchmark problems in computational aeroacoustics*.

[61] Hittinger, J. A. (2001). *Foundations for the generalization of the Godunov method to hyperbolic systems with stiff relaxation source terms.* PhD thesis, The University of Michigan.

[62] Holway Jr, L. H. (1965). Kinetic theory of shock structure using an ellipsoidal distribution function. *Rarefied Gas Dyn.*, 1:193.

[63] Holway Jr, L. H. (1966). New statistical models for kinetic theory: methods of construction. *Phys. Fluids*, 9(9):1658–1673.

[64] Horn, R. A. and Johnson, C. R. (2012). *Matrix analysis*. Cambridge university press.

[65] Huang, K. (2009). *Introduction to statistical physics*. Chapman and Hall/CRC.

[66] Huang, R., Lan, L., and Li, Q. (2020). Lattice boltzmann simulations of thermal flows beyond the boussinesq and ideal-gas approximations. *Physical Review E*, 102(4):043304.

[67] Huang, Y. and Bau, H. H. (1997). Thermoacoustic waves in a confined medium. *Int. J. Heat Mass Transf.*, 40(2):407 – 419.

[68] Karlin, I. V., Ferrante, A., and Öttinger, H. C. (1999). Perfect entropy functions of the lattice boltzmann method. *Europhys. Lett.*, 47(2):182.

[69] Karlin, I. V., Gorban, A. N., Succi, S., and Boffi, V. (1998). Maximum entropy principle for lattice kinetic equations. *Phys. Rev. Lett.*, 81(1):6.

[70] Kataoka, T. and Tsutahara, M. (2004). Lattice boltzmann model for the compressible navier-stokes equations with flexible specific-heat ratio. *Physical review E*, 69(3):035701.

[71] Kida, S. (1985). Three-dimensional periodic flows with high-symmetry. *Journal of the Physical Society of Japan*, 54(6):2132–2136.

[72] Kim, H. and Durbin, P. (1988). Observations of the frequencies in a sphere wake and of drag increase by acoustic excitation. *Phys. Fluids*, 31(11):3260–3265.

[73] Kim, J., Moin, P., and Moser, R. (1987). Turbulence statistics in fully developed channel flow at low reynolds number. *J. Fluid Mech.*, 177:133–166.

[74] Kogan, M. N. (1969). *Rarefied Gas Dynamics. Translated from Russian*. Plenum Press.

[75] Kolluru, P. K., Atif, M., and Ansumali, S. (2020). Extended BGK model for diatomic gases. *J. Comput. Sci.*, 45:101179.

[76] Krithivasan, S., Wahal, S., and Ansumali, S. (2014). Diffused bounce-back condition and refill algorithm for the lattice boltzmann method. *Phys. Rev. E*, 89(3):033313.

[77] Kuščer, I. (1989). A model for rotational energy exchange in polyatomic gases. *Physica A*, 158(3):784–800.

[78] Ladd, A. and Verberg, R. (2001). Lattice-boltzmann simulations of particle-fluid suspensions. *J. Stat. Phys.*, 104(5-6):1191–1251.

[79] Ladd, A. J. (1994). Numerical simulations of particulate suspensions via a discretized boltzmann equation. part 1. theoretical foundation. *J. Fluid Mech.*, 271:285–309.

[80] Ladd, A. J. C. (1993). Short-time motion of colloidal particles: Numerical simulation via a fluctuating lattice-boltzmann equation. *Phys. Rev. Lett.*, 70:1339–1342.

[81] Landau, L. and Lifshitz, E. (1987). Fluid mechanics. translated from the russian by jb sykes and wh reid. *Course of Theoretical Physics*, 6.

[82] Landau, L. D. and Lifshitz, E. (1959). *Course of Theoretical Physics Vol. 6 Fluid Mechanics*. Pergamon Press.

[83] Larina, I. and Rykov, V. (2010). Kinetic model of the Boltzmann equation for a diatomic gas with rotational degrees of freedom. *Computational Mathematics and Mathematical Physics*, 50(12):2118–2130.

[84] Larkin, B. (1967). Heat flow to a confined fluid in zero gravity. In *Thermophysics of Spacecraft and Planetary Bodies*, pages 819–832. Elsevier.

[85] Leal, L. G. (2007). *Advanced transport phenomena: fluid mechanics and convective transport processes*, volume 7. Cambridge University Press.

[86] Lebowitz, J., Frisch, H., and Helfand, E. (1960). Nonequilibrium distribution functions in a fluid. *Phys. Fluids*, 3(3):325–338.

[87] Levermore, C. D. (1996). Moment closure hierarchies for kinetic theories. *J. Stat. Phys.*, 83(5-6):1021–1065.

[88] Li, Y. and Shan, X. (2011). Lattice boltzmann method for adiabatic acoustics. *Philosophical Transactions of the Royal Society A: Mathematical, Physical and Engineering Sciences*, 369(1944):2371–2380.

[89] Liboff, R. L. (2003). *Kinetic theory: classical, quantum, and relativistic descriptions*. Springer Science & Business Media.

[90] Liepmann, H. W., Narasimha, R., and Chahine, M. T. (1962). Structure of a plane shock layer. *Phys. Fluids*, 5(11):1313–1324.

[91] Lubich, C. (1993). Integration of stiff mechanical systems by runge-kutta methods. *Zeitschrift für angewandte Mathematik und Physik ZAMP*, 44(6):1022–1053.

[92] MacCormack, R. (2003). The effect of viscosity in hypervelocity impact cratering. *Journal of spacecraft and rockets*, 40(5):757–763.

[93] Marié, S., Ricot, D., and Sagaut, P. (2009). Comparison between lattice boltzmann method and navier-stokes high order schemes for computational aeroacoustics. *J. Comput. Phys.*, 228(4):1056–1070.

[94] Mazloomi M, A., Chikatamarla, S. S., and Karlin, I. V. (2015). Entropic lattice boltzmann method for multiphase flows. *Phys. Rev. Lett.*, 114(17):174502.

[95] McQuarrie, D. (2000). *Statistical Mechanics*. University Science Books.

[96] Morse, T. (1964). Kinetic model for gases with internal degrees of freedom. *The physics of fluids*, 7(2):159–169.

[97] Moser, R. D., Kim, J., and Mansour, N. N. (1999). Direct numerical simulation of turbulent channel flow up to re τ= 590. *Phys. Fluids*, 11(4):943–945.

[98] Mott-Smith, H. M. (1951). The solution of the Boltzmann equation for a shock wave. *Phys. Rev.*, 82(6):885.

[99] Müller, I. and Ruggeri, T. (2013). *Rational extended thermodynamics*. Springer Science & Business Media.

[100] Murthy, J. S. N., Kolluru, P. K., Kumaran, V., and Ansumali, S. (2018). Lattice Boltzmann method for wave propagation in elastic solids. *Commun. Comput. Phys.*, 23(4):1223–1240.

[101] Namburi, M., Krithivasan, S., and Ansumali, S. (2016). Crystallographic lattice Boltzmann method. *Sci. Rep.*, 6:27172.

[102] Nie, X., Shan, X., and Chen, H. (2008). Thermal lattice Boltzmann model for gases with internal degrees of freedom. *Phys. Rev. E*, 77(3):035701.

[103] Oh, C., Oran, E., and Sinkovits, R. (1997). Computations of high-speed, high Knudsen number microchannel flows. *J. Thermophys. Heat Trans.*, 11(4):497–505.

[104] Parang, M. and Salah-Eddine, A. (1984). Thermoacoustic convection heat-transfer phenomenon. *AIAA J.*, 22(7):1020–1022.

[105] Pope, S. B. (2001). Turbulent flows.

[106] Pozrikidis, C. and Jankowski, D. (1997). *Introduction to theoretical and computational fluid dynamics*, volume 675. Oxford university press New York.

[107] Pullin, D. (1978). Kinetic models for polyatomic molecules with phenomenological energy exchange. *Phys. Fluids*, 21(2):209–216.

[108] Qian, Y., d'Humières, D., and Lallemand, P. (1992). Lattice bgk models for navier-stokes equation. *Europhys. Lett.*, 17(6):479.

[109] Qian, Y.-H. and Zhou, Y. (1998). Complete galilean-invariant lattice bgk models for the navier-stokes equation. *Europhys. Lett.*, 42(4):359.

[110] Reichl, L. E. (1999). A modern course in statistical physics.

[111] Resibois, P. (1978). H-theorem for the (modified) nonlinear enskog equation. *Journal of Statistical Physics*, 19(6):593–609.

[112] Rodríguez, I., Lehmkuhl, O., Borrell, R., and Oliva, A. (2013). Flow dynamics in the turbulent wake of a sphere at sub-critical reynolds numbers. *Comput. Fluids*, 80:233–243.

[113] Ruggeri, T. and Sugiyama, M. (2015). *Rational extended thermodynamics beyond the monatomic gas*. Springer.

[114] Rykov, V. (1975). A model kinetic equation for a gas with rotational degrees of freedom. *Fluid Dynamics*, 10(6):959–966.

[115] Schäfer, E. (1975). A new approach to explain the "high irradiance responses" of photomorphogenesis on the basis of phytochrome. *Journal of Mathematical Biology*, 2(1):41–56.

[116] Shakhov, E. (1968). Generalization of the krook kinetic relaxation equation. *Fluid dynamics*, 3(5):95–96.

[117] Shampine, L. F. (2018). *Numerical solution of ordinary differential equations*. Routledge.

[118] Shampine, L. F. and Gear, C. W. (1979). A user's view of solving stiff ordinary differential equations. *SIAM review*, 21(1):1–17.

[119] Shan, X. and He, X. (1998). Discretization of the velocity space in the solution of the Boltzmann equation. *Phys. Rev. Lett.*, 80(1):65–68.

[120] Shan, X., Yuan, X.-F., and Chen, H. (2006). Kinetic theory representation of hydrodynamics: a way beyond the navier–stokes equation. *J. Fluid Mech.*, 550:413–441.

[121] Singh, S. and Ansumali, S. (2015). Fokker–Planck model of hydrodynamics. *Phys. Rev. E*, 91(3):033303.

[122] Singh, S., Krithivasan, S., Karlin, I. V., Succi, S., and Ansumali, S. (2013). Energy conserving lattice boltzmann models for incompressible flow simulations. *Commun. Comput. Phys.*, 13(3):603–613.

[123] Singh, S., Thantanapally, C., and Ansumali, S. (2016). Gaseous microflow modeling using the fokker-planck equation. *Physical Review E*, 94(6):063307.

[124] Spradley, L. W. and Churchill, S. W. (1975). Pressure- and buoyancy-driven thermal convection in a rectangular enclosure. *J. Fluid Mech.*, 70(4):705–720.

[125] Struchtrup, H. (2004). Stable transport equations for rarefied gases at high orders in the Knudsen number. *Phys. Fluids*, 16(11):3921–3934.

[126] Struchtrup, H. (2005). *Macroscopic transport equations for rarefied gas flows*. Springer.

[127] Succi, S. (2001). *The lattice Boltzmann equation: for fluid dynamics and beyond*. Oxford university press.

[128] Succi, S., Karlin, I. V., and Chen, H. (2002). Colloquium: Role of the H theorem in lattice Boltzmann hydrodynamic simulations. *Reviews of Modern Physics*, 74(4):1203.

[129] Tam, C. and Hu, F. (2004). *An optimized multi-dimensional interpolation scheme for computational aeroacoustics applications using overset grid*.

[130] Tam, C. K. and Hardin, J. (1997). *Second computational aeroacoustics (CAA) workshop on benchmark problems*.

[131] Tam, C. K. and Webb, J. C. (1993). Dispersion-relation-preserving finite difference schemes for computational acoustics. *J. Comput. Phys.*, 107(2):262–281.

[132] Tsutahara, M., Kataoka, T., Shikata, K., and Takada, N. (2008). New model and scheme for compressible fluids of the finite difference lattice Boltzmann method and direct simulations of aerodynamic sound. *Comput. Fluids*, 37(1):79–89.

[133] Viggen, E. M. (2013). Acoustic multipole sources for the lattice boltzmann method. *Phys. Rev. E*, 87:023306.

[134] Viggen, E. M. (2014). Acoustic equations of state for simple lattice boltzmann velocity sets. *Phys. Rev. E*, 90:013310.

[135] von Backstrom, T. W. (2008). The effect of specific heat ratio on the performance of compressible flow turbo-machines. In *ASME Turbo Expo 2008*, pages 2111–2117. ASME.

[136] Wagner, A. J. (1998). An h-theorem for the lattice boltzmann approach to hydrodynamics. *Europhys. Lett.*, 44(2):144.

[137] Wang, Z., Yan, H., Li, Q., and Xu, K. (2017). Unified gas-kinetic scheme for diatomic molecular flow with translational, rotational, and vibrational modes. *J. Comput. Phys.*, 350:237–259.

[138] Wang-Chang, C. and Uhlenbeck, G. (1951). Transport phenomena in polyatomic gases. *Research Rep. CM-681. University of Michigan Engineering*.

[139] Wanner, G. and Hairer, E. (1996). *Solving ordinary differential equations II*, volume 375. Springer Berlin Heidelberg New York.

[140] Watari, M. (2007). Finite difference lattice Boltzmann method with arbitrary specific heat ratio applicable to supersonic flow simulations. *Physica A*, 382(2):502–522.

[141] Westbrook, C. K. and Dryer, F. L. (1984). Chemical kinetic modeling of hydrocarbon combustion. *Progress in energy and combustion science*, 10(1):1–57.

[142] Wu, L., White, C., Scanlon, T. J., Reese, J. M., and Zhang, Y. (2015). A kinetic model of the Boltzmann equation for non-vibrating polyatomic gases. *J. Fluid Mech.*, 763:24–50.

[143] Yudistiawan, W. P., Ansumali, S., and Karlin, I. V. (2008). Hydrodynamics beyond navier-stokes: The slip flow model. *Phys. Rev. E*, 78(1):016705.

[144] Yudistiawan, W. P., Kwak, S. K., Patil, D. V., and Ansumali, S. (2010). Higher-order galilean-invariant lattice boltzmann model for microflows: Single-component gas. *Phys. Rev. E*, 82:046701.

[145] Yun, G., Kim, D., and Choi, H. (2006). Vortical structures behind a sphere at subcritical reynolds numbers. *Phys. Fluids*, 18(1):015102.